Università degli Studi di Trieste

XXXV Ciclo del Dottorato di ricerca in Fisica

PHD THESIS

2D Materials on metal surfaces: a numerical approach

Settore scientifico-disciplinare: fisica della materia computazionale

PhD student:
Simone Del Puppo

PhD Supervisor:
Maria Peressi

PhD Coordinator:
Francesco Longo

Academic year 2021-2022

Contents

List of Acronyms

ARPES	Angular-Resolved-Photoemission Spectroscopy
BP	Blue-Phosphorus
BZ	Brillouin Zone
CLS	Core Level Shift
CO	Carbon Monoxide
CVD	Chemical Vapour Deposition
DFT	Density Functional Theory
DoS	Density of States
EG(RG)	Epitaxial (Rotated) Graphene
EGC(RGC)	Epitaxial (Rotated) Graphene with nickel carbide
FFT	Fast-Fourier-Transform
G	Graphene Layer
HPC	High-Performance-Computing
ICD	Induced Charge Density
ILDoS	Integrated Local Density of States
KS	Kohn - Sham
LAMMPS	Large-scale Atomic Molecular Massively Parallel Simulator
LDoS	Local Density of States
LEED	Low energy electron diffraction
MD	Molecular Dynamics
ML	Monolayer
NEB	Nudged elastic band
Ni_2C	Nickel carbide
NN	Neural-Network
PBC	Periodic Boundary Conditions

PDoS	Projected Density of States
PES	Potential Energy Surface
PP	PseudoPotantials
QE	Quantum Espresso
SCF	Self-consistent cycle
STM	Scanning Tunneling Microscopy
XPS	X-ray Photoelectron Spectroscopy

Abstract

The field of two-dimensional (2D) materials is rapidly rising after the discovery of graphene in 2004. 2D allotropes of various elements or compounds offer great flexibility in terms of structural and electronic properties, and are widely studied for several technological applications, including electronic devices, sensors, light harvesting. 2D materials can be synthesized by Chemical Vapor Deposition (CVD) on different substrates, which play an important role, affecting composition, quality, properties of the 2D layers. In general, an efficient integration of 2D layers with transition metal substrates seems a promising yet broad and challenging field.

Although the extensive work on 2D materials, a comprehensive understanding of the layer-substrate interaction and how this affects the structure and the electronic properties is still lacking, even for the most famous 2D material, graphene. With the aim of shedding light on this still open issue, in this work we extensively investigated through numerical simulations some selected systems based on two different 2D materials, Graphene (G) on Nickel (Ni) substrates (most of the work) and Blue-Phosphorus (BP) on Gold (Au) substrate, using different and, to some extent, complementary numerical approaches. Most of the work consisted in quantum mechanical ab-initio simulations based on Density Functional Theory (DFT), paying attention to some specific technical details to ensure the accuracy and the reliability of the results. Part of the work concerned the construction via neural network techniques and the validation of new interatomic potentials to extend the investigation of G/Ni sys-

tems to more realistic configurations or to dynamical processes not directly affordable by ab-initio calculations. Throughout the work, a direct comparison with published or new experimental results is discussed.

Graphene can be easily grown by CVD on nickel substrates but its electronic and structural properties depend on the matching/mismatching and on the alignment/misalignment between its hexagonal lattice and the underlying surface lattice. The thesis starts with the investigation of epitaxial G on Ni(111), which is already very well known. Starting from a set of DFT calculations that we also used as a benchmark to refine many technical details of our simulations on other new configurations, we used a Neural Network to generate an interatomic potential able to accurately predict energy and forces in this system. The new potential allows to perform molecular dynamics simulations with thousands of atoms with accuracy close to that of DFT, paving the way for large-scale simulations of such system. We report a successful application on large G domains showing coexistence of different registries with the substrate.
After that, structural reconstruction that Ni(111) surface undergoes at high temperatures during CVD process has been investigated. We showed how the presence of rotated domains of graphene with respect to Ni(111) lattice affects the formation of a nickel carbide phase, Ni_2C, underneath.
Furthermore, we studied the intercalation of Carbon Monoxide under epitaxial G grown on Ni(111) providing a systematic investigation of the intercalated CO pattern, highlighting the modifications induced on the graphene electronic structure. The most important signature of CO intercalation is a shift of Dirac cones linearly dependent on the CO coverage, opening the way to application as gas sensor to easily detect and quantify its presence.
In this work, G on Ni(100) has also been studied. Such an interface, due to lattice mismatch, presents a stripe moiré pattern in which

strongly (chemisorbed) and weakly (physisorbed) interacting G regions with Ni surface alternate, inducing anisotropic modulated electronic structure and reactivity properties. Here we provided a full investigation of different kind of defects of G layer and we investigated how they can increase the reactivity of graphene for metal adatoms or molecules adsorption.

The last part of the thesis has been devoted to Blue-Phosphorus, a new 2D material made by only P atoms arranged similarly to graphene but with a larger lattice parameter and a small buckling of the two constituent sublattices. To describe BP grown on Au(111), we identified as the best candidate a structural model formed by P_9 pyramidal shaped domains connected by Au adatoms in a 5x5 supercell. The nice correspondence with many different new experimental results, including STM images and ARPES spectra, allows to discriminate among different possible models, indicating once again the necessity of a synergetic effort between simulations and experiments to shed light on the structure and properties of real systems.

Introduction

In the last few years the field of 2D materials raised particular attention, extending from graphene [1] [2] to the discovery of many others such as Black phosphorene[3] [4], metal dichalcogenides [5] [6] [7] [8], borophene [9] [10], silicene [11] [12] [13] and so on, due to their simple compositions and their promising potential applications in different technological sectors [14] [15] [16] [17] [18] [19]. Conversely to 3D bulk materials, these materials offer the great advantage of having an atomic thickness making them ideal for minimizing the size of devices. Furthermore, they showed a wide range of tunable electronic properties. For example, graphene has a very high electron mobility which makes it suitable for optoelectronic devices and for light harvesting applications [20], while metal dichalcogenides and black phosphorene showed an intriguing semiconducting behavior making them suitable for other industrial applications [21] [22] [23] [24] [25]. Many 2D materials, such as graphene and black phosphorene, can be exfoliated from their 3D counterpart, but this procedure is not efficient for a large scale fabrication [19]. For this reason, other bottom-up methods, such as Chemical-Vapour-Deposition, have been developed in the last decades leading to high quality and large scale fabrications [26] . On the other hand, other 2D materials, such as borophene and silicene, could be only synthesized with the support of a substrate using bottom-up method. The choice of the substrate is fundamental for the electronic properties of the 2D material.
The goal of this work is to explore the field of 2D materials integrated on metal substrates using a numerical approach. In particular, in the

first part we will report on graphene on different nickel surfaces, i.e. (111) and (100), while in the second part another very recent 2D material, i.e. Blue-Phosphorus, is investigated.

The larger part of the thesis is based on quantum mechanical simulations within the framework of the Density Functional Theory (DFT), but we also investigate the generation of new potentials using Neural Network techniques. Computational resources have been obtained from CINECA through ISCRA projects and the agreement with University of Trieste.

The present thesis has been organized as follows:

- **Chapter 1**: a brief overview on the theory behind ab-initio approach and about the software used for simulations is given. Notions of Neural Networks and how they can be used in a procedure to generate interatomic interaction are also reported.
- **Chapter 2**: different results for graphene on Ni(111) are reported. The first part is devoted to the generation and test of new interatomic potentials to model several G/Ni(111) systems. In the second part, nickel carbide formation under rotated graphene domains is investigated through Density-Functional-Theory simulations. In the last part of the chapter we investigate the intercalation of carbon monoxide under G layer, showing how it affects the G's electronic properties.
- **Chapter 3**: a systematic investigation of defects of G on Ni(100) is reported, showing how they can increase the reactivity of graphene layer for metal adatoms and carbon monoxide adsorption.
- **Chapter 4**: electronic and structural properties of Blue-Phosphorus on Au(111) has been investigated through DFT simulations and the results are compared with experimental evidences.

- **Chapter 5**: the main results are summarized and some future perspectives are given.

Chapter 1

Theory and numerical approach

The first part of this chapter summarizes some basic concepts of the theory behind ab-initio calculations and introduces useful concept and technicalities implemented in Quantum ESPRESSO(QE) [27], an open source package to perform such simulations.
Finally, an overview about Neural Networks(NN) and how they can be used to generate interatomic potentials and carry out Molecular Dynamic simulations is given.

1.1 Electrons and nuclei

Let's consider a physical system, such as molecules, surfaces or solids, composed by N_i nuclei with charge $-Z_i e$ and mass M_i and N electrons with charge e and mass m_e mutually interacting one each other. The total hamiltonian of the system can be written as:

$$H = T_N + V_{NN} + T_e + V_{ee} + V_{eN} \tag{1.1}$$

where T_N and T_e are the kinetic terms of nuclei and electrons respectively, V_{NN} the nucleus-nucleus interaction, V_{ee} the electron-electron interaction and V_{eN} the electron-nucleus interaction. They can be written as:

$$T_N = \sum_{i=1}^{N_i} \frac{\mathbf{P}_i^2}{2M_i} \qquad V_{NN} = \frac{e^2}{2} \sum_{i \neq j} \frac{Z_i Z_j}{\mid \mathbf{R}_i - \mathbf{R}_j \mid} \tag{1.2}$$

$$T_e = \sum_{i=1}^{N_i} \frac{\mathbf{p}_i^2}{2m_e} \qquad V_{ee} = \frac{e^2}{2} \sum_{i \neq j} \frac{1}{\mid \mathbf{r}_i - \mathbf{r}_j \mid} \tag{1.3}$$

$$V_{eN} = -\frac{e^2}{2} \sum_{j} \frac{Z_j}{\mid \mathbf{r}_i - \mathbf{R}_j \mid} \tag{1.4}$$

where we used $\mathbf{r}$ ($\mathbf{R}$) to denote the positions of electrons (nuclei) and $\mathbf{p}$ ($\mathbf{P}$) their momenta.

The Schrödinger equation for such an hamiltonian cannot be solved exactly and an approximation is necessary. Since the mass of nuclei is much greater than the mass of electrons and since the typical electrons velocities are much greater than the nuclei velocities, it is possible to separate the nuclei and electrons motions (*Born-Oppenheimer approximation*). In this way, when considering the electronic motion, T_N can be neglected and nuclei positions ($\mathbf{R}$) are treated as parameters. The electronic eigenvalue problem thus becomes:

$$H_e \psi_e(\{\mathbf{r}\}; \{\mathbf{R}\}) = E(\{\mathbf{R}\}) \psi_e(\{\mathbf{r}\}; \{\mathbf{R}\}) \tag{1.5}$$

with

$$H_e = T_e + V_{ee} + V_{eN} + V_{NN} \tag{1.6}$$

This equation is still very difficult to solve when there are a lot of electrons in the system (actually, even for two electrons only) and a more efficient way is needed.
$E(\{\mathbf{R}\})$ describes a *Potential Energy Surface* for the nuclei and is used to evaluate the forces acting on the them:

$$\mathbf{F}_i \equiv -\nabla_{\mathbf{R}_i} E(\{\mathbf{R}\}) \tag{1.7}$$

This expression can be further simplified for computing using the Hellmann-Feynmann theorem [28]:

$$\mathbf{F}_i = \langle \psi(\{\mathbf{r}\}; \{\mathbf{R}\}) | \frac{\partial \hat{H}_e}{\partial \mathbf{R}_i} | \psi(\{\mathbf{r}\}; \{\mathbf{R}\}) \rangle \tag{1.8}$$

1.2 Ab-initio approach

An efficient solution mthod for the electronic problem described by equation 1.5 is based on Density Functional Theory (DFT). The theory lies on two theorems, formulated by Hoenberg and Kohn in 1964 [29]:

- **Theorem 1**: For any system of interacting particles in an external potential v_{ext}, the potential v_{ext} is determined uniquely, a part from a constant, by the ground state electronic density $n_0(\mathbf{r})$.
- **Theorem 2**: For any external potential v_{ext}, it is possible to define the energy of the system as a functional of the density $n(\mathbf{r})$: $E = E[n]$. Moreover, the ground state energy of the system is the minimum value of this functional and the density that minimizes it, keeping the number of electron N constant, is the ground state density $n_0(\mathbf{r})$.

In cases of interest for this work, v_{ext} is the nuclear potential experienced by the electrons, namely the V_{eN} term, thus the energy functional can be written as:

$$E[n] = T_e[n] + V_{ee}[n] + \int v_{ext}(\mathbf{r})n(\mathbf{r})d\mathbf{r} + E_{NN} \tag{1.9}$$

where E_{NN} is the energy from nucleus-nucleus interaction and it is a constant term due to Born-Oppenheimer approximation. In principle, from the second theorem of Hohenberg-Kohn, it is possible to find all the ground state properties by the minimization of the functional $E[n]$.
The main difficulty is that $T_e[n]$ and $V_{ee}[n]$ are in general not known since the system is interacting. Kohn and Sham found a method to overcome this issue in 1965 [30]; they demonstrated that it is possible to reduce the electronic interacting many-body system to an auxiliary non-interacting one with particles in an effective potential and

with the same ground state electronic density (figure 1.1). This new problem is computationally easier to solve and it allows to have an excellent description of structural and electronic properties of a wide class of materials.

For this purpose the energy functional $E[n]$ in equation 1.9 can be rewritten as:

$$E[n] = T_s[n] + E_{Hartree}[n] + \int v_{ext}(\mathbf{r}) n(\mathbf{r}) d\mathbf{r} + E_{NN} + E_{xc}[n] \quad (1.10)$$

where we have introduced the following terms:

- $T_s[n]$ is the kinetic energy functional of the fictitious system;
- $E_{Hartree}[n]$ is the classic Coulomb interaction energy:

$$E_{Hartree}[n] = \frac{e^2}{2} \int \frac{n(\mathbf{r}) n(\mathbf{r}')}{|\mathbf{r} - \mathbf{r}'|} d\mathbf{r}' d\mathbf{r}$$

- $E_{xc}[n]$ is the *exchange-correlation* energy functional; it contains all the many-body effects of exchange and correlation and it is defined as:

$$E_{xc}[n] = T_e[n] - T_s[n] + V_{ee}[n] - E_{Hartree}[n]$$

It is now possible to minimize the functional $E[n]$ with respect to the electronic density $n(\mathbf{r})$, keeping the number of electrons constant. This leads to single-particle Schrödinger-like equations for the electrons of the fictitious system, called *Kohn-Sham equations* (KS):

$$\left(-\frac{\hbar^2 \nabla^2}{2m_e} + V_{KS}(\mathbf{r}) \right) \psi_i(\mathbf{r}) = \epsilon_i \psi_i(\mathbf{r}) \quad (1.11)$$

where $V_{KS}(\mathbf{r})$ is the Kohn-Sham potential given by:

$$V_{KS}(\mathbf{r}) = v_{ext}(\mathbf{r}) + e^2 \int \frac{n(\mathbf{r}')}{|\mathbf{r} - \mathbf{r}'|} d\mathbf{r}' + \frac{\delta E_{xc}[n]}{\delta n(\mathbf{r})} \quad (1.12)$$

and $\psi_i(\mathbf{r})$ are the single-particle wavefunctions of the fictitious system, namely the *Kohn-Sham eigenstates*.

No approximations have been done so far thus in principle, if exact exchange-correlation functional $E_{xc}[n]$ would be known, KS equations would give the exact ground state of the interacting system. Most of the times this is not possible and an approximation is needed. Finally, note that the equations 1.11, though mathematically very similar to a Schrödinger equation, are conceptually very different: the Khon-Sham potential $V_{KS}(\mathbf{r})$ depends on the electronic density $n(\mathbf{r})$ but this is related to Kohn-Sham eigenstates through relation $n(\mathbf{r}) = \sum_i |\psi_i(\mathbf{r})|^2$ so the equations must be solved self-consistently, as explained in next subsection.

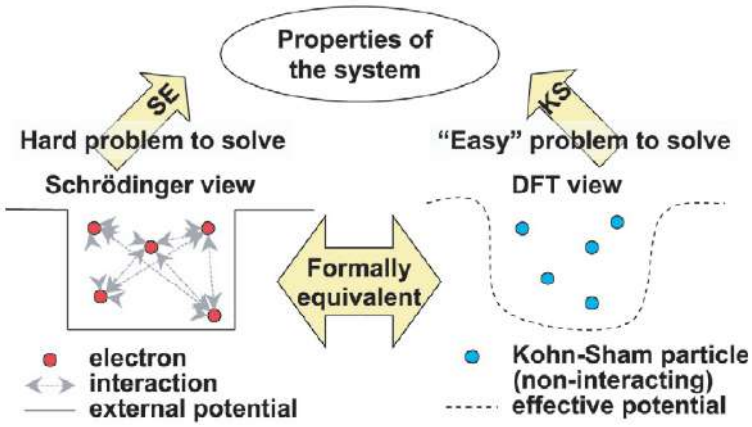

Figure 1.1: Qualitative scheme of Density Functional Theory. The real interacting many-body system is formally equivalent to non-interacting many-body system with an effective potential which is easier to solve computationally. Image taken from the website `https://assignmentpoint.com/dft-density-functional-theory/` .

Self-consistent cycle

Equations 1.11 can be computationally solved by means of the self-consistent loop reported in figure 1.2.

First of all, an initial guess of the electronic density $n(\mathbf{r})$ is made and the KS potential is calculated. Then the KS equations are solved and the electronic density is recalculated from the new KS orbitals. At this point the new electronic density is compared with the one given in input: if their difference is larger than a given threshold the loop restarts with a new guess of the electronic density otherwise the

KS equations are solved and the calculation ends. The new guess of electronic density is not completely random but is a proper weighted average between the old one and a new one randomly generated. Many algorithms to make a proper choice of the electronic density have already been studied in order to speed up the convergence [31] [32].
Once the convergence is achieved, many output quantities such as total energy, forces and electronic properties of the system can be obtained. A brief description of them will be given in section 1.3.

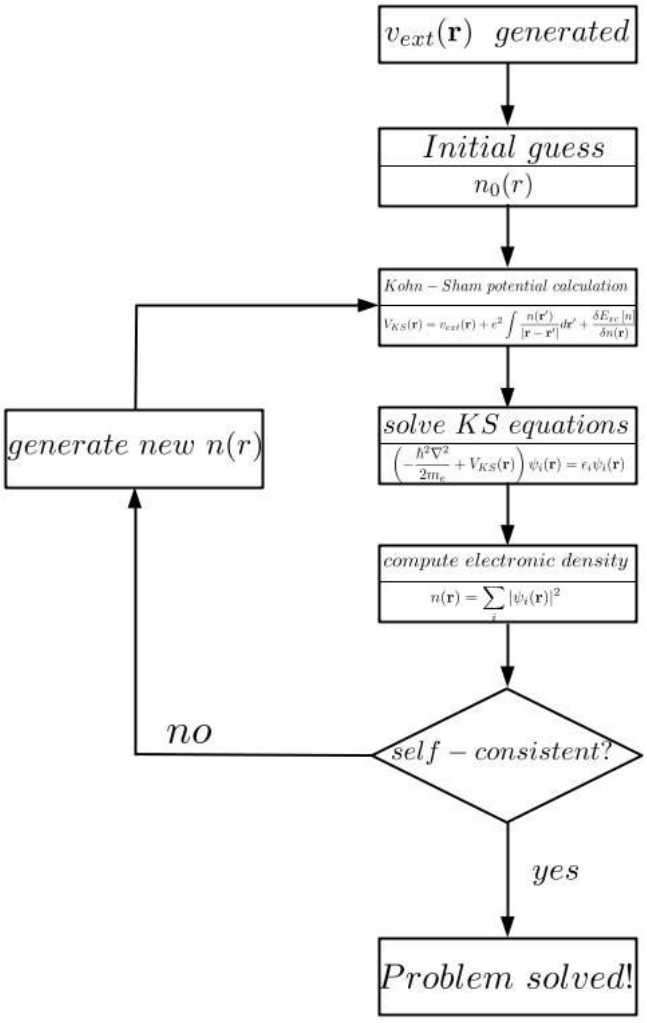

Figure 1.2: Schematic algorithm of the self-consistent cycle for the solution of KS equations 1.11.

Exchange-Correlation approximations

The exchange-correlation term, $E_{xc}[n]$, in equation 1.11 is not known in general and a reasonable approximation is needed. The most simple is called *Local Density Approximation*(LDA) in which the exchange-correlation energy is assumed to be equal to that of an homogeneous electron gas ϵ_{xc}^{hom}:

$$E_{xc}^{LSDA}[n(\mathbf{r})] = \int d\mathbf{r}\ n(\mathbf{r})\epsilon_{xc}^{hom}(n(\mathbf{r})) \tag{1.13}$$

However, LDA fails in some cases. An improvement can be made by considering also the gradient of the electron density. This is called *Generalized Gradient Approximation* and the exchange-correlation functional becomes:

$$E_{xc}^{GGA}[n(\mathbf{r})] = \int d\mathbf{r}\ n(\mathbf{r})\epsilon_{xc}^{hom}(n(\mathbf{r}))F(n(\mathbf{r}), \nabla n(\mathbf{r})) \tag{1.14}$$

In both cases we can take into account of the spin of the particles and consider two electron densities, one for spin up and one for spin down and their gradients. In the present work all the simulations were performed in the Generalized Gradient Approximation and the parametrization of F is given by Perdew-Burke-Ernzerhof (PBE) functional[33].

1.3 QUANTUM ESPRESSO **package**

In order to solve the Kohn-Sham equations efficiently, the schema described in previous section needs to be further reformulated. Among many ways to do this, QUANTUM ESPRESSO(QE) [27] exploits a plane-wave basis set expansion to reduce the equations 1.11 into a matrix diagonalization problem. The use of pseudopotentials to describe the valence electrons is a further simplification of the problem, instead of a all-electrons approach. In this section an overview of the technicalities implemented in QE to solve KS equations are provided.

1.3.1 Computational details

Plane-wave expansion

Let's consider a periodic system, such as a crystal, with translational periodicity $\mathbf{R}$. From Bloch theorem [34] we know that the wavefunctions can be written as:

$$\psi_{n,\mathbf{k}}(\mathbf{r}) = e^{i\mathbf{kr}} u_{n,\mathbf{k}}(\mathbf{r}) \tag{1.15}$$

where $u_{n,\mathbf{k}}(\mathbf{r})$ is such that $u_{n,\mathbf{k}}(\mathbf{r}) = u_{n,\mathbf{k}}(\mathbf{r}+\mathbf{R})$ and $e^{i\mathbf{kr}}$ is a generic plane wave. Since plane wave basis set is an infinite complete basis set, it is possible to expand $u_{n,\mathbf{k}}(\mathbf{r})$ as:

$$u_{n,\mathbf{k}}(\mathbf{r}) = \frac{1}{\Omega} \sum_{\mathbf{G}} c_{\mathbf{k},\mathbf{G}} e^{i\mathbf{Gr}} \tag{1.16}$$

where Ω is the volume of the unit cell, $\mathbf{G}$ is a reciprocal lattice vector and the sum is only on the $\mathbf{G}$ vectors due to the lattice periodicity. Equation 1.15 thus becomes:

$$\psi_{n,\mathbf{k}}(\mathbf{r}) = \frac{1}{\Omega} \sum_{\mathbf{G}} c_{n,\mathbf{k},\mathbf{G}} e^{i(\mathbf{G}+\mathbf{k})\mathbf{r}} \equiv \sum_{\mathbf{G}} c_{n,\mathbf{k}+\mathbf{G}} \Phi_{\mathbf{k}+\mathbf{G}} \tag{1.17}$$

where $\Phi_{\mathbf{k}+\mathbf{G}}$ is still a plane wave with momentum $\mathbf{k}+\mathbf{G}$. Inserting 1.17 into KS equations 1.11 allows to turn the problem into a matrix diagonalization which is computationally much simpler:

$$\sum_{\mathbf{G}} \left(\langle \Phi_{\mathbf{k}+\mathbf{G}} | \hat{H}_{KS} | \Phi_{\mathbf{k}+\mathbf{G}'} \rangle - \epsilon_{n,\mathbf{k}} \delta_{\mathbf{G},\mathbf{G}'} \right) c_{\mathbf{k}+\mathbf{G}'} = 0 \tag{1.18}$$

Since the sum over $\mathbf{G}$ in 1.17 cannot be infinite, the number of plane waves in the expansion is determined by imposing an energy cutoff parameter E_{cut}, satisfying the condition:

$$\frac{\hbar^2 |\mathbf{k}+\mathbf{G}|^2}{2m_e} \leq E_{cut} \tag{1.19}$$

The convergence depends on the choice of the parameter E_{cut}: the larger it is the more accurate are the results but also the more demanding is the simulation.

This expansion have a very great advantage: it allows to pass from real to reciprocal space and vice versa by means of the Fast-Fourier-Transform algorithm (FFT), which has a computational complexity of $O(NlogN)$ with N the mesh size used for discretization, to solve equation 1.18 and to calculate quantities of interest.
In this work, we deal with crystal surfaces which are not periodic systems in all directions. Anyway, this type of systems can be described using a slab geometry with periodicity in the surface plane and some empty space above the surface in order to avoid interactions with its images along the third dimension. In this way it is still possible to take advantage of the FFT but the downside is that also empty space above surface is sampled and this costs computational time and memory. Therefore, in modeling a surface one has to be very careful to choose the size of the supercell along the third direction: if it's too small, images will interact with each other leading to false results, on the other hand if it's too big it will be difficult to manage computationally.

Pseudopotentials

Let's consider a single atom. The use of Coulomb potential to describe the nuclear attraction leads to computational difficulties especially in codes based on plane waves. In fact, since core electron wavefunctions are sharply peaked close to the nuclei and, consequently, all-electron valence wavefunctions have lots of wiggles near the nuclei due to the orthogonality with respect to the core electrons wavefunctions, a lot of plane waves are required for calculations and a very large kinetic energy cutoff is needed (rough estimate is around $30Z^2\ Ry$ where Z is the atomic number of the atom). To overcome this issue, since core electrons are not significantly involved in chemical bonding and materials properties, it is reasonable to consider a new system with only valence electrons that interact with ionic cores

(nucleus and core-electrons) through some effective potential. This is called *frozen core approximation* and the new potential, introduced to replace the divergent Coulomb potential, is called pseudopotential (figure 1.3a). Therefore, the valence pseudo-wavefunctions are smoother than the all-electron ones and without wiggles close to the nucleus(figure 1.3b). This further simplification is very useful because it reduces the number of plane waves requested, making the calculations faster and less demanding in terms of memory.
Since the introduction of the pseudopotential concept, one of the main challenge has been to construct pseudopotentials able to substitute satisfactorily the true potential. The first pseudopotentials were empirically generated from experimental data [35] but transferability to different types of systems was problematic. To overcome this issue, Norm Conserving PseudoPotentials (NCPP) have been introduced [36]: they were theoretically generated imposing the charge-conservation condition on the valence pseudo-wavefunctions. This ensured both a correct electrostatics outside the core region and a good transferability property. However, for some elements such as nitrogen, oxygen and transition metals, NCPP are still too "hard" as they still need a very large plane wave basis sets for expansion. Thus, UltraSoft PseudoPotentials (USPP) were developed by Vanderbilt [37] for this purpose. He relaxed the charge-conservation constrain of NCPP obtaining a much softer pseudopotential in the core region. The price to pay is an additional term, called *augmentation charge*, in calculating the electronic density in order to recover the correct amount of charge. USPP were used throughout this work. Further information about how to generate an USPP is given in appendix 5.2.

Brillouin zone sampling

During the self-consistent cycle many quantities (A), such as electronic density, have to be calculated as an average over the Brillouin

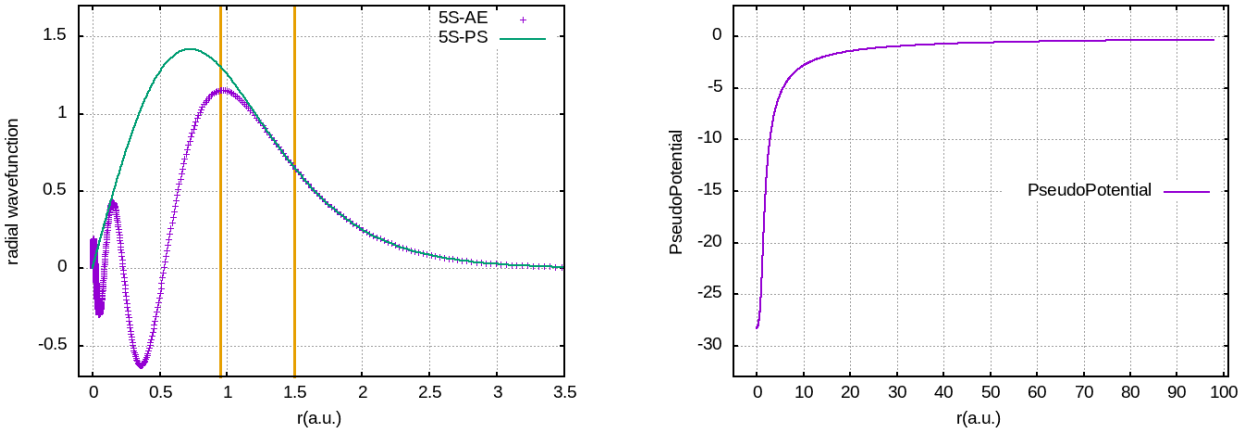

(a) (b)

Figure 1.3: Example of UltraSoft pseudopotential generated for a W atom. (a) All-electron (purple) and Pseudo (PS in green) 5S radial wavefunctions. AE 5S wavefunction have a lot of wiggles close to the origin, while PS wavefunction have a smoother behavior. Yellow vertical lines indicate the two cutoff radii used for Ultrasoft PP generation. (b) Local non-divergent pseudopotential.

zone:

$$\langle A \rangle = \frac{1}{\Omega_{BZ}} \int_{BZ} f(\mathbf{k}) A(\mathbf{k}) d\mathbf{k} \tag{1.20}$$

where Ω_{BZ} is the volume of the first Brillouin zone and $f(\mathbf{k})$ is the occupation number of the states. The integration can be efficiently performed by means of the Monkhorst-Pack methods [38], i.e. with a discrete sum over a set of representative k points. The idea is to build up an equally spaced k-point mesh in the Brillouin zone, given as input the number of k points in each directions, and then to select the inequivalent ones. The average is then calculated summing the quantity evaluated in this special points multiplied by a weight corresponding to the number of equivalent points. In this way the integral evaluation is faster and the number of k-points requested to do the average decreases with the increase of the cell size.
When metal systems are studied, since the conduction bands are partially filled and the integran function in 1.20 is discontinuous, the Monkhorst-Pack methods is very inefficient as it would require a great number of k-points. To overcome this problem it is possible to use a smoother function for the occupation number in order to smear the

discontinuous step function. In this work *Methfessel-Paxton Smearing* [39] is used which replaces the step function with its expansion on few Hermite polynomials.

1.3.2 Data processing

Once the KS equations are solved, further analysis can be performed on the system. This subsection gives an overview of the main electronic quantities and structural properties that have been calculated in this using QE.

Structural optimization

Structural optimization is a very common type of simulation which allows to find the stable equilibrium configuration of the system, minimizing energy and forces acting on the nuclei. The algorithm for structural optimization is schematically reported in fig.1.4 and is called quasi-Newton Broyden-Fletcher-Goldfarb-Shanno(BFGS) algorithm [40][41][42][43]. Starting from an initial configuration for ions and electrons, the energy of the system is calculated with a self-consistent cycle. Forces acting on nuclei are then computed using equation 1.8 and if convergence for energy and force is achieved, the optimized structure is found, otherwise ions are moved according to the forces acting on them and the cycle starts again. It should be noted that this algorithm is dependent on the initial choice of the starting configuration for the ions: it does not guarantee to end up in the actual global minimum but it can converge to a local minimum. Therefore, it is important to find a suitable guess for the initial configuration based on experimental input or from theoretical considerations.

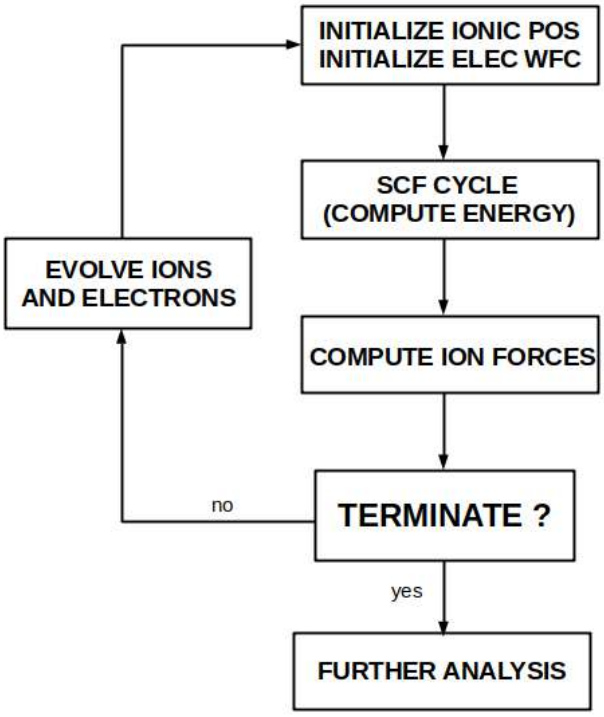

Figure 1.4: Schematic algorithm for structural optimization implemented in Quantum Espresso.

Born-Oppenheimer molecular dynamic

This is also a pretty common simulation used to investigate which is the time evolution of atoms in an interacting system although typically for very short times. Within the Born-Oppenheimer approximation, forces acting on ions can be calculated with equation 1.8 and are used to build ionic trajectories.

Energy barrier calculations

The energy barriers governing a rearrangement of a group of atoms from one stable configuration to another, such as chemical reactions, changes in surface structures or diffusion processes in solids, can be estimated if the lowest energy path can be identified. Such a path is often referred as the *Minimum Energy Path* (MEP). The energy is a complicate function of the ionic coordinates but one normally defines a "reaction coordinate" in which any point on the path is at an energy minimum in all directions perpendicular to it. Extrema of MEP are always minimum for the potential energy surface since they

must correspond to stable configurations. Along the path instead, different stationary points can occur: minima, corresponding to intermediate stable configurations, but also maxima and saddle points on the potential energy surface. This means that energy barriers can be estimated only if the shape of MEP is properly described.
The Nudged Elastic Band (NEB) [44] [45] is a method to find the MEP between a pair of stable configurations. It is a chain-of-states method in which a given number of intermediate images (geometric configurations of the system) are used to describe the reaction path and are connected by spring forces to ensure equal spacing. The initial path is usually constructed from linear interpolation of initial and final states. The images along the guessed path are then relaxed to the MEP through a force projection scheme in which potential forces act perpendicular to the band and spring forces act along the band (figure 1.5). Atomic positions of each image are then moved according to this scheme until the MEP is reached within a chosen threshold.

Density of States

The Density of States [34] is a function of energy (E) and can be calculated as:

$$DoS(E) \propto \int_{B.Z.} d\mathbf{k}\delta(\epsilon(\mathbf{k}) - E) \tag{1.21}$$

where $\epsilon(\mathbf{k})$ is a generic eigenvalue of K-S equations. In systems composed by inequivalent atoms, it could be useful to calculate also a quantity called *Projected Density of States* (PDOS) defined as:

$$PDoS(\alpha, E) \propto \int_{B.Z.} d\mathbf{k} \left|\langle \Phi^{\alpha}_{at} | \psi_{\mathbf{k}} \rangle\right|^2 \delta(\epsilon(\mathbf{k}) - E) \tag{1.22}$$

where Φ^{α}_{at} is the atomic orbital with quantum numbers α centered on the atom of interest and $\psi_{\mathbf{k}}$ is the wavefunction of the system. Since the dot product $\langle \Phi^{\alpha}_{at} | \psi_{\mathbf{k}} \rangle$ is the projection of $\psi_{\mathbf{k}}$ on Φ_{at}, it tells us which is the contribution of each atom to the density of states.

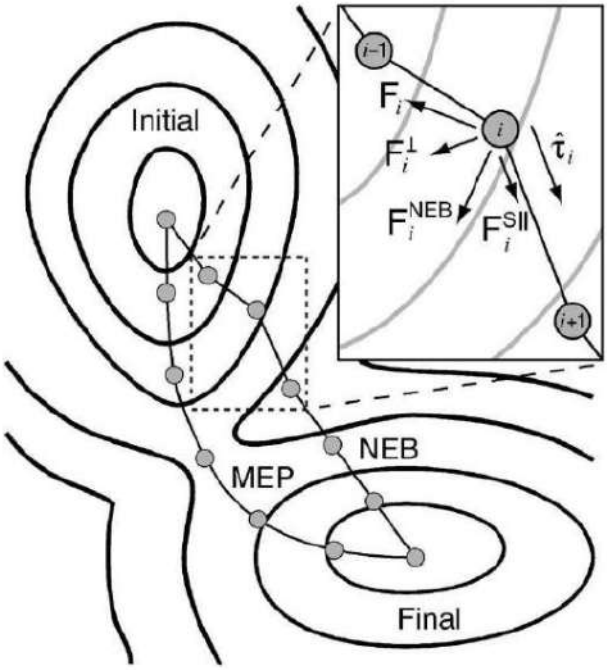

Figure 1.5: Schematic diagram of a MEP obtained by NEB calculation taken from [44]. Initial and final configurations are also shown together with the initial guessed path. Perpendicular and parallel component of the forces acting on the NEB images are also present in the box on top-right.

Moreover, it is possible to calculate which is the electronic density by means of the formula:

$$n(r) \propto \sum_i \int_{B.Z.} |\psi_{i,\mathbf{k}}(r)|^2 f(\epsilon(\mathbf{k}))d\mathbf{k} \tag{1.23}$$

where $f(\epsilon(\mathbf{k}))$ is the Fermi-Dirac occupation and the sum is over both atoms and orbitals. As for DOS and PDOS, electronic density of each orbital of each atom, i.e. what is called *Löwdin charges*, can be calculated as follow:

$$n_{at}(r) \propto \sum_{\alpha \in atom} \int_{B.Z.} |\Phi_{at}^{\alpha}|\psi_{i,\mathbf{k}}\rangle|^2 f(\mathbf{k})d\mathbf{k} \tag{1.24}$$

where we used the same notation as before and in this case the sum is only over orbitals of a single atom. Thus we can calculate which is the amount of charge in each valence orbital of each atom and which is the contribution to electron density from each atom.

Equation 1.21, 1.22 and 1.24 can be easily extended also for magnetic systems, taking into account of spin polarization.

Scanning Tunneling Microscopy simulations

Scanning tunneling microscopy is an experimental method which allows to directly study the real-space of a surface structure. A small metal tip is brought close to the surface in different points and a bias voltage is applied between it and the sample. The set up can be used in two different modes:*constant height mode* an *constant current mode*. In the constant height mode, the height of the tip above the surface is kept fixed and the tunneling current I is measured: a current map will be obtained. In the constant current mode, the tunneling current is kept fixed by changing the tip height z: the STM image is formed recording the tip heights in every point scan. The constant height mode is not the most common since the tip may accidentally crash into the surface corrugations. For this reasons both experimental and simulated STM images of the present work have been taken in the second mode.
QE offers the possibility to simulate STM images using the Tersoff-Hamann approach [46]. The tip is modeled as a locally spherical potential wall in which only the s-wave solution is assumed to interact with the surface states. It is possible to demonstrate that the tunneling current I between the tip and the sample is proportional to the *Integrated Local Density of States*:

$$I(\mathbf{r}_{tip}) \propto ILDoS(\mathbf{r}_{tip}) \tag{1.25}$$

$ILDoS$ is defined as:

$$ILDoS(\mathbf{r}) = \int_{E_F}^{E_F+eV_{bias}} LDoS(\mathbf{r}, E)dE \tag{1.26}$$

with $LDoS(\mathbf{r}, E)$ the *Local Density of States*:

$$LDoS(\mathbf{r}, E) = \sum_i \int_{B.Z.} d\mathbf{k} \left|\psi_{i,\mathbf{k}}(\mathbf{r})\right|^2 \delta(\epsilon(\mathbf{k}) - E) \tag{1.27}$$

where E_F is the Fermi Energy and V_{bias} is the bias-voltage applied between the tip and the sample.

A constant-current STM image is obtained by choosing a certain value for the current I and search for each point xy of the surface the corresponding height (z value) that has the same value of I. Since in general for a given point xy on the surface more than one z value can have the same current I, an isovalue-search algorithm is implemented, which starts from the vacuum region of the system and goes toward the sample until the given isovalue of I is found for the first time.

Band structure unfolding

QE allows to compute electronic band structure $E(\mathbf{k})$ for a given path in the reciprocal lattice. This is an important information on the electronic properties of the system but in most cases the results cannot be directly compared with experimental spectra such as those detected in Angular-Resolved Photoemission Spectroscopy (ARPES). This is due to the fact that most of the systems have to be modeled by means of a large supercells which have a larger periodicity in real space than the elementary unit cell. As a consequence, the reciprocal space of the supercell have a small periodicity and all the electronic bands fold into the Brillouin Zone of the supercell (figure 1.6).
For this purpose, QE provides an additional package that allows to map the energy eigenvalues obtained from large supercell calculations into the effective band structure, using the Popescu and Zunger algorithm [47]. The idea is that the supercell (SC) eigenvectors $\psi_{\mathbf{K},m}(\mathbf{r})$ can be expressed as a linear combination of primitive cell (PC) eigenvectors $\psi_{\mathbf{k},n}(\mathbf{r})$:

$$\psi_{\mathbf{K},m}(\mathbf{r}) = \sum_i \sum_n F(\mathbf{k}_i, n; \mathbf{K}, m)\psi_{\mathbf{k}_i,n}(\mathbf{r}) \tag{1.28}$$

Projecting $\psi_{\mathbf{K},m}(\mathbf{r})$ on all PC Bloch states $\psi_{\mathbf{k}_i,n}(\mathbf{r})$ for a fixed $\mathbf{k}_i$, the spectral weights can be calculated as:

$$P_{\mathbf{K},m}(\mathbf{k}_i) = \sum_n |\psi_{\mathbf{K},m}(\mathbf{r}) * \psi_{\mathbf{k}_i,n}(\mathbf{r})|^2 \tag{1.29}$$

This is the contributions of states $\psi_{\mathbf{k}_i,n}(\mathbf{r})$ to the SC states $\psi_{\mathbf{K},m}(\mathbf{r})$ at the same energy $E_n = E_m$. The evaluation of the spectral weight is particularly simple in plane-wave based codes since it is just a coefficient of the plane wave expansion of the SC eigenvector $\psi_{\mathbf{K},m}(\mathbf{r})$. Thus, summing up all the contributions at different energies, the *Spectral Function* $A(\mathbf{k}_i, E)$ of continuous variable E can be calculated as:

$$A(\mathbf{k}_i, E) = \sum_m P_{\mathbf{K},m}(\mathbf{k}_i)\delta(E_m - E) \tag{1.30}$$

The $E(\mathbf{k})$ dispersion can then easily be recovered from this new quantity.
Similarly, with the same package, it is also possible to calculate the contributions of each orbital of each atom to the band structure.

Core Level Shift

A typical issue in surface science is how to identify some specific atom, as well as its chemical state. This can be afforded with X-Ray Photoelectron Spectroscopy(XPS), a surface-sensitive technique. It consists in irradiating a sample with a beam of X-ray with a proper energy $h\nu$ exciting a core-electron of the atom of interest; the electron is ejected with a kinetic energy(KE) which can be measured and, knowing the work function Φ of the material and the energy of the incident beam, the Binding Energy(BE) of the core-electron can be determined as:

$$BE = h\nu - KE - \Phi$$

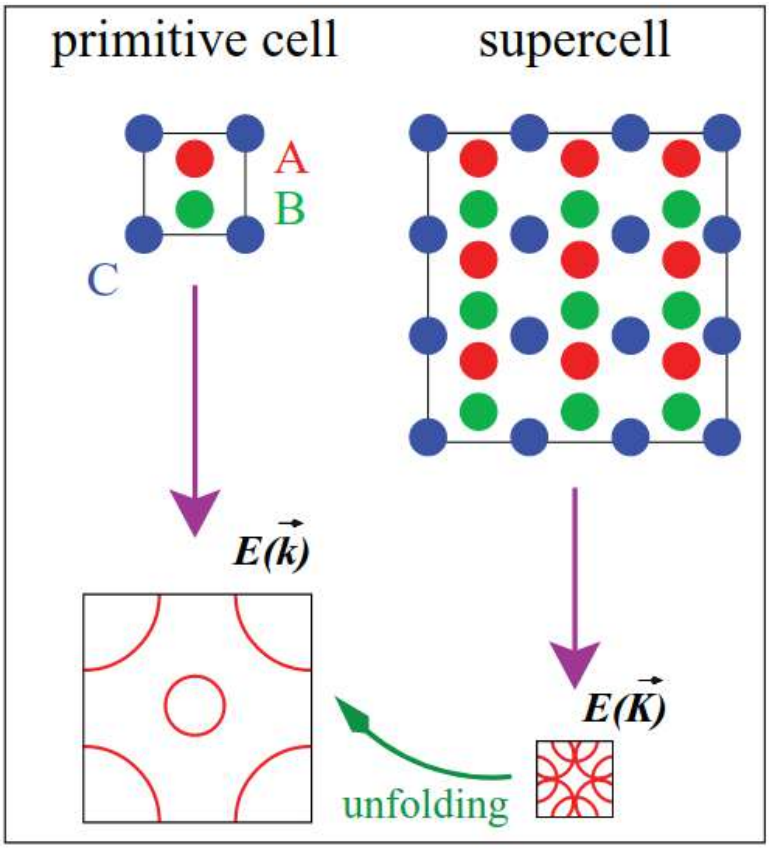

Figure 1.6: Schematic rappresentation of the unfolding process of a supercell structure. Image taken from [47].

Computationally, absolute values of the core-level binding energies (BE) are not accessible in the pseudopotential formalism, where only their differences (i.e. core level shifts, CLS) are meaningful. To this purpose, final state approximation can be used to calculate CLSs. It consists on to approximate initial and final state as follow:

- Initial state(indicated with i in the following): all electrons are present in each atom in the ground state;
- Final state (indicated with i^*): one core-electron of one atom is removed while the others are frozen in their initial state.

Given two different configurations i and j, their *Core Level Shift* is defined as the difference between all-electron binding energies:

$$CLS(j-i) = \Delta BE(j-i) = BE^{AE}(j) - BE^{AE}(i) \qquad (1.31)$$

with

$$BE^{AE}(i) = E^{AE}_{tot}(i^*) - E^{AE}_{tot}(i)$$

where $E_{tot}^{AE}(i^*)$ and $E_{tot}^{AE}(i)$ are all-electrons total energies of core-excited and normal configurations respectively. Since we do not have access to AE total energies, BE_{tot}^{AE} can be written in terms of pseudopotential energies (E_{tot}^{PS}) as:

$$BE^{AE}(i) = BE^{PS}(i) + \Delta E_{at}^{AE-PS}(i^* - i) \tag{1.32}$$

with

$$BE^{PS}(i) = E_{tot}^{PS}(i^*) - E_{tot}^{PS}(i)$$

and

$$\Delta E_{at}^{AE-PS}(i^* - i) = E_{at}^{AE}(i^*) - E_{at}^{PS}(i^*) - [E_{at}^{AE}(i) - E_{at}^{PS}(i)]$$

where E_{at} refers to the atomic energies of the isolated atom. Thus, the *Core Level Shift* between two configurations i and j with a different core-excited atom can be calculated in terms of PS energies only as:

$$CLS(j - i) = E_{tot}^{PS}(j^*) - E_{tot}^{PS}(i^*) - [E_{tot}^{PS}(j) - E_{tot}^{PS}(i)] \tag{1.33}$$

In the present work, in order to calculate core-level-shifts, the needed PseudoPotentials with a missing core-electron have been generated using the ld1.x atomic code of QUANTUM-ESPRESSO package (appendix 5.2).

1.4 Interatomic potentials with Neural Network

The efficient modeling of the Potential Energy Surface (PES) and interatomic forces has always been a matter of debate. On one hand, ab-initio molecular dynamics trajectories are very accurate but restricted to systems sizes of hundreds of atoms and to time scales of $\sim 100ps$ since energy and forces evaluation through DFT is very heavy computationally. On the other hand, classical molecular dynamic allows larger and longer simulations but with much lower accuracy.

In the last few years, Neural Networks(NN) have been used to model the PES, allowing to perform molecular dynamics simulations with accuracy and efficiency comparable to DFT and classical simulations respectively. Among many packages available, the DeepMD package has been used in this work since it is well interfaced with LAMMPS software [48], a classical molecular dynamics code. In this section, we are going to give a brief overview about the Neural Networks and some technical details about DeepMD and LAMMPS packages.

1.4.1 Neural-Network: an overview

A neural network is a collection of artificial computing nodes connected together, called *neurons*, which allows to model unknown and very complicated functions.
Each neuron accepts N input data (x_j, $j = 1, ..., N$) and gives as output a weighted sum of them as depicted in figure 1.7a, where weights w_i are parameters of the model to be learned during a training phase. Most of the times, the weighted sum is passed through a non-linear function known as *activation function* in order to grasp non-linearity behaviors of input data.
To model very complex functions a single neuron is usually not sufficient, thus many of them are collected and connected together into layers to form a Neural Network(NN) and weights can be arranged in a matrix (W) for each layer. The type of NN that we are going to use in this work is a dense feed-forward NN where each neuron at layer $k-1$ is connected to each neuron at layer k, i.e. the input data of each neuron of the k^{th} layer are the outputs of each neuron in the $(k-1)^{th}$ layer (figure 1.7b). The number of neurons for each layer and the number of layers (L) in a NN are hyper-parameters since they have to be tuned by user and are fixed during *training*.
Training is the process by means of which we can determine the weights of input data for each neuron in order to approximate a given function $F(x)$ knowing its values in some points $x_1, ..., x_n$ by

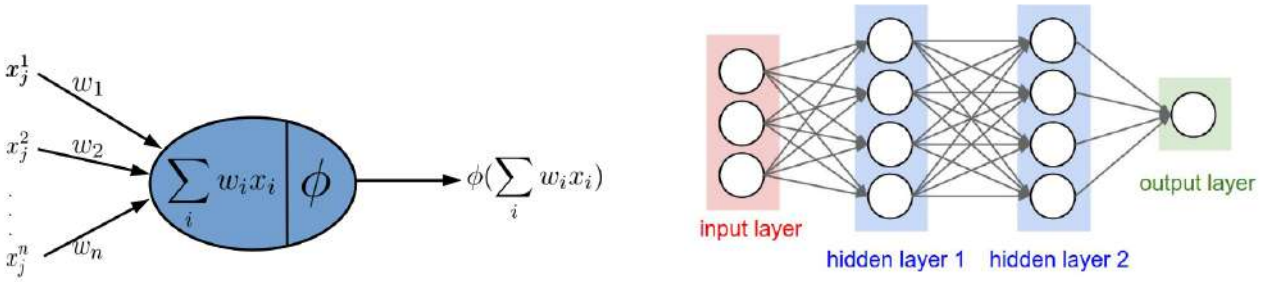

(a) (b)

Figure 1.7: (a) Schematic structure of an artificial neuron. It has many input (x_j) and one output (y). (b)Example of Feed Forward Neural Network with two hidden layer. Each layer has some neurons and each of them are connected to each neurons in the next layer.

minimizing a *loss* or *cost function*. Letting $h(x, \{W_1, ..., W_L\})$ the prediction of the NN model, where $W_1, ..., W_L$ are matrix weights of each layer, a classic choice for the loss function is the Root Mean Square Error(RMSE) defined as:

$$L(\{W_1, ..., W_L\}) = \frac{1}{2} \sum_{i=1}^{n} \left(F(x_i) - h(x_i, \{W_1, ..., W_L\})\right)^2 \quad (1.34)$$

which is a measure of how close is the prediction to the true value. Minimization of loss function is performed through an iterative algorithm, called *Gradient Descent*: weights in each neuron are randomly initialized and then updated through equation:

$$w_i(t+1) = w_i(t) - \eta \frac{\partial L}{\partial w_i} \quad (1.35)$$

where t is the number of updates, η is the *learning rate* and it can vary during training and $\partial L/\partial w_i$ the gradient of the loss function with respect to weights w_i. Minimization of the loss function is a very difficult task since there are many weights to optimize and many local minima can be present. Many other sophisticated algorithms have already been studied but they all lie on Gradient Descent Algorithm [49].

1.4.2 DeepMD package

DeepMD [50] is a package, based on Tensorflow 2.0 framework [51], which allows to model the Potential Energy Surface of crystalline systems through a Neural Network model. In particular, it allows to predict energy of the system as a sum of individual atomic contributions:

$$E = \sum_i E_i \tag{1.36}$$

where E_i is the atomic energy of the $i-th$ atom. Each atomic energy is determined by the position ($\mathbf{R}$) of the atom and its neighbors: $E_i = E_{s(i)}\left(\mathbf{R}_i, \{\mathbf{R}_j | j \in N_{R_C}(i)\}\right)$ where $N_{R_C}(i)$ is the set of neighbors of atom i within a given cutoff radius R_C.
As a consequence, forces acting on the $i-th$ atom can be calculated as:

$$\mathbf{F}_i = -\frac{\partial}{\partial \mathbf{R}_i} \sum_j E_{s(j)} \tag{1.37}$$

Since we want translational, rotational and permutational symmetries of the system to be preserved on the PES function as well, a preprocessing of atomic positions is needed [52]. This is achieved through a Deep Neural Network, called *Encoding Network*, which maps atomic positions into ad-hoc "descriptors" of the atomic chemical environment with all the symmetries of the system [50].
In order to fit the PES function, outputs from the encoding network are passed through a feed forward NN, called *fitting network*. The loss function used for training is defined as:

$$L(p_\epsilon, p_f) = \frac{p_\epsilon}{N}\Delta E^2 + \frac{p_f}{3N}\sum_i |\Delta \mathbf{F}_i|^2 \tag{1.38}$$

where N is the number of atoms in the system, ΔE^2 and $|\Delta \mathbf{F}_i|^2$ denote the root mean square error in energy and forces respectively and p_ϵ and p_f are prefactors free to change during training and chosen by the user. Its minimization is always carried out using Adam

Stochastic Descent Algorithm [49].
Once the NN model parameters are found trough training, they can be frozen and classical Molecular Dynamic simulations carried out with LAMMPS package, using the fitted PES to evaluate forces and energies.

Chapter 2

Graphene on Nickel(111)

2.1 State of art

Since its discover in 2004 [53], graphene (G) exhibits promising technological applications in different areas including electronics, optics, gas sensors, and catalysis [54]. One of the most widely used technique to grow G is chemical vapour deposition (CVD) which involves transition metal surface as a catalytic substrate for the self-assembling of carbon atoms from gaseous hydrocarbons [55] [56]. It is an efficient method to produce large flakes of high-quality graphene but the choice of the substrate is crucial in determining the G properties.

For instance, G interacts strongly with Ni(111), Ni(110), Co(111), Co(110), Pd(111) [57] leading to chemisorption accompanied by noticeable changes of G properties [58], while on Cu(111) and Ir(111) G is only physisorbed [59] thus preserving its main properties such as semimetallicity.
Among the aforementioned substrates, Ni(111) is particularly appealing due to its excellent lattice match with G lattice parameter but its surface becomes unstable upon exposure to hydrocarbons and can undergo "clock reconstruction", with the formation of highly stable nickel carbide (Ni_2C) phase [60] [61] [62]. This structural phase transition can be followed by G growth that can occur not directly from decomposed hydrocarbons but in two steps: formation of the precursor carbide converted into G in a second step [63] [64].

The presence of nickel carbide, with the appropriate substrate pretreatment and the suitable choice of the CVD parameters, can lead to the formation of rotated domains (RG) of Graphene [64]. This is further investigated in section 2.3.
Anyhow, Ni(111) ensures the formation of high-quality G flakes, with the drawback of a strong interaction which leads to the loss of free-standing G features [65]. Nevertheless, many efforts have been done to tailor the properties of G and in many case the intercalation of atoms or molecules can be exploited to decouple it from the substrate and to modify at will its electronic properties[66][67][68][69][70][71][72]. In this perspective, the intercalation of carbon monoxide (CO) is particularly relevant, since CO is one of the simplest and most harmful molecules in atmosphere, and a system for its trapping can be of potential application in sensor or catalytic reactor [73]. In section 2.4 such topic will be investigated in more details.

2.2 Potential Energy Surface modeling

Since G/Ni(111) has been already extensively investigated, we benefit of that to exploit an approach different from simply "brute force" DFT calculations, with the aim of extending the study to more complex configurations. Up to now, ab-initio calculations have been widely used for Potential Energy Surface(PES) modeling in different atomic systems with great accuracy, but computational resources have limited their application to configurations with hundreds of atoms at most. This has been even more limiting for ab-initio molecular dynamics simulations (AIMD) since only short-time trajectories can be afforded. To overcome this problem empirical interatomic potentials such as Lennard-Jones [74] or embedded atom method [75] [76] have been introduced but at the cost of a lack of transferability. In recent years, in parallel with the rapid advances of Artificial In-

telligence, there have been many attempts to construct interatomic potentials using Machine Learning and Neural Networks techniques. Among these, Deep Potential Molecular Dynamics(DeePMD) [77] [50] is one of the most popular and many works have already been reported in literature [78][79][80][81][82].

We constructed and trained a Deep Neural Network by means of DeepMD-kit [77] package to model the PES for free pristine graphene, G on Ni(111) and Ni bulk. A first trial potential has been generated using data from ab-initio Born-Oppheneimer Molecular Dynamics(BOMD) (first generation potential) and then it has been improved adding uncorrelated configurations generated through classical molecular dynamics with the new potential (second generation potential). Finally, the second generation potential has been used to study configurations affordably with DFT.

2.2.1 First generation potential

Data preparation and training

The choice of the dataset for training and validation is fundamental to obtain a high quality potential. To this end, we performed Born-Oppenheimer Molecular Dynamics using Quantum Espresso to generate some trajectories in the canonical ensemble at constant volume (NVT) for different temperatures and configurations (table 2.1 and figure 2.1).

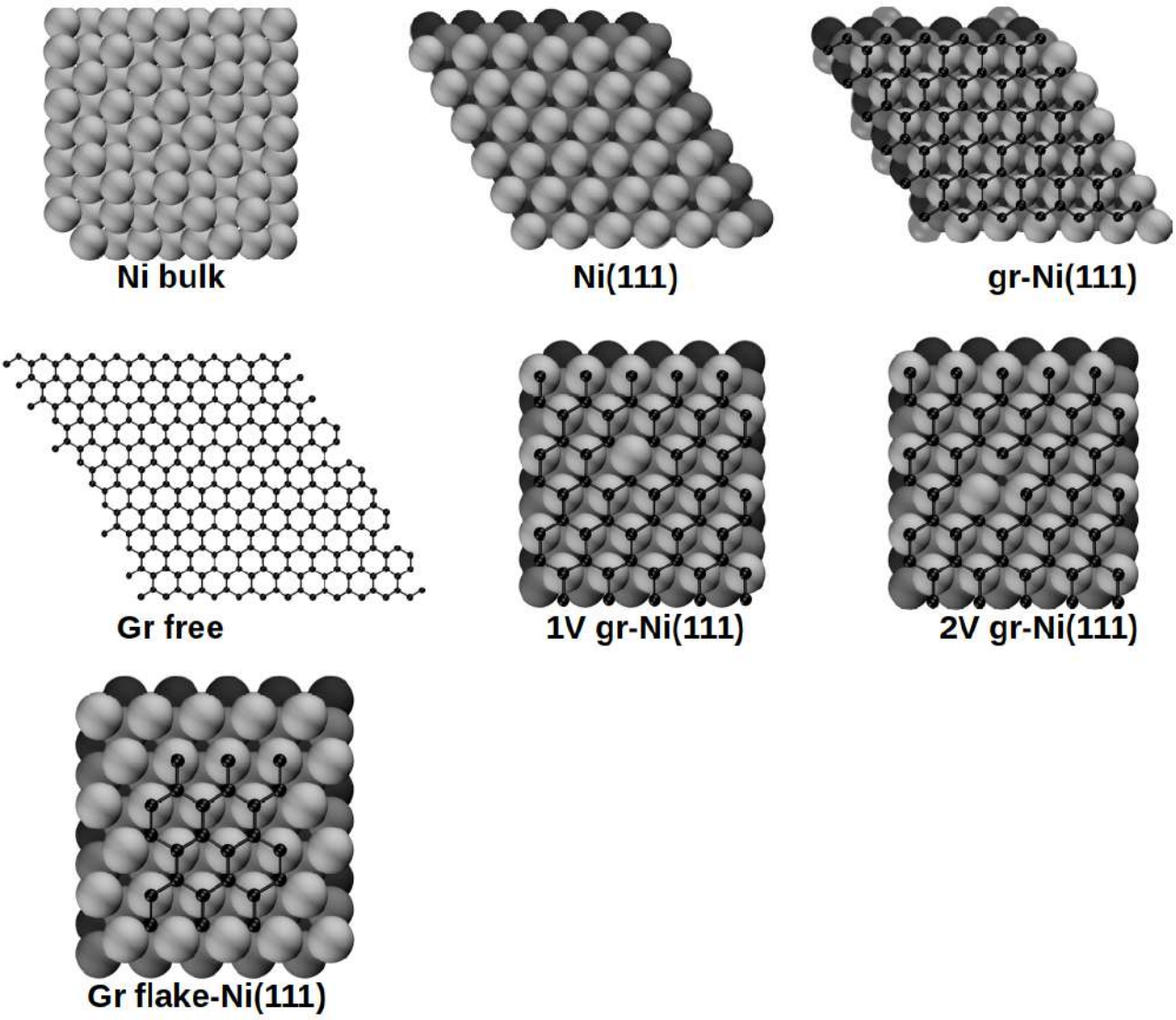

Figure 2.1: Schematic images of structures used to create the initial dataset for first generation potential creation. For each of them Born-Oppenheimer MD at different temperatures in the canonical ensemble (NVT) have been carried out and many frames have been included in the dataset as reported in table 2.1.

Structures	Unit cell repetitions	N_{atom}	Temperature (K)	N_{step}
G free	12×12	288	200	200
			600	193
			1000	195
Ni bulk conventional cubic cell	$3\times\ 3\times\ 3$	256	200	1000
			600	1000
			1000	1000
Ni slab 6 layers	$6\times\ 6$	216	200	100
			600	215
			1000	214
G/Ni(111)	$6\times\ 6$	288	200	150
			600	166
			1000	154
G/Ni(111) with 1C-vacancy	$3\sqrt{3}R°30 \times 5$	239	200	116
			600	128
			1000	127
G/Ni(111) with 2C-vacancy	$3\sqrt{3}R°30 \times 5$	238	200	165
			600	166
			1000	182
Ni(111) with G flake above	$3\sqrt{3}R°30 \times 5$	204	300	183
			600	183
			1000	182

Table 2.1: Dataset information about included frames for each structures at different temperatures.

In all cases, a time-step of $1.45fs$ and the Andersen thermostat were used. Exchange and correlations effect were taken into account through Perdew-Burke-Ernzerhof (PBE) parametrization within Generalized-Gradient-Approximations. Grimme-D2 scheme were also used for Van-der-Waals interactions. Cutoffs of 30 Ry and 200 Ry were set for plane-wave and electron density expansion, respectively. Ultra-

soft, scalar-relativistic pseudopotential with non-linear core corrections and Γ point only for sampling in the Brillouin zone were used . The dataset was formed by all the frames of all the trajectories and was split into two subsets: a *training set*, composed by 90% of each trajectory and it for training, and a *validation set*, used to validate the Neural Network while training.

DeepMD-kit [77] was used to train the potential. Concerning the encoding Network, two different descriptors were used:

- short-range descriptor (`se_e2_a`): this descriptor of local environment is constructed from both angular and radial information of atomic configurations. This descriptor is supposed to catch the short-range interactions, thus smoothing cutoff `rcut_smth` and cutoff `rcut` parameters were set to 3.0 Å and 4.0 Å respectively, such that first and second nearest-neighbors are included both in free G and Ni bulk. A 3 layers encoding Neural Network with 32-64-128 neuron units respectively was set up.
- long-range descriptor(`se_e2_r`): this descriptor of local environment is constructed from only radial information of atomic configurations and thus it should be suitable for long-range interaction description. For this reason the two cutoffs, `rcut_smth` and `rcut`, were set to 6.0 Å and 8.0 Å respectively and the same encoding network as in the previous descriptor was used.

For the fitting network, 4 layers with 64 neuron units each are employed. The learning rate starts from 0.001 and decay exponentially to $1e-7$ in 80000 steps.
The Network has been trained for 64000 epochs using a batch size of 2. Since the datasets are not balanced, i.e. the number of frames for each configurations is not the same, the probability of picking a configuration at each step of training has been set manually such that each configuration had almost the same probability to be chosen.

In figure 2.2 the cost function, calculated as in equation 1.38 during training, is reported. It converges both for training and validation set in the same way, meaning that there is no overfitting.

Testing

At this point, the NN parameters found have been frozen and the potential generated. In order to test it, a short classical molecular dynamic of 5ps (5000 steps) using LAMMPS package [48] was run for each structure in the dataset at different temperatures and energies and forces were computed. Energies and forces of two randomly chosen frames were also computed by means of an scf calculation with QE for comparison: they are reported in figures 2.3 and 2.4, respectively.

Energies predictions (figure 2.3), as confirmed by low RMSEs reported in each figures, were good but still a bit noisy due to the fact that the number of frames was not very high and more frames should be added. On the other hand, force predictions (figure 2.4) were very good for all configurations except for G flake on Ni(111). This could be due to the fact that the C atoms on the edge of the flake have a different coordination with respect to those inside, thus making the learning more difficult (see figure 2.1).
In any case, even if the potential seems to interpolate energies and forces quite well, this does not ensure that it works well in longer simulations. It is meaningful to calculate the force autocorrelation function(FACF) on the Born-Oppheneimer MD as:

$$\rho(k) = \frac{1}{(N_f - k)\sigma^2} \sum_{t}^{N_f - k} \frac{1}{N} \sum_{i}^{N} \mathbf{F}_i(t)\mathbf{F}_i(t+k) \tag{2.1}$$

where i is the atom index, t the frame index, N_f the number of frames, N the number of atoms in the configuration and k is the time-step delay. The FACF was rather high in our simulations and

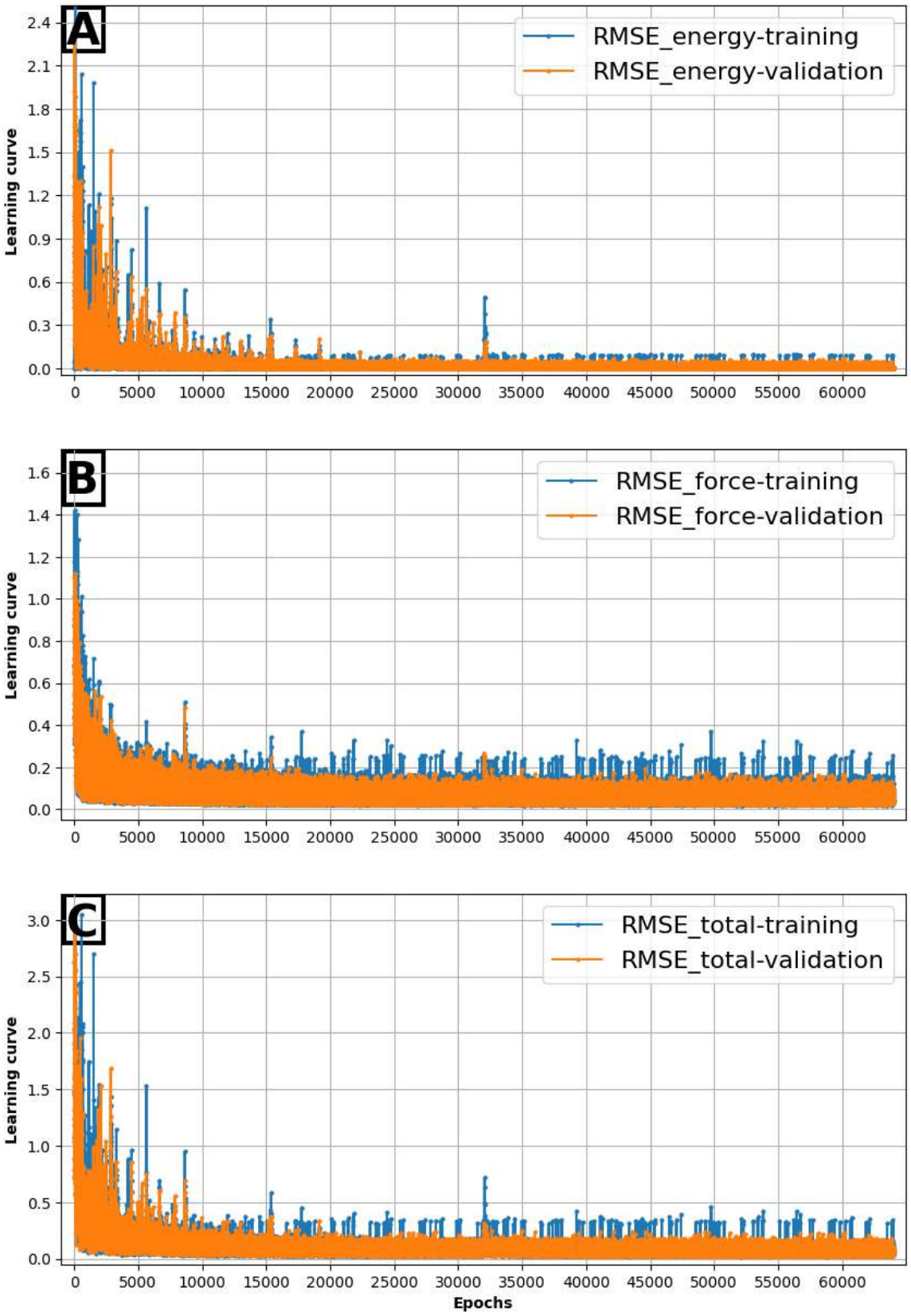

Figure 2.2: Loss functions of energy (a), forces (b) and total(sum of energy and forces)(c) are reported. Blue lines are the Root Mean Square Errors (RMSE) calculated on the training set while orange is the RMSE calculated on the validation set. Since they both converge similarly to the same value, overfitting is not present.

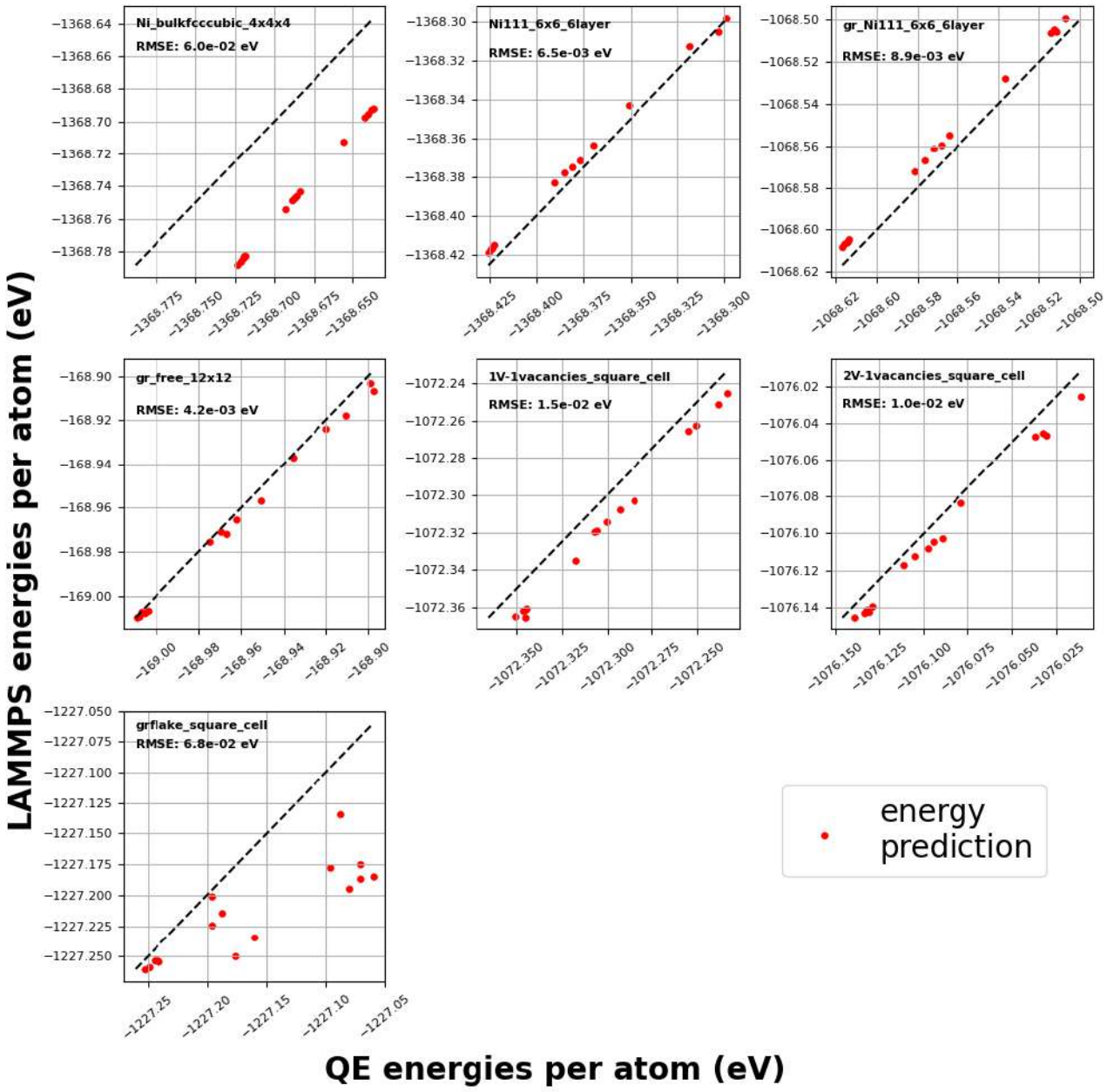

Figure 2.3: Energy comparison between predictions of the first generation potential(y-axis) and DFT calculation(x-axis). In most of the cases points are very close to the bisecting line meaning that the predictions agree quite well with DFT calculations. RMSEs calculated for each configuration on the test set are also reported

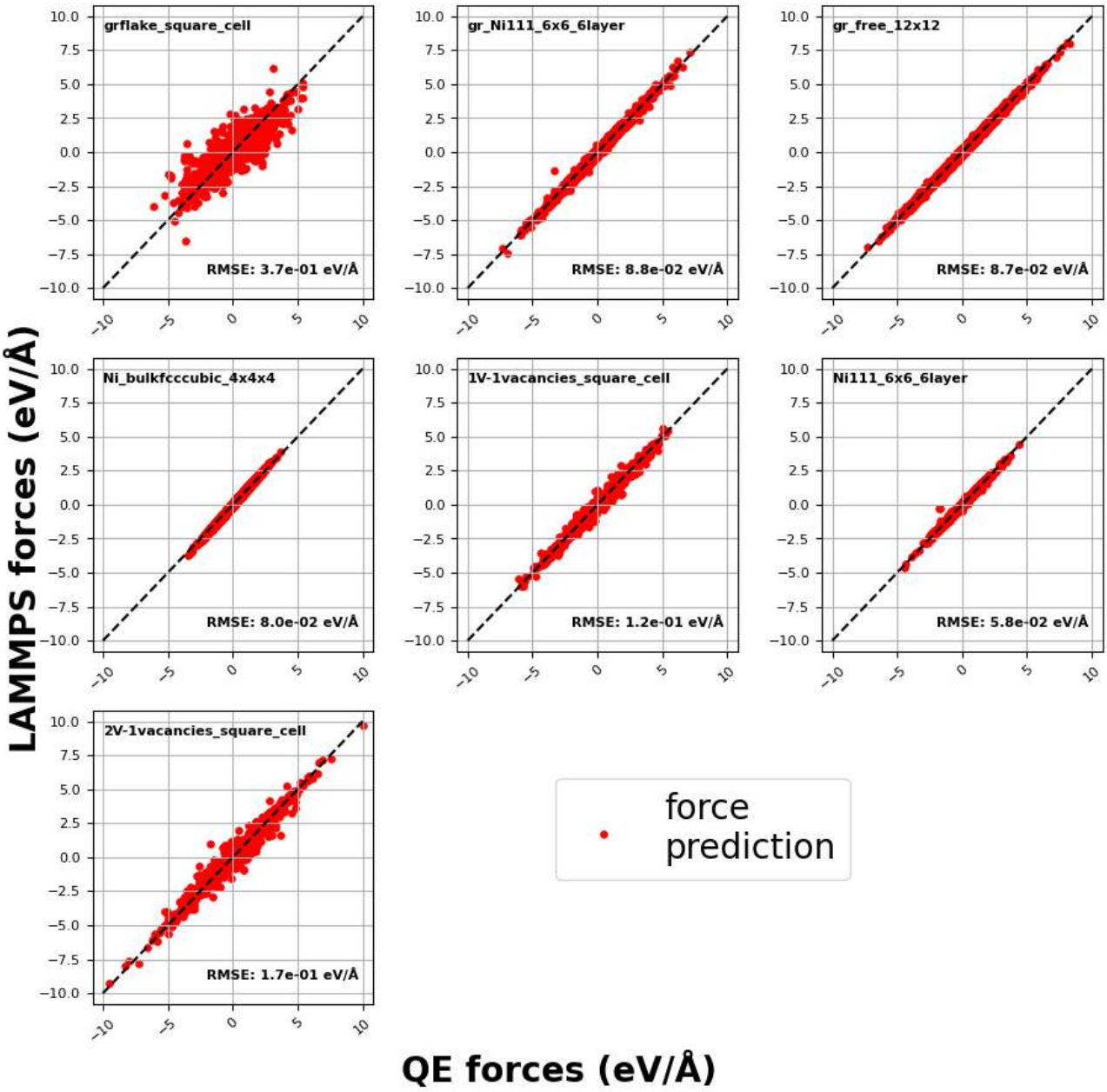

Figure 2.4: Force comparison between predictions of the first generation potential(y-axis) and DFT calculation(x-axis). RMSEs calculated for each configuration on the test set are also reported. In all cases predictions are very good.

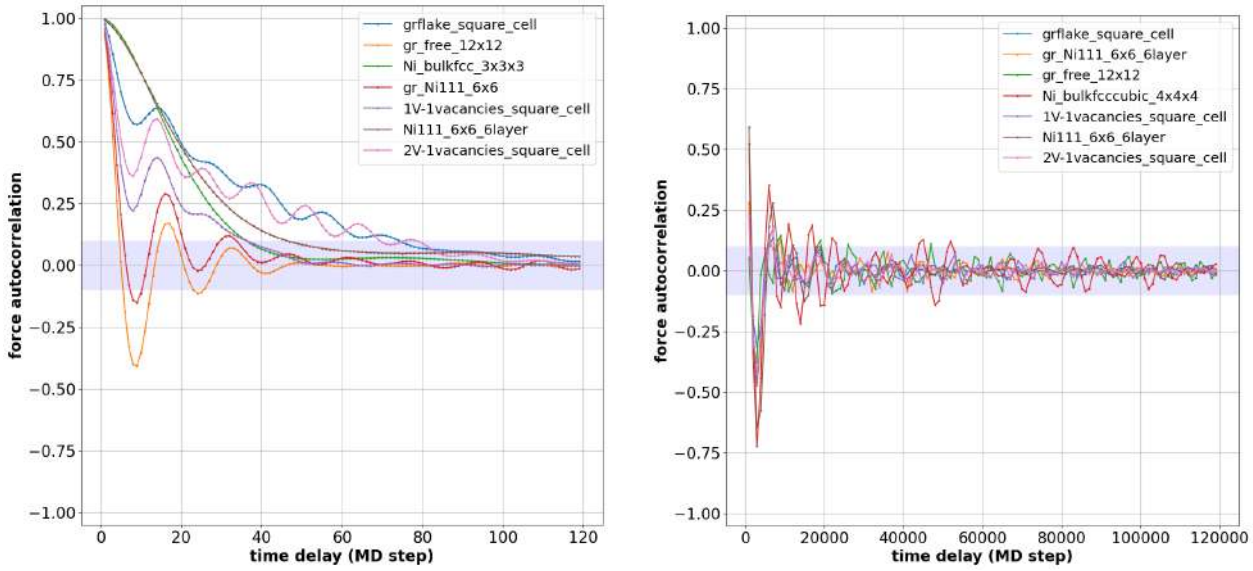

(a) (b)

Figure 2.5: Force autocorrelation function for Born-Oppheneimer (a) and LAMMPS (b) trajectories of all structures at 600 K. In the first case, computationally much more expensive, frames can be considered uncorrelated only from the 80^{th} step (FACF within the shaded regions), while in the second case from the 2000^{th}.

it went to zero only after at least 80 time-steps (figure 2.5a). This means that most of the frames in the dataset did not really carry new information to the network and that the phase space of all possible configurations was not sufficiently sampled.
Typically a second generation potential is always needed to overcome this problem and to improve its quality.

Second generation Potential

Since running long Born-Oppheneimer Molecular Dynamics to have uncorrelated frames is too expensive, the first generation potential has been used to run classical MD using LAMMPS package. In order to enlarge the dataset and to improve the transferability of the potential, it has been used also to run MD on some new structures.
For each configuration, a 3×10^5 step trajectory has been generated at 3 different temperatures (300, 600, 1000 K) printing positions, forces and energies every 1000 steps.
The force autocorrelation functions calculated as in equation 2.1 for

the new trajectories showed very weak correlations between the saved frames (figure 2.5b).
For each saved frame, energies and forces have been computed using a QE scf calculation (same parameter used as for first generation potential). The new dataset was made by all the frames with a total force smaller than $2Ry/\text{Å}$, since configurations with bigger total force are completely out of equilibrium and very unlikely to occur. In table 2.3 all the information about the new dataset are reported.

configurations	Unit cell repetitions	N_{atom}	Temperature (K)	Frame
G free	12×12	288	300	224
			600	229
			1000	153
Ni bulk conventional cubic cell	4×4×4	256	200	225
			600	225
			1000	225
Ni slab 6 layers	6×6	216	200	225
			600	228
			1000	225
G/Ni(111)	6×6	288	200	225
			600	229
			1000	157
G/Ni(111) with 1C-vacancy	$3\sqrt{3}R°30 \times 5$	239	200	264
			600	272
			1000	273
G/Ni(111) with 2C-vacancy	$3\sqrt{3}R°30 \times 5$	238	200	274
			600	274
			1000	274
G/Ni(111) with 4C-vacancy	$3\sqrt{3}R°30 \times 5$	236	200	272
			600	271

			1000	272
G/Ni(111) with 2 2C-vacancy	$3\sqrt{3}R°30 \times 5$	236	200	272
			600	272
			1000	272
G/Ni(111) with 2 2C-vacancy and 1 1C-vacancy	$3\sqrt{3}R°30 \times 5$	235	200	267
			600	271
			1000	267
G/Ni(111) with 3C-vacancy	$3\sqrt{3}R°30 \times 5$	237	200	271
			600	271
			1000	270
G/Ni(111) with 3 1C-vacancy	$3\sqrt{3}R°30 \times 5$	237	200	271
			600	270
			1000	271
Ni(111) with 1C surface	$3\sqrt{3}R°30 \times 5$	181	200	175
			600	178
			1000	99
Ni(111) with 2C surface	$3\sqrt{3}R°30 \times 5$	182	200	174
			600	92
			1000	91
Ni(111) with 6C surface	$3\sqrt{3}R°30 \times 5$	186	200	90
			600	94
			1000	180
Ni(111) with 10C surface	$3\sqrt{3}R°30 \times 5$	190	200	90
			600	90
			1000	90
Ni(111) with 20C surface	$3\sqrt{3}R°30 \times 5$	200	200	90
			600	90
			1000	90
Ni(111) with 5C subsurface	$3\sqrt{3}R°30 \times 5$	185	200	271
			600	273
			1000	273
Ni(111) with G flake above	$3\sqrt{3}R°30 \times 5$	204	300	356

			600	344
			900	19
			1000	174
Ni(111) with G flake above	$4 \times \frac{9}{2}\sqrt{3}R°30$	300	300	169
			600	169
			1000	169

Table 2.3: Dataset information about included frames for each structures at different temperatures for second generation potential.

The network has been trained using exactly the same hyper-parameters as for the first generation potential. In figure 2.6 we can see training and validation cost functions converging similarly close to zero, meaning that there is no overfitting.

As previously done for the first generation potential, in order to test the new potential, a short classical molecular dynamic of 5ps (5000 steps) using LAMMPS package was run for each structure in the dataset and energies and forces of two randomly chosen frames were computed by means of an scf calculation with QE (figures 2.7 and 2.8).

Concerning energies, figure 2.7 shows a clear improvement of prediction for Ni bulk , pristine G and G on Ni(111) with C-vacancies while Ni(111) clean surface and G on Ni(111) RMSE increases. This is due to the fact that, for computational reason, only Γ point was used for Brillouin sampling during DFT supercell calculations, corresponding to different sampling densities, since the supercells had different periodicity. This introduced some noise in the training data, making the learning process more difficult, but on the other hand increasing the Brillouin zone sampling density would have been too expensive computationally.

RMSE on force prediction instead improved or remained about the same for each configurations showing a good predictive power of the

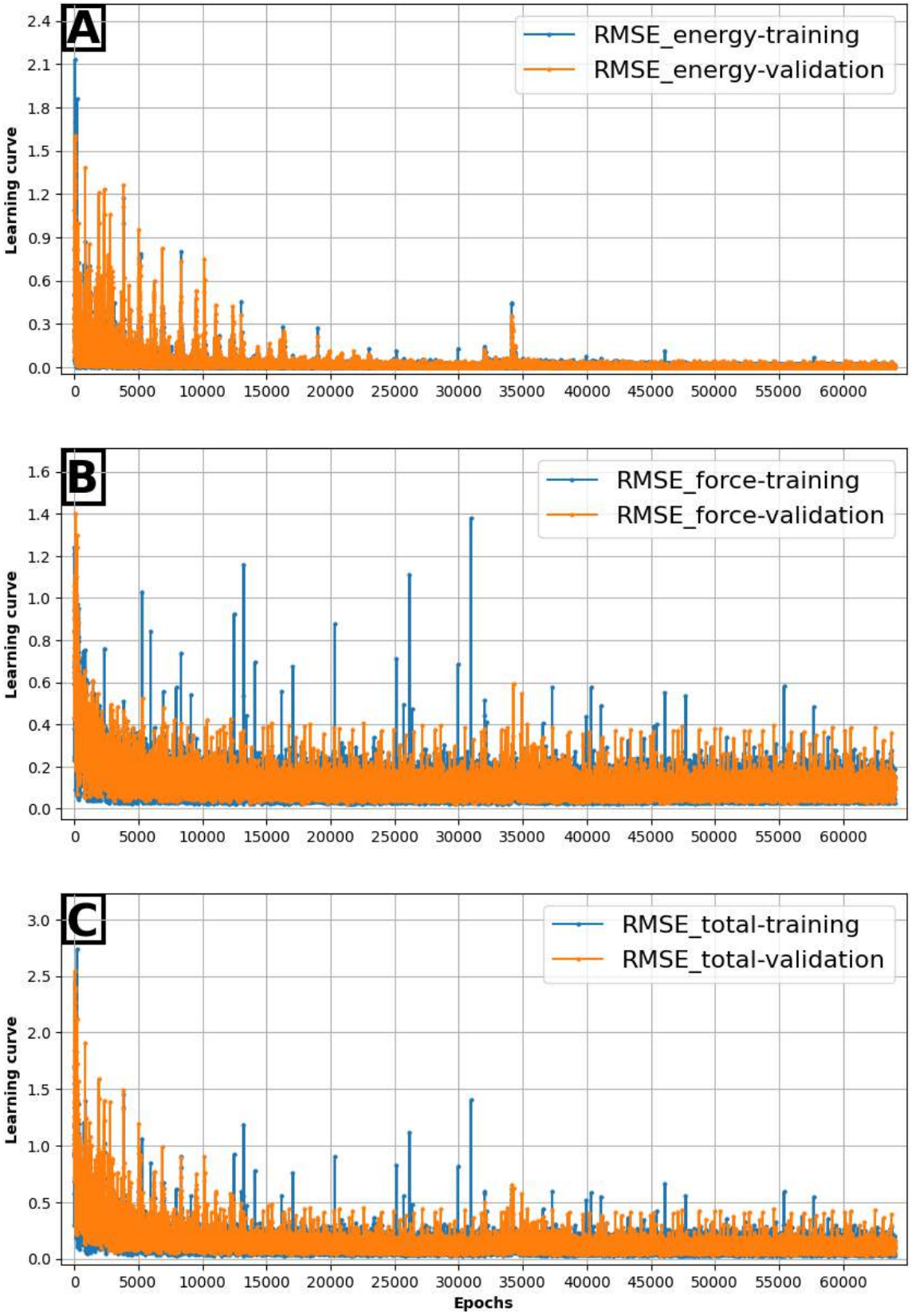

Figure 2.6: Loss functions of energy (a), forces (b) and total(sum of energy and forces)(c) are reported. Blue lines are the Root Mean Square Errors (RMSE) calculated on the training set while orange is the RMSE calculated on the validation set. Since they both converge similarly to the same value overfitting is not present.

second generation potential on these systems.
Concerning the new configurations added to the dataset, energies and force predictions in figure 2.9 and 2.10 respectively have a very low RMSE, indicating a good transferability of this potential.

2.2.2 Test on phonon dispersion

As a further validation of the new potential, the phonon band dispersion for pristine G and Ni bulk have been calculated using *Phonolammps* package, a plugin of LAMMPS package for phonon calculations.
Graphene's band dispersion was calculated along the Γ - M - K - Γ path. From figure 2.11 we see a very good agreement with literature [83]. Optical branches slightly underestimate frequencies but the shape of the two bands are very similar, while acoustic branches perfectly matches the values in literature.
Ni bulk phonon dispersion was calculated along the Γ - X - W - X - K - Γ - L path. The agreement with the results from [84] is very good, even if in this case a slight overestimate of the highest frequencies is present.

2.2.3 Different G/Ni(111) registry

The great advantage of the new potential is that very large systems can be investigated with an accuracy at DFT level (although not much different from those used for learning/training). An example comes from G/Ni(111), where configurations with different high-symmetries registries[85], i.e. top-fcc, top-hcp and top-bridge, have been separately studied but a coexistence of such domains can be detected on large scale systems ($\approx$ 100 Å), since it is due to the tiny difference in lattice parameter between Ni(111) and G (figure 2.12). Up to now, for this reason, the spontaneous coexistence of different domains of G couldn't be simulated with DFT but, with the new potential it was possible. Since the main goal of the following

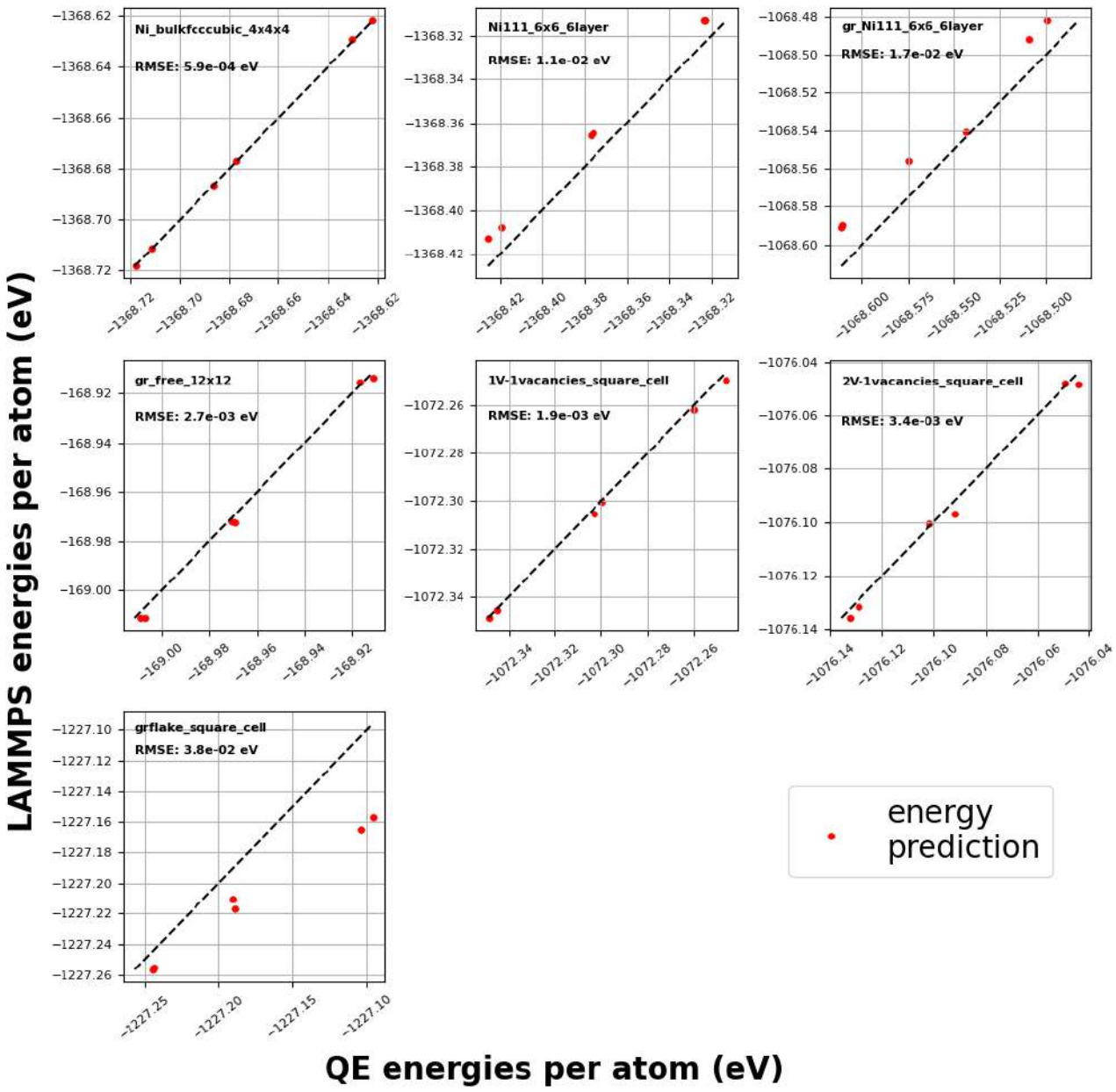

Figure 2.7: Energy comparison between predictions of the second generation potential and DFT for configurations in the first generation potential dataset. RMSEs calculated for each configuration on the test set are also reported.

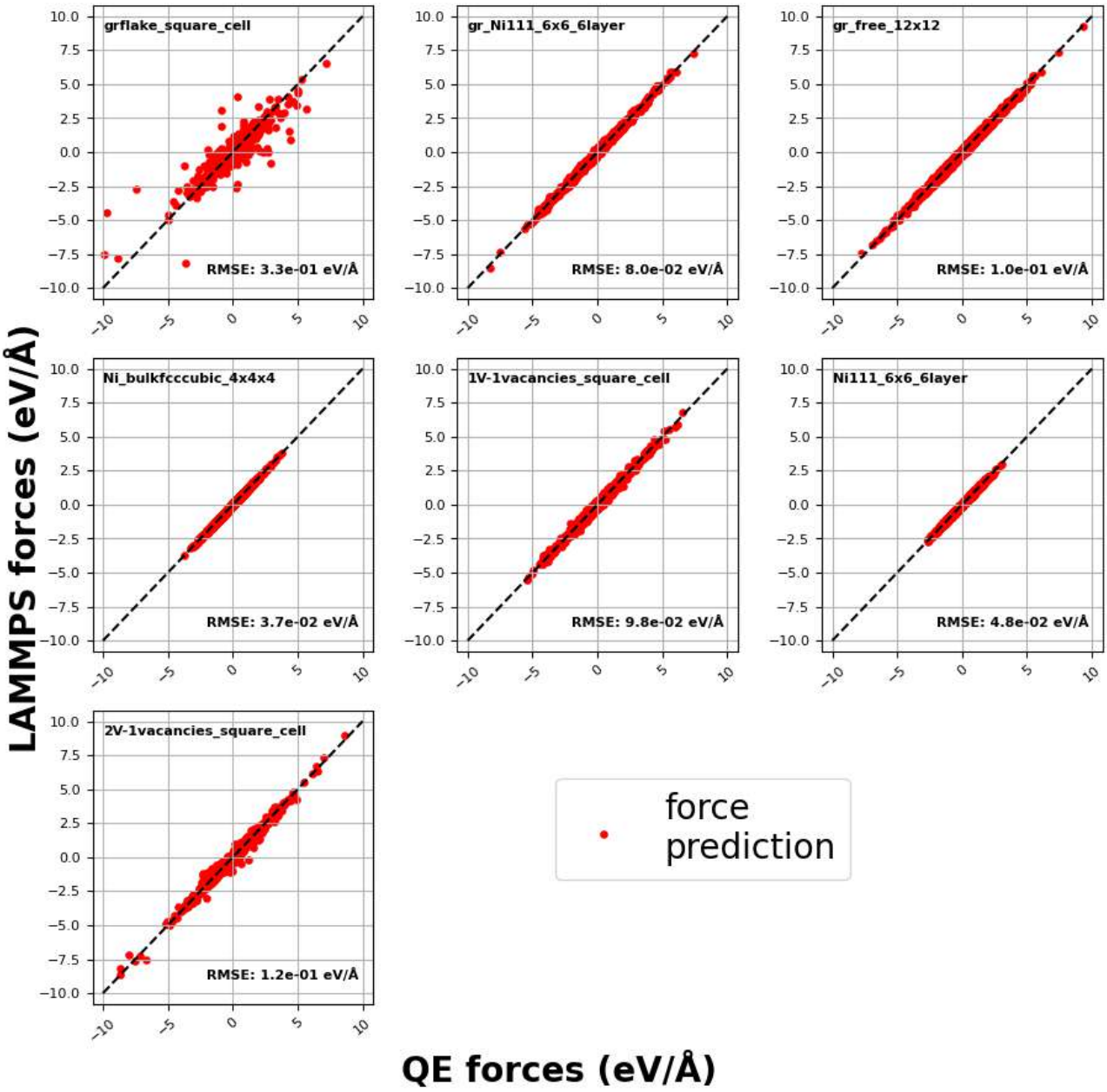

Figure 2.8: Force comparison between predictions of the second generation potential and DFT for configurations in the first generation potential dataset. RMSEs calculated for each configuration on the test set are also reported.

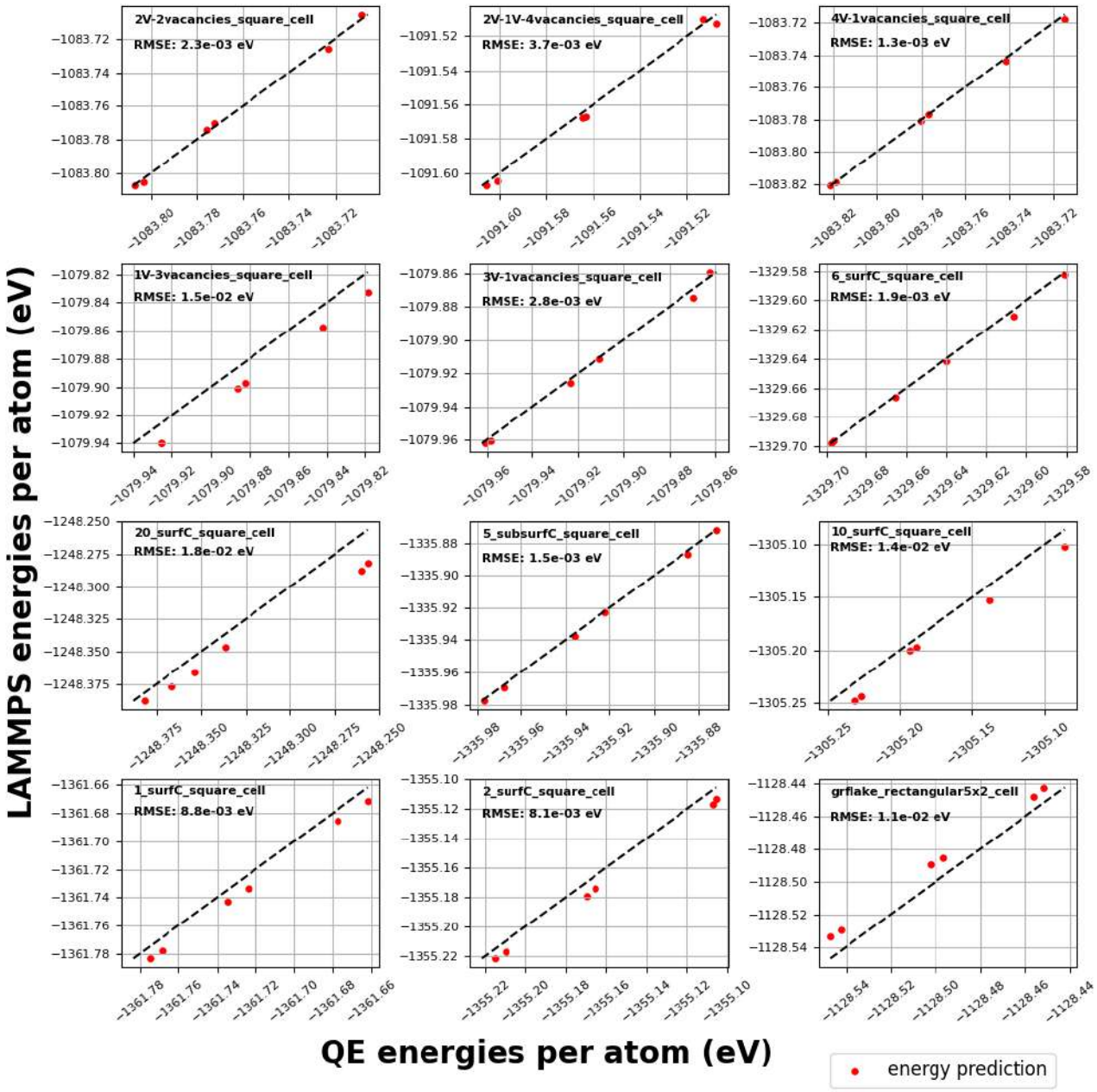

Figure 2.9: Energy comparison between predictions of the second generation potential and DFT for new configurations added in the dataset. RMSEs calculated for each configuration on the test set are also reported.

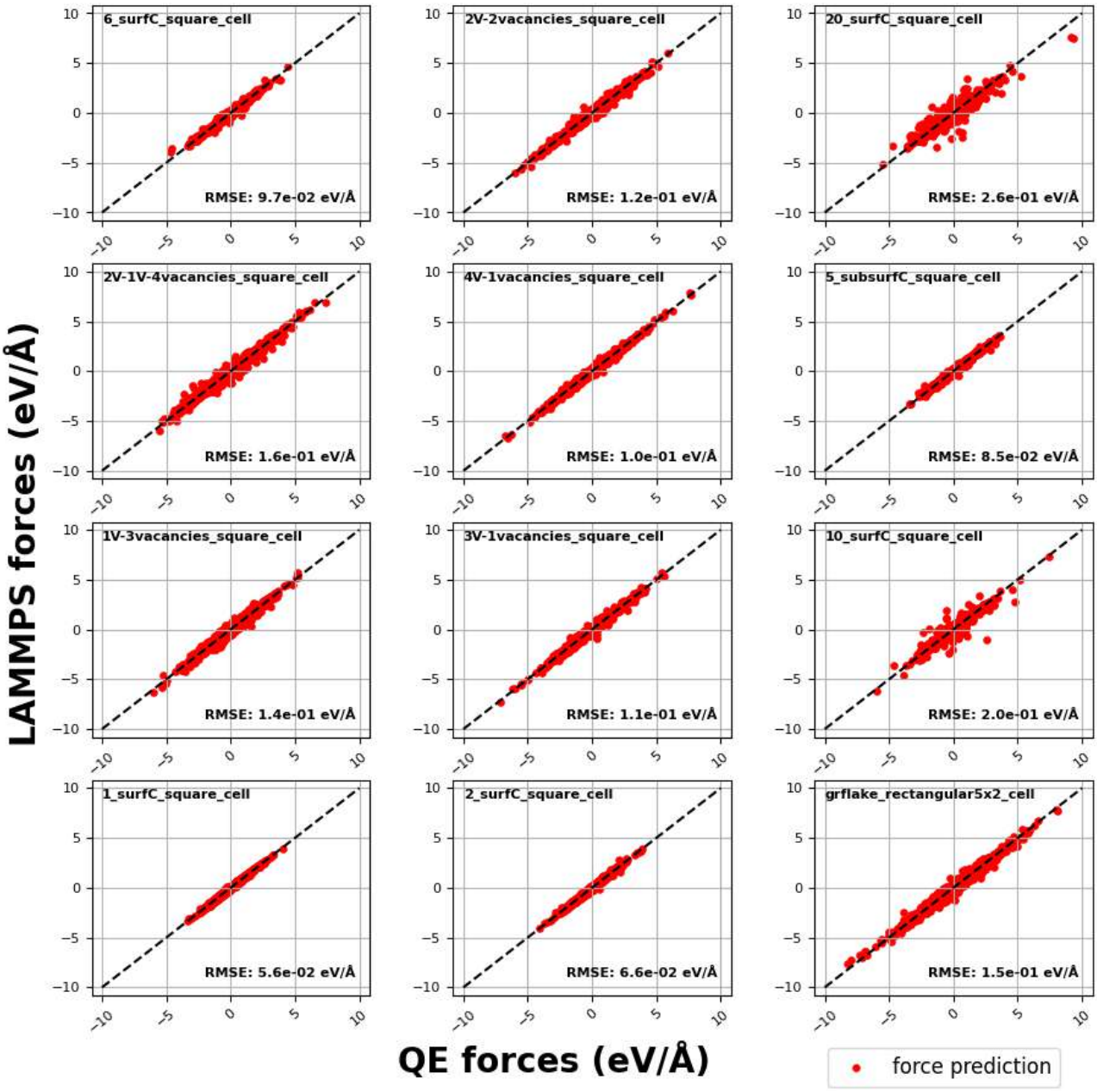

Figure 2.10: Force comparison between predictions of the second generation potential and DFT for new configurations added in the dataset. RMSEs calculated for each configuration on the test set are also reported.

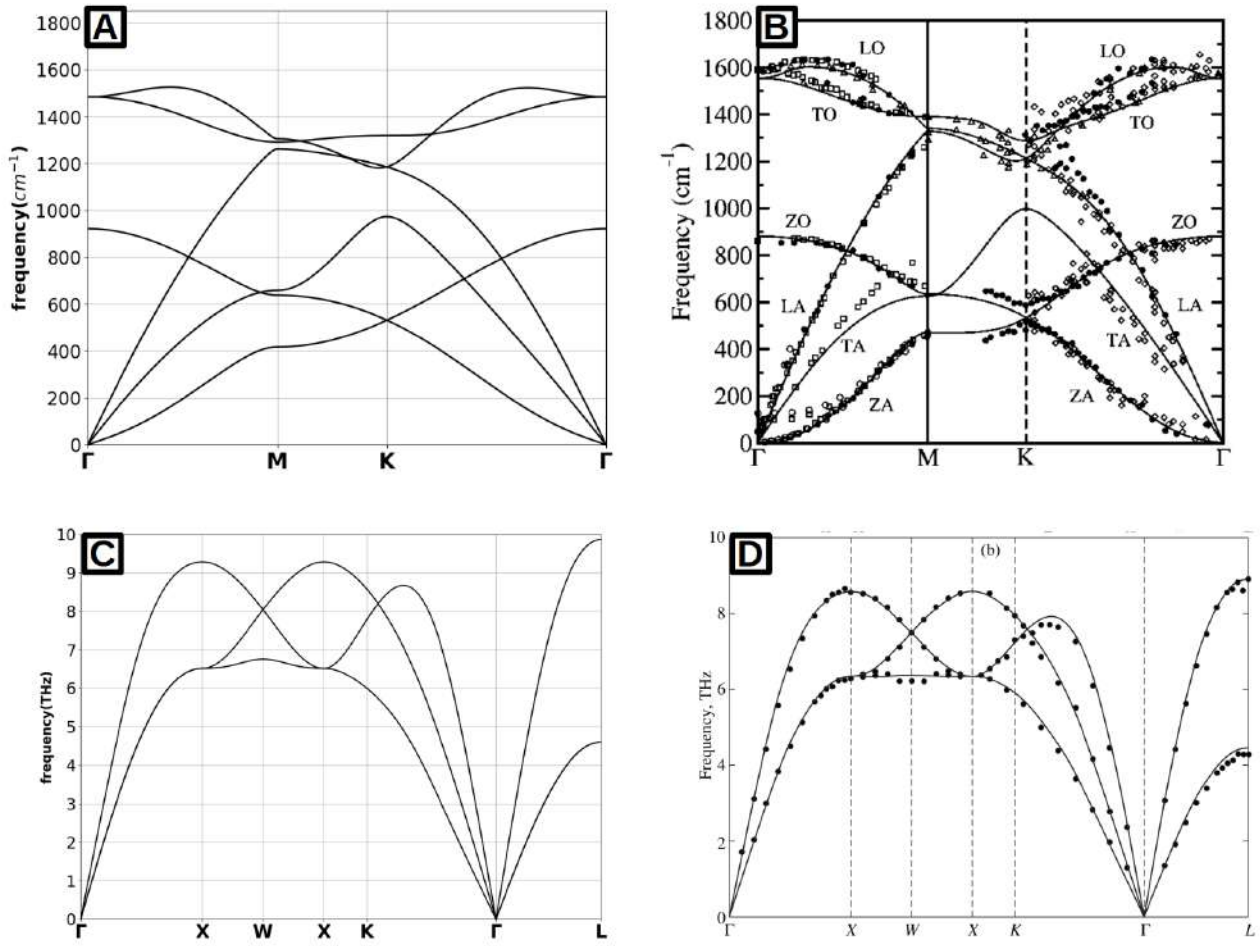

Figure 2.11: Phonon band dispersion calculated for G (a) and Ni bulk (c) using the second generation potential. They are in agreement with images found in literature [83](b) for G and [84](d) for Ni bulk.

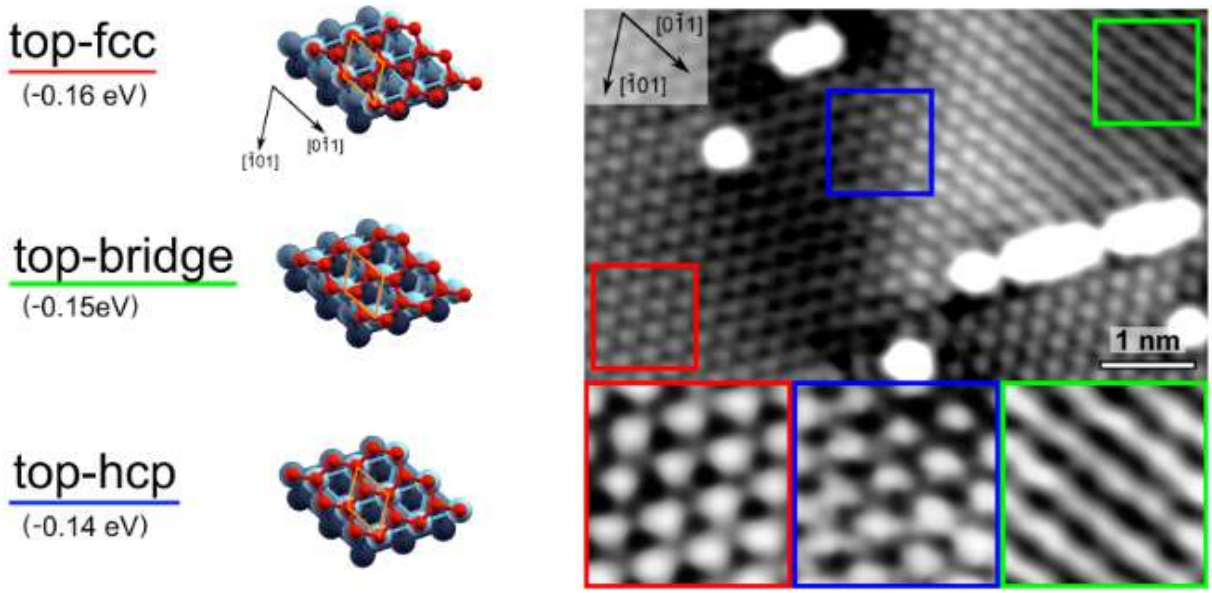

(a) (b)

Figure 2.12: (a) Three possible high-symmetry registries for G on Ni(111). (b)Experimental STM image of different coexisting G domains. Images taken from [85]

simulations is to test the new potential in a real large scale system, thermal expansions effects have been neglected.

Change of registry by translation

We first investigated the possibility of a change of registry by translation as the temperature increases. We performed molecular dynamics simulations of 50ps (50000 steps) for G on Ni(111) starting with G in the three possible high-symmetry registries and for temperatures of 300, 600, 1000 K. For the simulations, a supercell made by 6×6 unit cells of Ni(111) has been used. Starting and final registries of each simulation are reported in table 2.4. When the temperature is 300 K, G remains in the same registry throughout the simulations, while increasing the temperature G always assumes the top-fcc registry, which is the most favorable [85]. The results are compatible with NEB calculations performed on the unit cell for translation from one registry to another (figure 2.13) which predict barriers of order

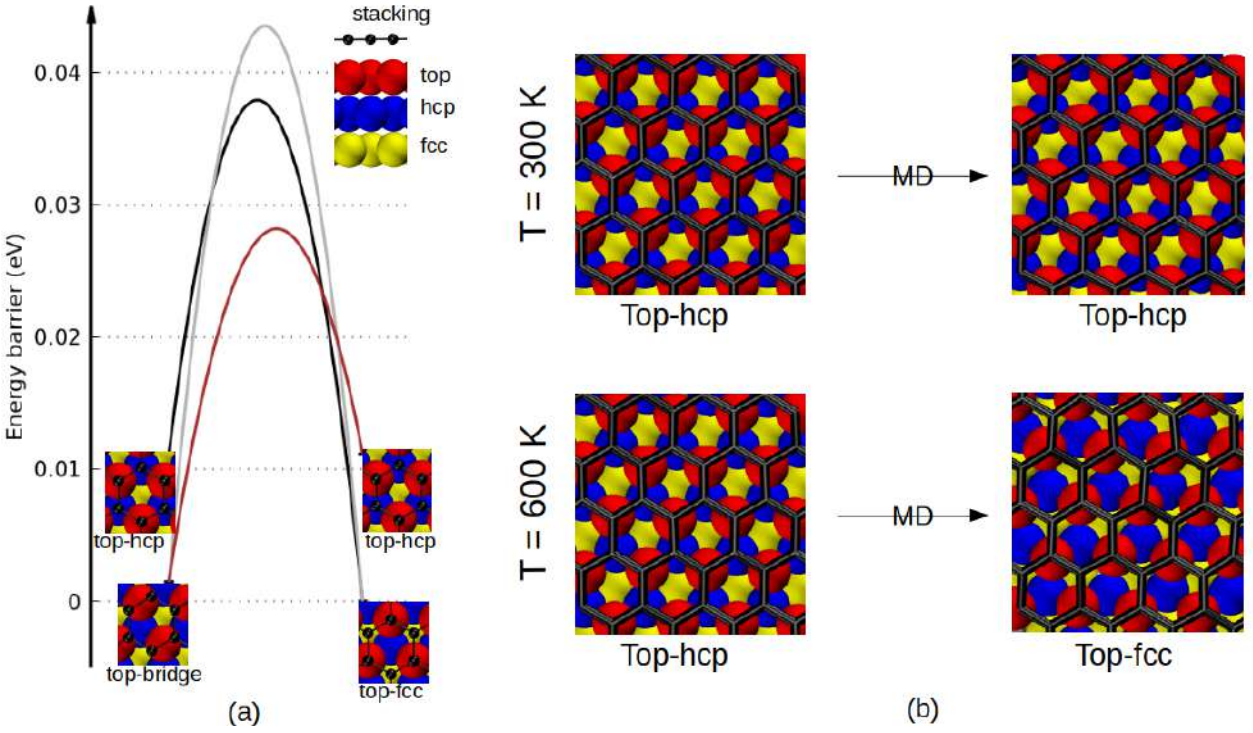

Figure 2.13: (a) Energy barriers for translation from one registry to another. (b) Initial and final configurations in LAMMPS simulations at 300 and 600 K: the starting registry in both cases is top-hcp, but ending registry changes in top-fcc only at $600K$. Stacking color scale of Ni is shown in the top right inspect of image (a).

of $0.03-0.04eV$, corresponding to temperatures of $\approx 400K$ (tab. 2.5).

Temperature (K)	initial registry	final registry
300	top-fcc	top-fcc
300	top-hcp	top-hcp
300	top-bridge	top-bridge
600	top-fcc	top-fcc
600	top-hcp	top-fcc
600	top-bridge	top-fcc
1000	top-fcc	top-fcc
1000	top-hcp	top-fcc
1000	top-bridge	top-fcc

Table 2.4: Initial and final registries of G on Ni(111) in Molecular Dynamics simulations at different temperatures.

Initial registry	Final registry	Energy barrier (eV)	T = $\frac{1}{k_B E}$ (K)
top-hcp	top-fcc	0.026	311
top-fcc	top-hcp	0.038	440
top-bridge	top-fcc	0.042	488
top-fcc	top-bridge	0.044	505
top-bridge	top-hcp	0.037	440
top-hcp	top-bridge	0.028	330

Table 2.5: Energy barriers and corresponding temperatures for registry translation predicted by NEB calculations.

Registries coexistence

In order to check the possible coexistence of different G registries on Ni(111), as observed experimentally, we cannot consider configurations with PBC applied simultaneously to G and to the Ni(111) slab. In fact, we note that:

- Independently on the use of the elementary 1×1 cell or multiple, by symmetry the result would always consist in a domain with an homogeneous registry. In order to let G accommodate on the substrate with different registries, we have to consider a large G domain on Ni, but not infinite in all the directions.

- The G domain has to be large enough in order that its adhesion could be determined by the internal C atoms and not by the edges. To estimate the minimum proper size, we have to recall that the binding energy to Ni(111) for each C atom is about 0.15 eV for the internal atoms and varies from about 0.5 to 2 eV for the atoms at the edges according to the specific binding configuration [86]. Therefore, as a rule of thumb we have to consider G domains where the number of internal atoms is at least about 20 times higher than the atoms at the edges.

Keeping in mind that, a nanoribbon of G on a rectangular supercell of sizes 150Å×15Å has been constructed. G nanoribbon was cut along the zig-zag direction in both sides as shown in figure 2.14a, contained 714/12 internal/edge atoms and was let free to move during dynamics. The Ni(111) slab was modeled with 6 layers using a lattice parameter of 2.489 Å(see appendix 5.1).
Molecular dynamics runs of $\approx 500ps$ (50000 timesteps) were performed at $300K$ (figure 2.14), 600 K (figure 2.15) and 1000 K (figure 2.16) starting from top-hcp registry for G in all cases. At 300 K G stays in top-hcp registry. Conversely, at higher temperatures top-hcp and top-fcc registries coexist alternating throughout the simulations both at 600 K and at 1000 K.

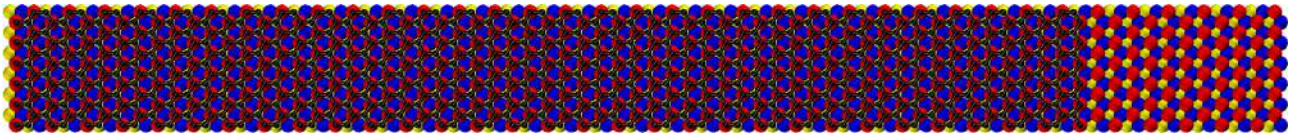

(a)

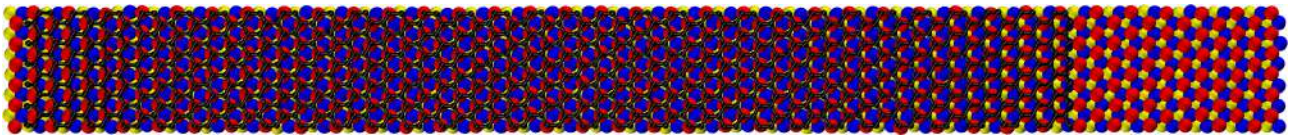

(b)

Figure 2.14: Initial(a) and final(b) configuration for MD at 300 K. G remain in the same registry throughout the simulation. Stacking color scale is the same as in figure 2.13.

Although in simulated nanoribbon the coexistence of G registries can be clearly seen, G is still constrained by PBC along the y directions: while along x direction around 15Å of clean Ni surface have been set to ensure that G images do not interact, along y direction we still have a full G layer. For this reason we constructed an hexagonal G flake on a quasi-squared Ni slab supercell of sizes 150Å×155Åwith 6 layers. In this case, since we are not constrained by PBC we used the equilibrium lattice parameter both for Ni(111) and for G layer, i.e. 2.489Å and G 2.46Å respectively. G flake was cut along the zig-zag directions in all the six directions, as shown in figure 2.17a. The side of the hexagon has been set to about 80Å since, as we al-

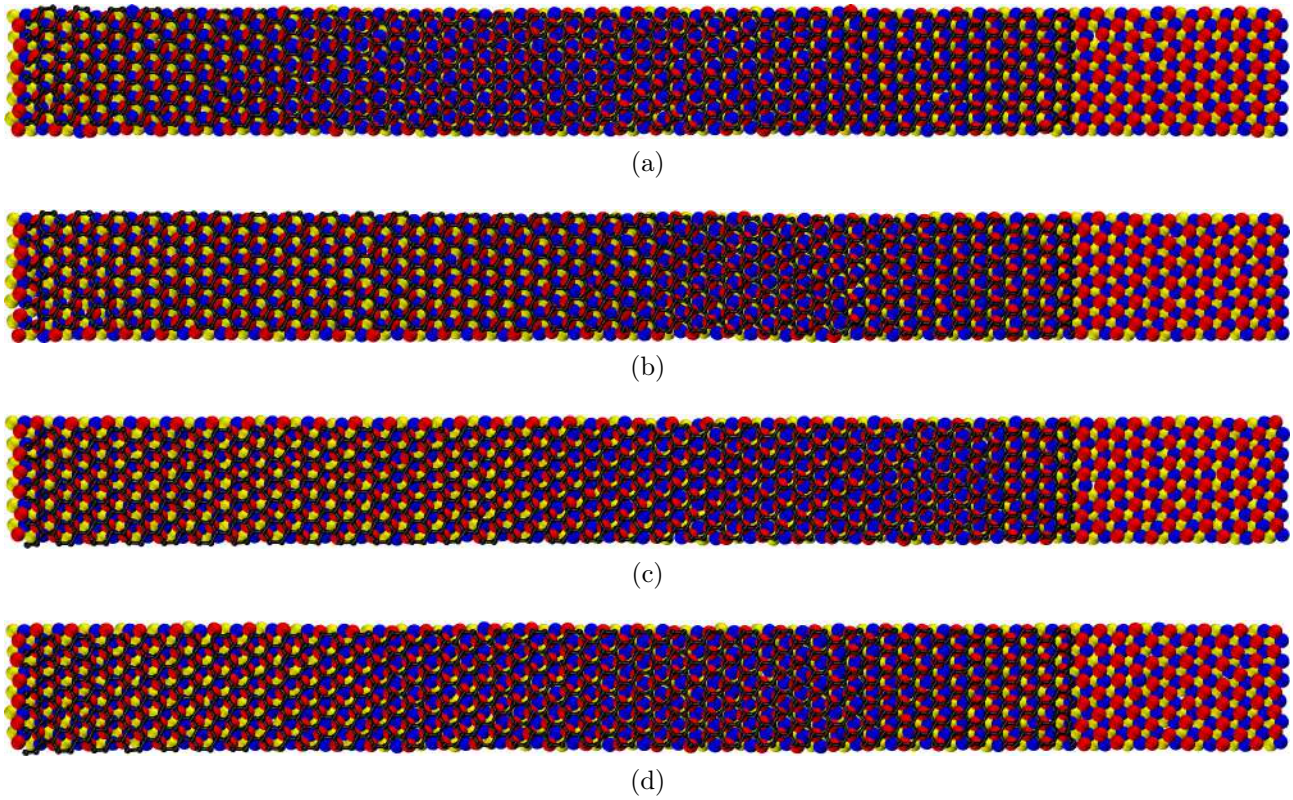

(a)

(b)

(c)

(d)

Figure 2.15: Selected frames (number 10000(a), 10900(b), 47100(c) and last (d)) from Molecular dynamic at $600K$. G registry alternates during simulation from top-fcc to top-hcp and vice versa. Stacking color scale is the same as in figure 2.13.

ready noted, the internal number of C in G layer should be at least 20 times higher than the number of atoms at the edges (4968/176 internal/edge atoms).

Molecular dynamics simulations of $\approx 500ps(50000)$at $300K$ (figure 2.17), 600 K (figure 2.18) and 1000 K (figure 2.19) starting from the configuration reported in figure 2.17a. In all cases, different registries coexists alternating throughout the simulations.

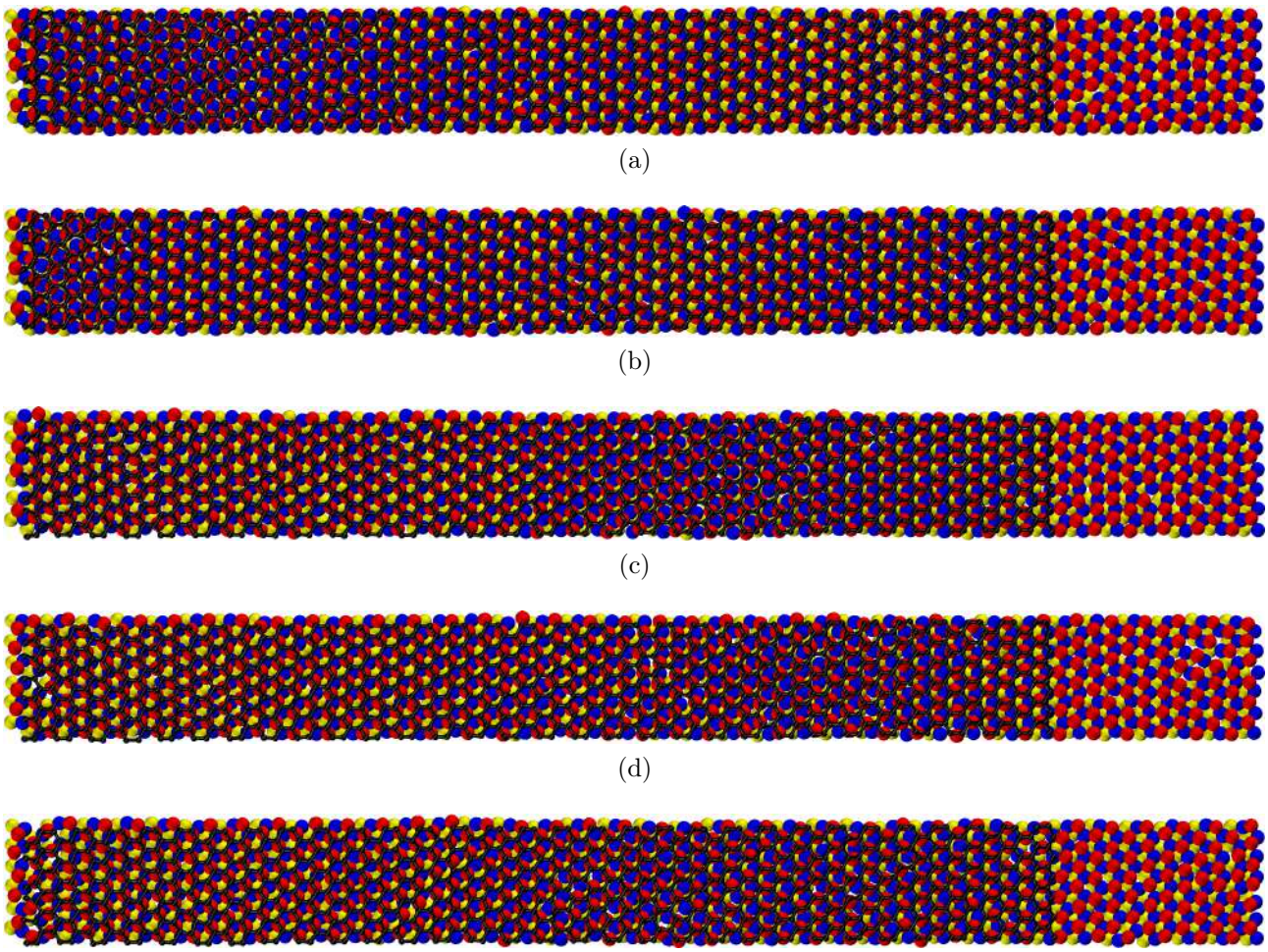

(a)

(b)

(c)

(d)

(e)

Figure 2.16: Selected frames (number 700(a), 1100(b), 16200(c), 33200(d) and last (d)) of Molecular dynamic at $1000K$. G registry alternates during simulation from top-fcc to top-hcp and vice versa. Stacking color scale is the same as in figure 2.13.

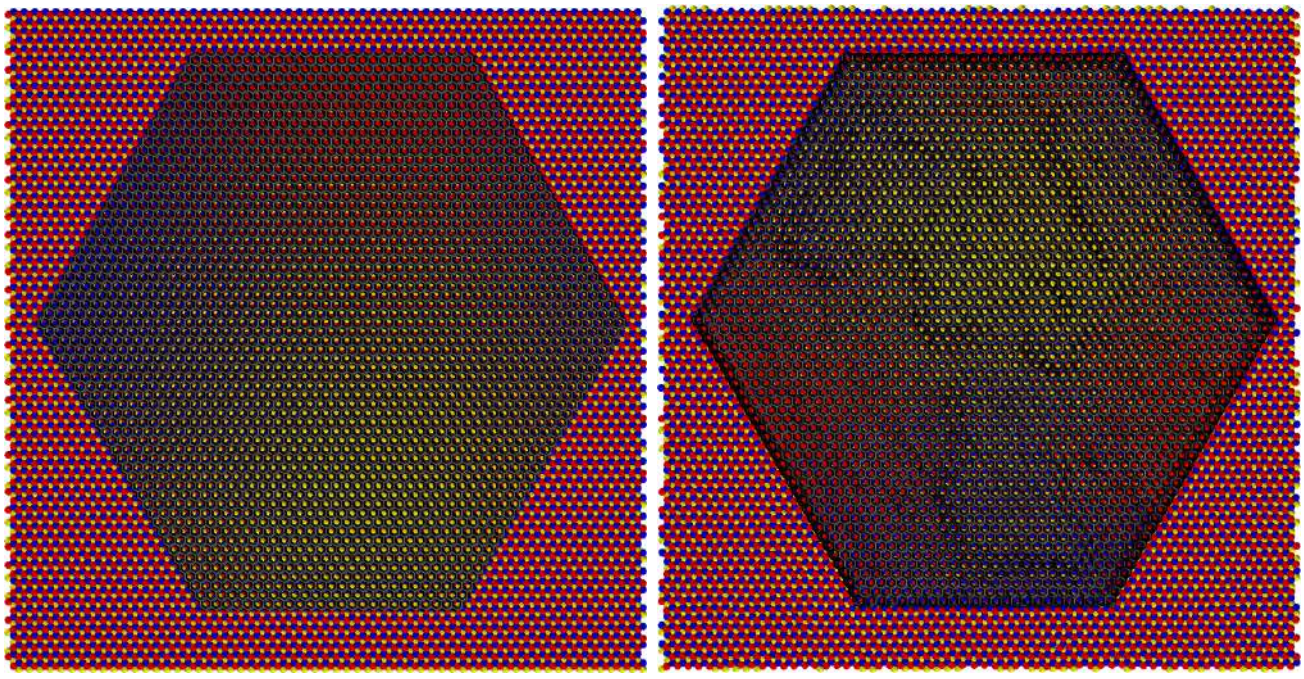

(a) (b)

Figure 2.17: Initial(a) and final(b) configuration for MD at 300 K. The coexistence of top-hcp (yellow portion on G flake), hcp-fcc (red) and top-fcc (blu) registries are clearly visible in the final configuration. Stacking color scale is the same as in figure 2.13.

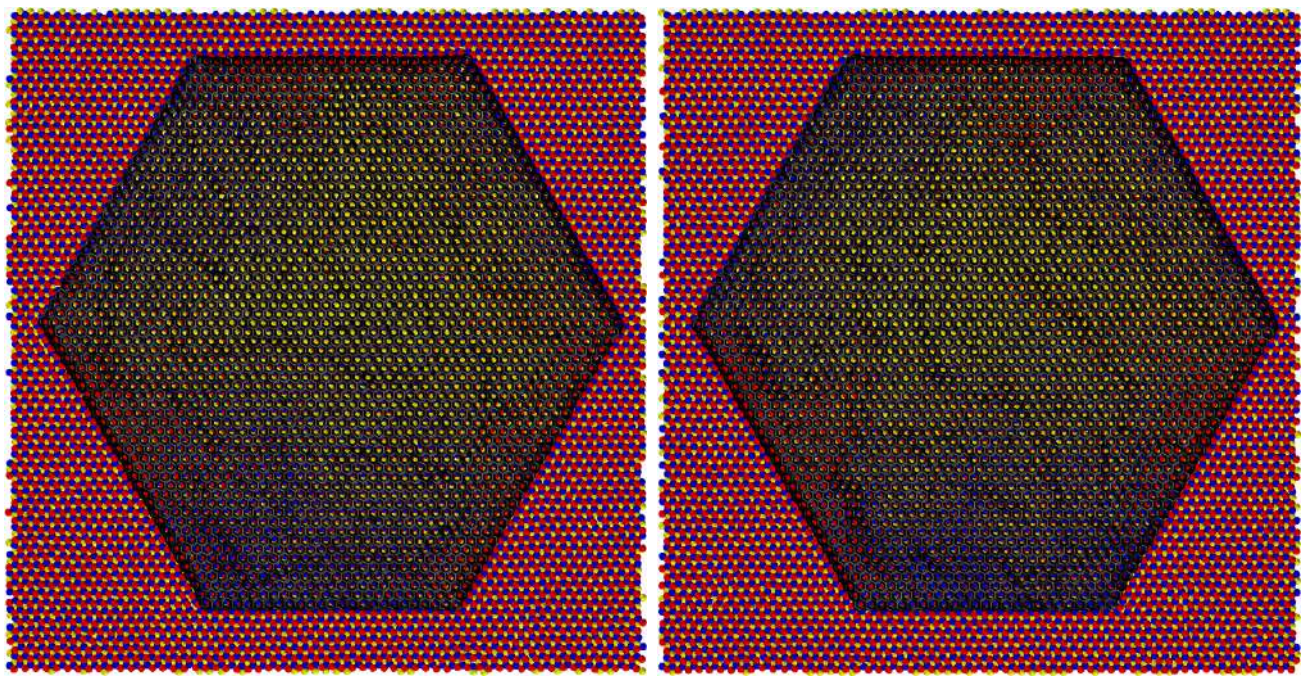

(a) (b)

Figure 2.18: Selected frames (number 1000(a) and last (b)) of Molecular dynamic at 600K. G registry alternates during simulation and the coexistence of top-hcp (yellow portion on G flake), hcp-fcc (red) and top-fcc (blu) registries are clearly visible. Stacking color scale is the same as in figure 2.13.

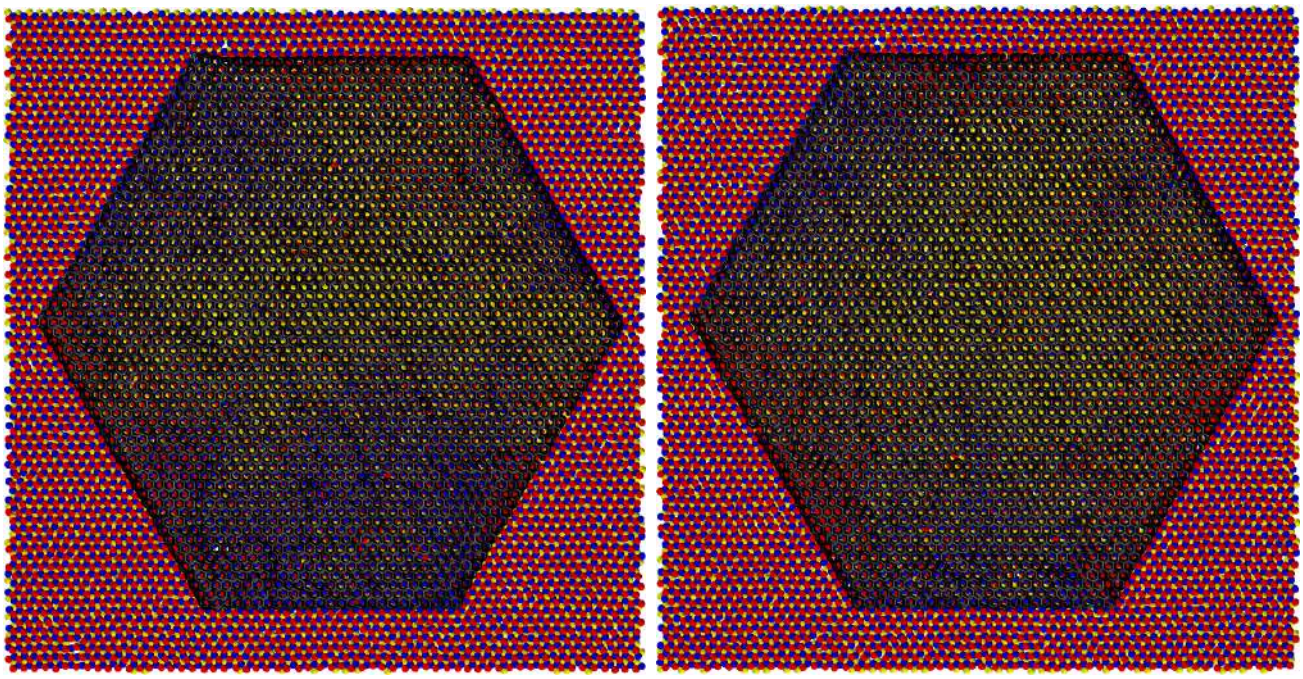

(a) (b)

Figure 2.19: Selected frames (number 2500(a) and last (b)) of Molecular dynamic at $1000K$. G registry alternates during simulation and the coexistence of top-hcp (yellow portion on G flake), hcp-fcc (red) and top-fcc (blu) registries are clearly visible. Stacking color scale is the same as in figure 2.13.

2.3 G/Ni_2C/Ni(111)

Recent experiment performed by C. Africh, G. Comelli and collaborators at CNR-IOM showed that due to an excess of carbon segregation from bulk nickel to surface upon cooling, a nickel carbide Ni_2C phase forms and is detected solely under rotated graphene (RG) but not under epitaxial graphene (EG) [64]. In particular, combined LEED analysis and STM imaging on rotated domains showed that G domains rotated by 17° with respect to the $\langle 100 \rangle$ direction of nickel lattice are the most abundant ones, followed by 13° rotated domains[87]. In this chapter we construct different G/Ni_2C/Ni(111) interface models accounting for the two types of G domains and then, by applying density functional theory, we illuminate the microscopic mechanisms governing the structural changes of nickel surface induced by carbon segregation. The present work has already been published in [88].

Computational details

Spin-polarized DFT calculations were performed with QUANTUM ESPRESSO (QE) package [27]. Exchange and correlations effects were taken into account by means of Perdew-Burke-Ernzerhof (PBE) parametrization within the Generalized-Gradient-Approximation [33]. Van der Waals interactions were also added by means of semi-empirical corrections DFT-D2 schema [89]. Cutoffs of $30Ry$ and $200Ry$ were set for plane-wave basis set and electron density expansions, respectively. The convergence threshold for total energy in all calculations was set to $10^{-6}Ry$. Ultrasoft, scalar-relativistic pseudopotential with non-linear core corrections from the QE website have been used [90]. In order to calculate Core Level Shift(CLS) of C 1s states in different carbon species, an ultrasoft pseudopotential with one missing core electron were generated, using the *ld1.x* atomic code(see appendix 5.2).

During the structural relaxations, the Brillouin-zone (BZ) integration has been performed with 4 **k** points using the smearing special-point technique and a smearing parameter of $0.01Ry$ [38]. In order to compute the atom-projected density of states (DOS) additional non-self-consistent calculations with fixed potential were performed with 10 **k** points in the BZ. Energy barriers were calculated by means of nudged elastic band method with the quasi-Newton Broyden optimization schema. In all cases a threshold on the norm of the force orthogonal to the path were set to 0.1 eV/Å.

Structural models for G/Ni_2C/Ni(111) heterostructures

The G/Ni(111) structures, EG and RG, are modeled using an hexagonal unit cell with lateral size of 10.8 Å.
Ni_2C on Ni(111) can be described with a quasi-square $\sqrt{39}R16.1° \times \sqrt{39}\bar{R}16.1°$, where the denoted angles describe the orientation of the unit cell vectors with respect to $\langle 110 \rangle$ nickel surface directions and $\bar{R}$ denotes rotation in the opposite sense to R [61] [91] [92].
Two models of G at Ni_2C/Ni(111) interface have been studied: EGC, where G is epitaxially aligned with Ni(111) and RGC, where the angle between G zigzag direction and $\langle 110 \rangle$ direction of Ni(111) surface is about 16°. As we already know, G and Ni(111) share the same hexagonal lattice with very small difference in lattice constant and thus any unit cell of Ni_2C/Ni(111) can be used to describe EGC structure. However, this cell is not suitable for our goal since it cannot accommodate G rotated by 17° or 13° or any angle close to it.
To find a simulation cell which can accommodate three different lattices (rotated G, Ni_2C, Ni(111)) a small code in python3 has been written. We fixed a mutual point of the three lattices at the origin of the coordinate system and, keeping the Ni(111) lattice fixed, we rotated the G and Ni_2C lattices around the z-axis (figure 2.20a). Structural parameters of G and Ni_2C lattices have also been varied within a few percent interval. For every set of structural parameters

and rotation angles we look for points that can be considered as mutual points of the three lattices within a certain tolerance and limiting our search to supercells with a computationally affordable number of atoms. Among all the candidates, $(6 \times \sqrt{43})R7.6°$ is the minimal cell (lateral sizes 14.9 Åand 16.3 Å) that is suitable to match all three lattices with the rotation observed by LEED. The angles between the zigzag directions of graphene and $\langle 110 \rangle$ directions of nickel are close to the observed value but not perfectly equal (15.5° and 16.1°) due to a small shear strain (figure 2.20b).
The EGC heterostructure is modeled with the same supercell, with G adsorbed in the top-fcc registry but the G lattice constant is forced to be 1.2 % larger than in pristine G. The thickness of the vacuum region in both cases is set to at least 13 Å.
After structural optimizations both for EGC and RGC, the distance between G and carbide is 2.97 Å and 3.02 Å, respectively. As an aftermath of the geometric constraints imposed by the shape of the cell, the number of graphene C atoms differs in EGC and RGC (84 and 88 C atoms respectively) so we can't compare the total energies of the two cells. Therefore, to quantify the structural stability of the two configurations, we calculated the G adsorption energy per C atom (E_{ads}) as:

$$E_{ads} = \frac{1}{N_C}(E_{G/Ni_2C/Ni(111)} - E_{Ni_2C/Ni(111)} - E_G) \qquad (2.2)$$

where N_C is the number of C atoms in G layer, $E_{G/Ni_2C/Ni(111)}$ is the energy of the total system (RCG or EGC), $E_{Ni_2C/Ni(111)}$ is the energy of the substrate without G and E_G is the energy of G layer. Both for RGC and for EGC $E_{ads} = -0.10\ eV$, which is lower than $-0.17eV$ found for G adsorption on Ni(111) in the top-fcc registry, which is the most stable [85]. This is in agreement with previous studies, where a weaker graphene-nickel interaction is reported in cases where Ni_2C is present at the nickel surface [63]. Additionally, we found that the change in G orientation does not affect the stability

of $E_{Ni_2C/Ni(111)}$ heterostructure since the E_{ads} is the same in EGC and RGC structures. Hence, contrary to G adsorption on Ni(111) where both features of chemisorption and physisorption occur [93], modest E_{ads} and sizable increase in graphene-metal distance suggest that G adsorption on $Ni_2C/Ni(111)$ substrate can be undoubtedly characterized as a weak physisorption. In the end, since EGC and RGC structures are equally stable, we cannot explain why carbide formation occurs exclusively under RG domains by inspecting only the energetic properties of these structures.

Electronic properties of G/Ni_2C/Ni(111) heterostructures

As we already know, Binding Energy (BE) of core electrons are very sensitive to the chemical environment in which the atom is. Therefore, C 1s core electrons Binding Energies can be used to identify different carbon species for $G/Ni_2C/Ni(111)$ heterostructures. Taking BE of free-standing graphene (284.4 eV) as reference, we calculated 1s CLS for C in carbide and G (both on carbide and directly supported on nickel). Results are reported in table 2.6 and they are compared with experimental results in ref [87]. Interestingly, for G directly supported on Ni(111) we obtained an average CLS of about 0.4 eV towards higher BE, with the CLS of C 1s in top and fcc sites differing by about 0.1 eV, well beyond the numerical accuracy of the method but very difficult to detect experimentally.
Looking carefully at figure 2.21a, two different coordination for carbon atoms in Ni_2C can be identified: 1/3 of carbide C atoms have a fivefold coordination (C1, green balls) while the remaining 2/3 have a sixfold coordination (C2, orange balls). For C1 specie we found a perfect match with an experimental BE value. On the other hand, the experimental BE assigned to C atoms dissolved in the first few subsurface layers is very close to the value we obtain for the C2 atoms. Therefore we suggest that the peak attributed in ref. [87] to dissolved C could be alternatively attributed to the C2 atoms of carbide. Its

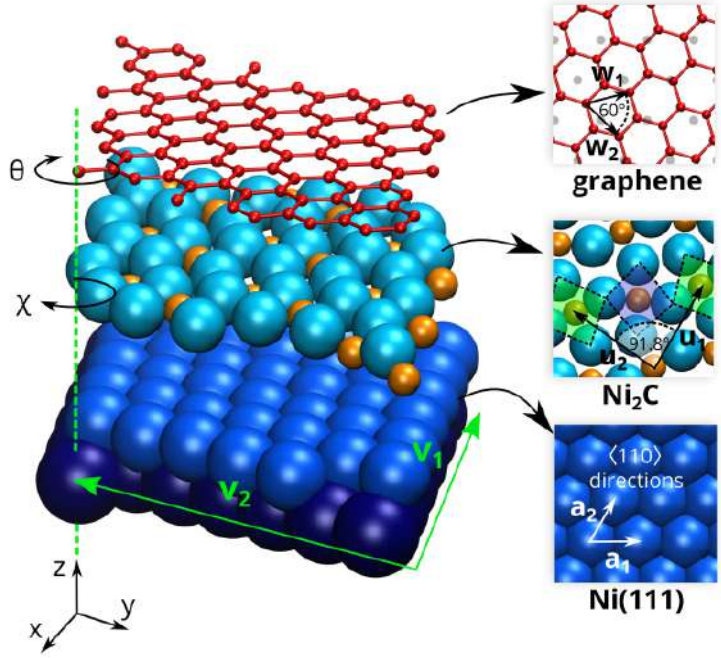

(a)

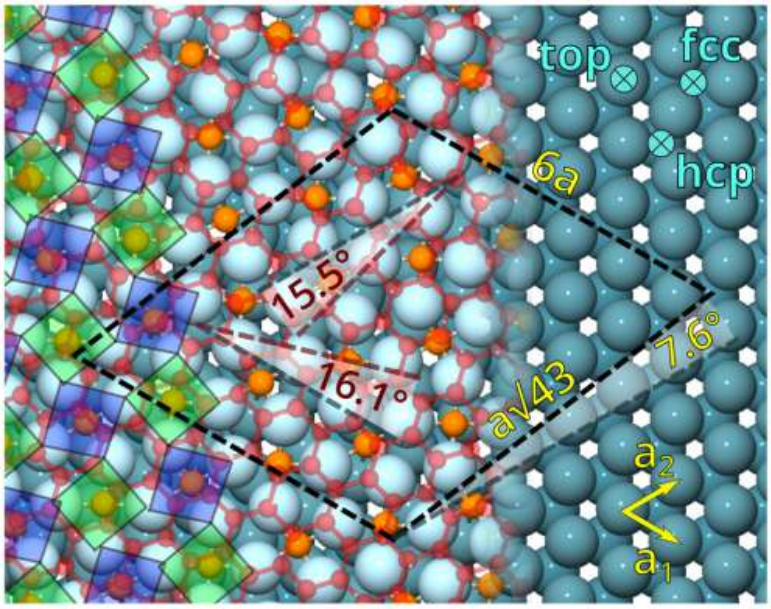

(b)

Figure 2.20: (a) Schematic diagram of the algorithm implemented for finding the simulation cell for both EGC and RGC (distance between components is enlarged to improve the visibility). The lattices of Ni(111), Ni_2C and G with the corresponding lattice vectors are depicted on the right as viewed from above. In the G panel, the sites corresponding to Ni(111) lattice are denoted by small gray dots to emphasize the G rotation. (b) $(6 \times \sqrt{43})R7.6°$ simulation cell found (black dashed line). C atoms of G (Ni_2C) are represented by red(orange) spheres. Green and violet squares on the left emphasize the typical clock reconstruction of carbide. Ni atoms of Ni(111) (Ni_2C) are depicted as dark(light) blue. Ni(111) underlying structure is revealed on the right by removing G and carbide from the image. Lattice vectors a_1 and a_2 in lower right corner define the $\langle 110 \rangle$ directions of nickel lattice. Image taken from [88].

very low intensity can be explained by structural arguments, as C2 atoms are 0.4 Å deeper than C1 atoms. Thus they are at the very end of the reach of photoelectrons whose effective attenuation length is around 4.4 Å.
The calculated BE of carbon atoms in G above carbide is equal to the free-standing G, thus confirming once again that G is decoupled from the substrate. As a further analysis for that, we calculated the charge density induced (ICD) upon the G adsorption on $Ni_2C/Ni(111)$ substrate and atomic projected density of states (pDOS) of G in both EGC and RGC (figures 2.22a-b, respectively). From ICD plots, a small electronic charge transfer of similar magnitude from G to Ni_2C has been found both in EGC and RGC. Löwdin analysis quantifies a loss of 0.05 electrons for G, irrespective of its orientation, and an average gain of 0.06 electrons on Ni atoms of carbide. A further confirmation of the very weak interaction between G and Ni_2C is the restoring of the typical Dirac cones of G (figure 2.22b), even if they appear to be slightly shifted of about 0.1 eV in both EGC and RGC.

Calculated BE (eV)		Experimental BE (eV)	
Carbide C1	283.2	Carbide	283.2
Carbide C2	283.6	Dissolved C	283.8
EGC (fcc)	284.8	EG	284.8
EGC (top)	284.9		

Table 2.6: BE of C 1s calculated and experimental [87].

Ni_2C formation at G/Ni(111)

To examine the carbide formation under EG and RG, we first investigated the influence of rotation on G binding on Ni(111) and then, adding C subsurface atoms, we discuss the microscopic mechanisms leading to carbide formation only under RG.

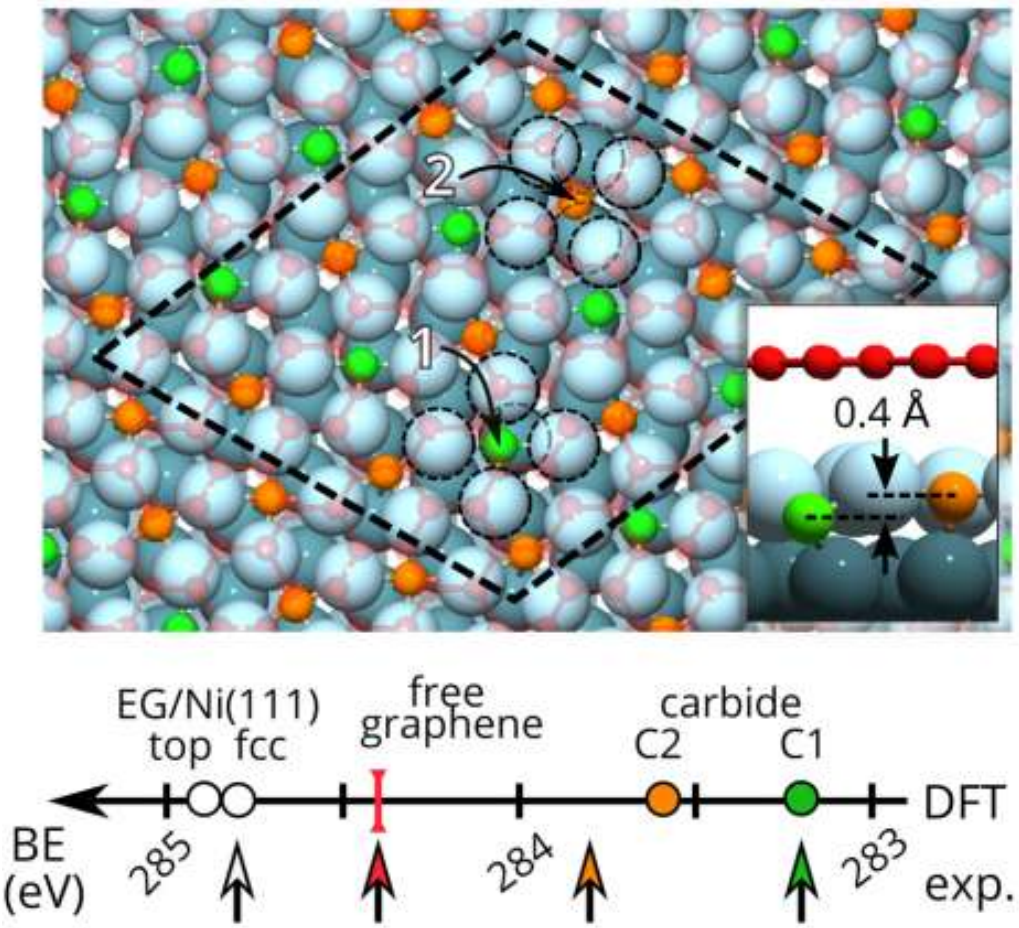

Figure 2.21: Core electron binding energies (in eV) for different carbon species. In the image above the two different coordination of carbon atoms in Ni_2C are represented by green and orange spheres and labeled by 1 and 2 respectively. Experimental values are ported as arrows. Image taken from [88].

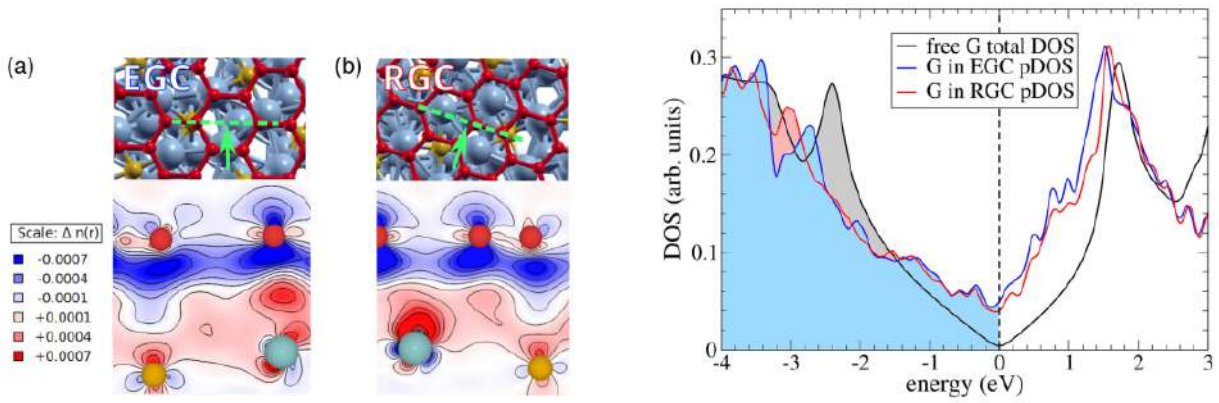

(a) (b)

Figure 2.22: (a) Charge density induced(ICD) upon G adsorption at Ni_2C/Ni(111) interface in epitaxial(EGC) and rotated(RGC) graphene. Plane used to plot the ICD is denoted by dashed green lines and thermographic scale on the left is in electrons/Bohr^3. (b) Projected Density of States averaged over C atoms of G in EGC(blue line) and RGC(red line) structures. Total DOS of free standing G is also reported in black. Image taken from [88].

Influence of rotation on G binding to Ni(111)

First of all, we tried to explain how the G rotation affects its stability on Ni(111). We constructed, using the same algorithm described in section 2.3, a simulation cell which can accommodate both Ni(111) and G rotated by 17° or 13° with respect to $\langle 110 \rangle$ directions of nickel. We found the $(\sqrt{19} \times \sqrt{19})R23.4°$ to be the most suitable candidate able to accommodate G rotated by 13.2° (figure 2.23a-b). This cell can accommodate both EG and RG and they both contain 95 atoms including 38 C atoms of graphene (indicated with C_G in the following). Simulated STM image for RG domain is in excellent agreement with the experimental one (figure 2.24). Direct comparison of the total energy of the two structures show a difference of 1.48 eV (0.04 eV per C atom) in favor of EG. This is a clear indication that G prefers to align with Ni(111). We argue that the difference in total energy of EG and RG stems from a different number of strong $C_G - Ni$ bonds in two structures, i.e. from different number of C_G atoms adsorbed in (or very near to) top sites.

To demonstrate that, using a 1x1 unit cell with two C_G atoms, we inspected three different registries for EG configurations, namely top-fcc, top-hcp and fcc-hp as already done in [**?**]. For each configuration we calculated the adsorption energy of two C_G atom pairs. With a simple algebra, from three EG configurations we extracted adsorption energies of C_G atoms at three different sites: we found that a single C_G atom adsorbed in top, fcc, and hcp site contributes to the adsorption energy of G sheet by -0.23, -0.11, and -0.08 eV, respectively. The contribution of top site is much larger than the other two: this is a firm clue that the number of C_G atoms sitting in top sites determines the stability of $G/Ni(111)$ structure. In particular, in the two structures EG and RG we have 19 and 8 C_G atoms on top sites, respectively. If we consider the other C_G atoms bound between fcc and hcp sites, the difference between the two contributions

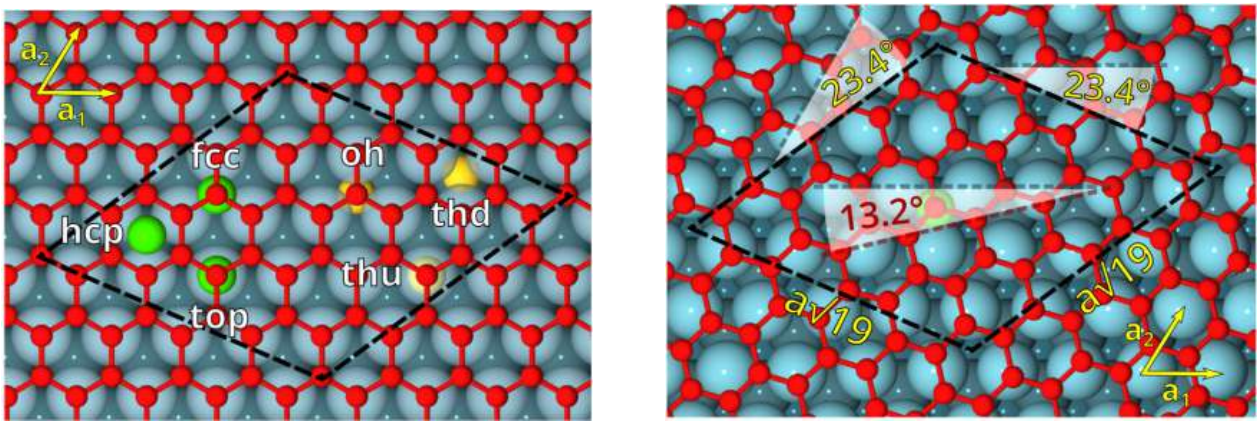

(a) (b)

Figure 2.23: Structural model of EG(a) and RG(b) made with $(\sqrt{19} \times \sqrt{19})R23.4°$ unit cell. In (a) surface and subsurface sites are reported as green and yellow spheres respectively. Image taken from [88].

is $(19-8) \times (0.23 - (0.11 + 0.08/2)) = 1.49\ eV$, which is roughly the difference in total energies of EG and RG structures.

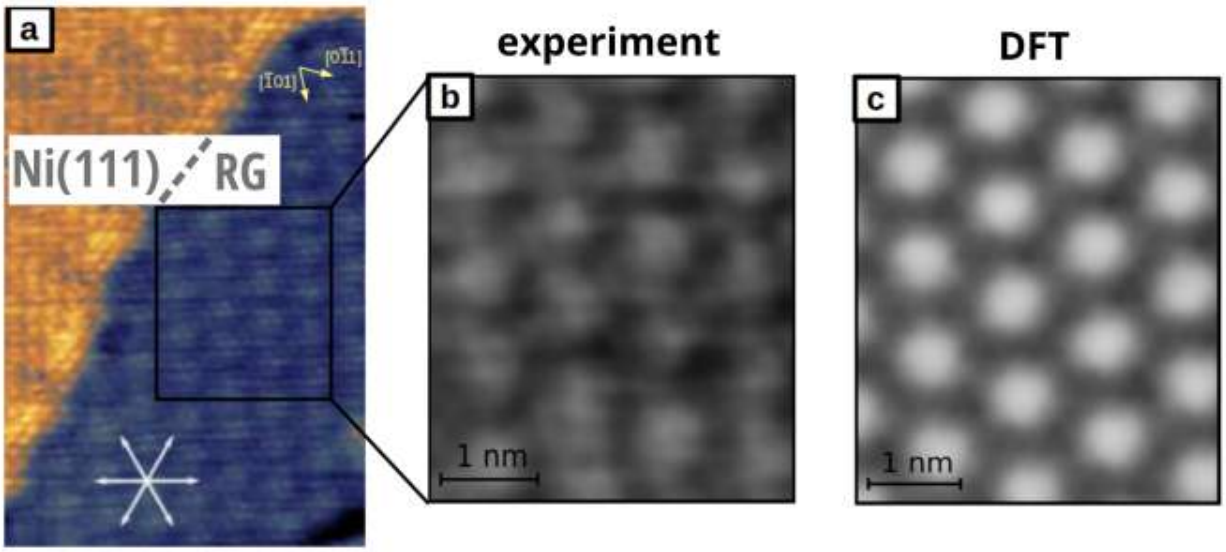

Figure 2.24: (a)Experimental STM image of RG domain with a rotation angle of 13° on Ni(111).(b) Detail of experimental STM image(V=-0.2 V; I = 2 nA)(adapted from ref [**?**] fig.S6).(c)DFT simulated image of RG structure with G rotation angle of 13.2° ($V_{bias} = -0.3eV$, ILDOS value $4 \times 10^{-4}|e|/a_0^3$). Image taken from [88].

Binding of individual C atoms

Using the same cell structure as before, we investigated the C binding in three surface sites (top, fcc, hcp) and three subsurface sites

between the second and first Ni layer (octahedral *oh*, tetrahedral-up *thu* and tetrahedral-down *thd*), both for clean Ni(111) and for EG and RG structures (figure 2.23a). The stability of all of them has been evaluated through binding energy (E_{bind}) defined as:

$$E_{bind} = E(C) + E(Sup) - E(C/Sup) \tag{2.3}$$

where $E(C)$ is the total energy of the isolated C atom, $E(Sup)$ is the total energy of the support (i.e. Ni(111), EG or RG) and $E(C/Sup)$ is the total energy of C atom bound to the support.

Support	*oh*	*thu*	*thd*	*top*	*fcc*	*hcp*
Ni(111)	7.46	6.41	–	–	6.90	6.96
EG	7.18	5.98	5.52	2.69	5.30	–
RG	7.39	–	–	–	5.99*	6.12*

Table 2.7: Binding energy E_{bind} for individual atom in subsurface sites of clean Ni(111) and EG and RG interfaces. The stars ($*$) denote the values averaged over fcc- and hcp-like sites under RG.

As reported in table 2.7, among surface sites, C atom displays very strong bindings on hollow sites for clean Ni(111) surface while it is unstable in top site, at variance with C_G atoms of graphene which prefers to bind to top site, as discussed in previous section. This suggests that the character of C-Ni bond crucially depends on the hybridization of C 2p orbitals. The overlap between the G π orbitals, formed upon sp^2-hybridization, and the Ni $3d_{z^2}$ orbitals is essential for G stability on Ni(111) [**?**]. On the other hand, a single C atom, which lacks sp^2-hybridized orbitals, prefers to bind in sites with high Ni coordination.
Furthermore, *oh* site is by far the most favorable in all three cases. Even in this case, the Ni coordination plays an important role since C atom is surrounded by six Ni atoms while in the other subsurface sites only by four. In particular, the binding of C atom in *oh* site under EG is slightly weaker under EG than RG or clean Ni(111). This is

due to the very strong interaction between the C_G atom in the top-fcc registry of EG and Ni(111) which hinders the displacement of Ni atoms in the first layer from the ideal fcc(111) positions. In RG, as demonstrated on previous section, a weaker interaction between Ni and G is present and thus nickel atoms of the first layer are free to slightly move to accommodate the additional C atom.
The *fcc* and *oh* sites are the only ones which are stable in all three the configurations thus, through NEB calculations, we investigated the possibility of a C atom in the *oh* site to segregate to the surface *fcc* site under EG and RG (figure 2.25). The calculated barriers of 2.23 and 1.51 eV in EG and RG structures indicate that the segregation of a single C atom is very unlikely to occur as long as Ni(111) surface is intact, i.e., as long as Ni atoms remain in fcc(111) positions. On the other hand, much smaller barriers of 0.36 eV and 0.17 eV for dissolution, i.e., for the inverse process of diffusion from the *fcc* to the *oh* site, suggest that the stability of C atom on the surface at room temperature is arguable.

Increasing concentration of subsurface C atoms

High barrier for surface segregation and low barrier for dissolution together with high E_{bind} for the shallowest *oh* sites indicate that an increase in subsurface C concentration is to be expected.
Following the preference of C atom to bind in subsurface *oh* site, we simulated the increase in the concentration of subsurface carbon in EG and RG structures by sequentially adding C atoms one-by-one to *oh* sites. Due to geometrical constraints imposed by the shape of the $\sqrt{19} \times \sqrt{19}R23.4°$ unit cell, the structures with homogeneous coverage of subsurface C atoms cannot be realized for any concentration. Therefore first we put C atoms into mutually distant *oh* sites to suppress the C-C interaction and then we add the C atoms in the *oh* sites in between. To quantify the deformation of nickel surface upon carbon addition, we calculated the mean absolute displacement $\langle d \rangle$

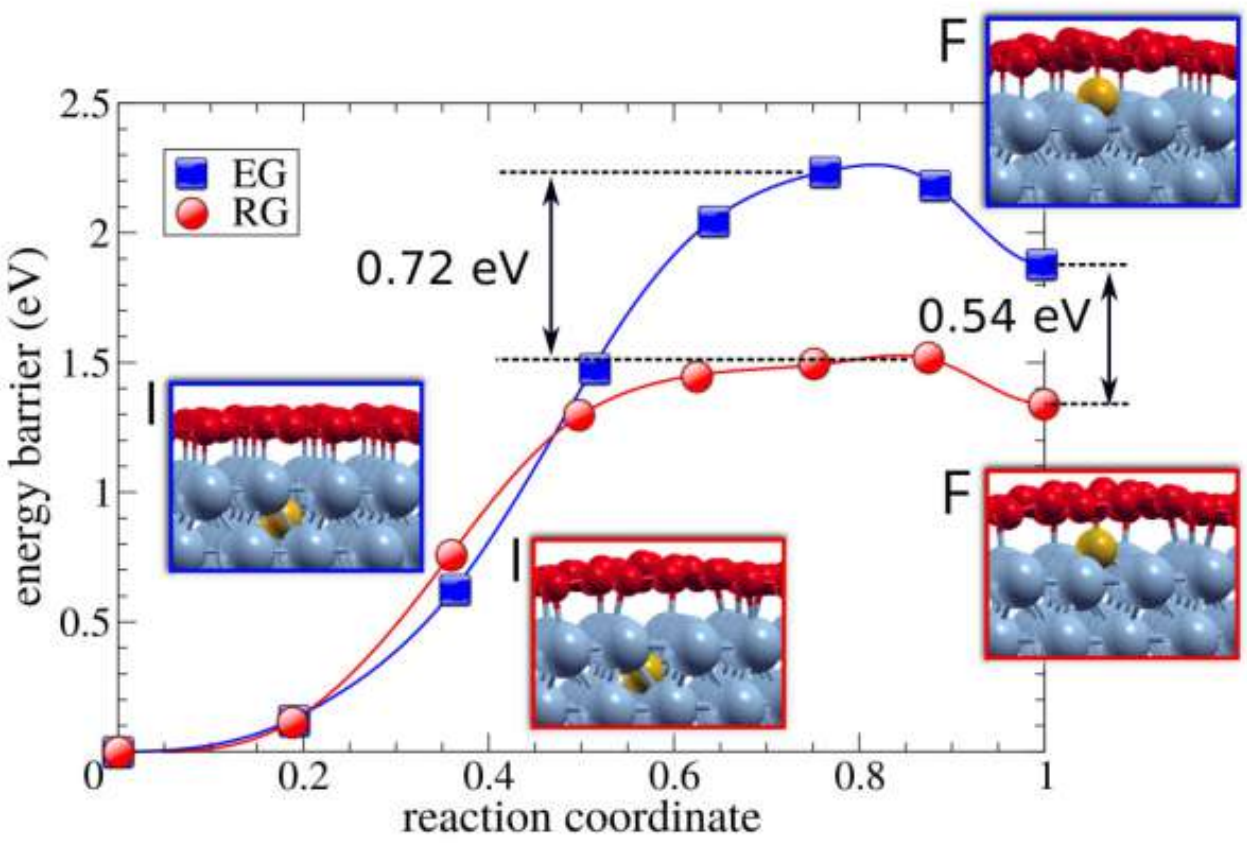

Figure 2.25: Energy barriers for segregation of C atom from *oh* to *fcc* site under EG(blu) and RG(red). Image taken from [88].

of Ni atoms from the first layer from their initial positions in EG and RG (figure 2.26). Finally, as a measure of the energy gain upon carbon addition, we calculated the incremental binding energy ΔE_{bind} for every additional subsurface C atom put in G/Ni(111) interface, as shown in figure 2.26. At low concentration not exceeding 0.3ML , ΔE_{bind} and $\langle d \rangle$ have the same behavior in both EG and RG, indicating that both structures can sustains carbon addition.
At higher coverage the situation abruptly changes: in EG ΔE_{bind} decreases, suggesting that further addition of C atom is unfavorable, while in RG increases, indicating an extra energy gain for additional subsurface C atom. This is confirmed by the steeper increase of the mean displacement of surface Ni atoms under RG than in EG (figure 2.26). Consequently, it is much easier to displace surface Ni atoms under RG rather than EG and in the latter case the Nickel fcc(111) structure is still preserved even at high C concentration.

To summarize, the epitaxially grown G completely locks the nickel surface, making progressively more difficult the C enrichment of Ni outermost layers, hindering the surface reconstruction and thus preventing the nickel carbide formation. When G cover is rotated with respect to Ni(111) surface, the C binding picture changes, the density of subsurface carbon can increase, reaching the critical concentration (estimated around 0.35 ML) which enables the structural transition of the C-enriched Ni(111) layer to a Ni_2C monolayer.

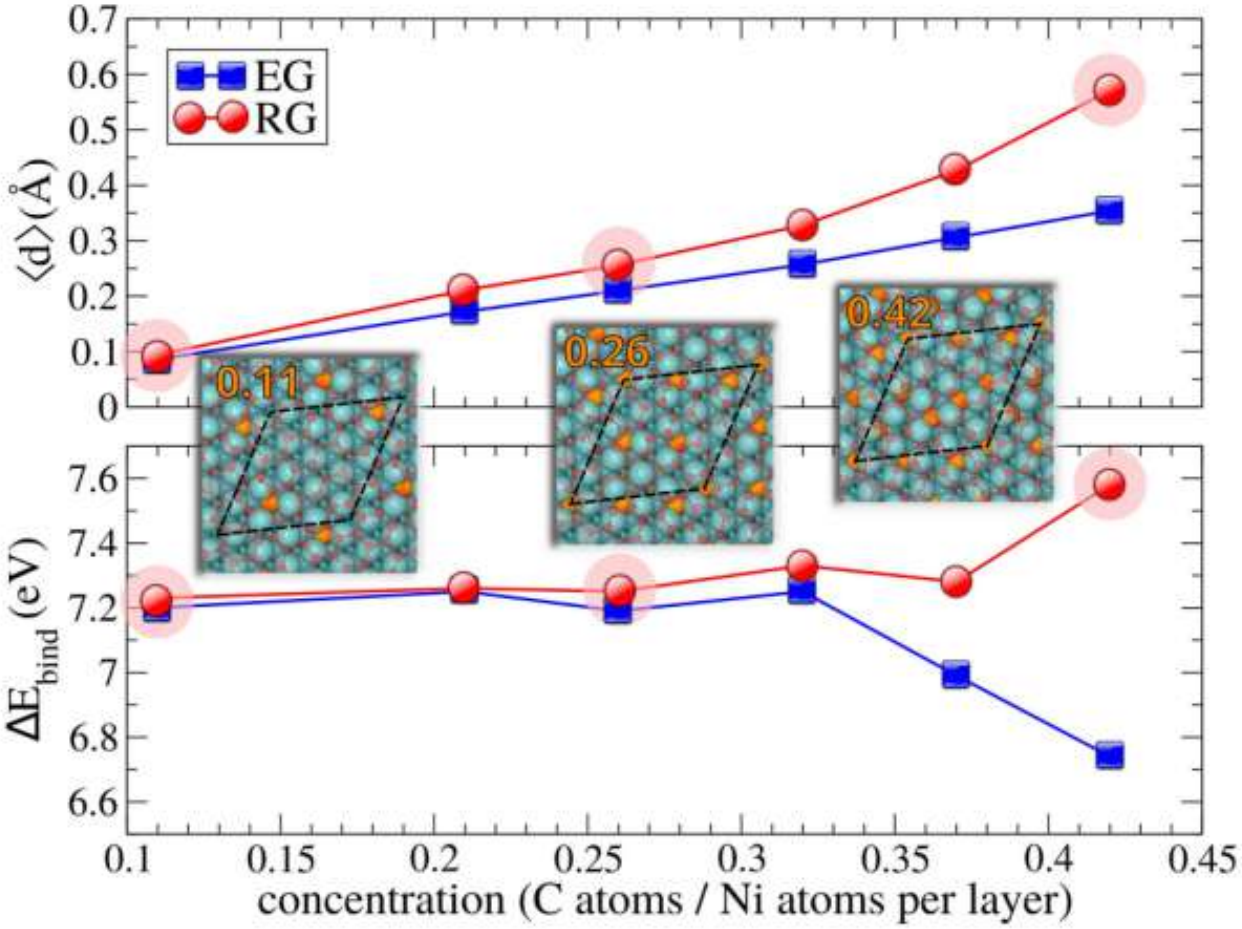

Figure 2.26: Mean absolute displacement $\langle d \rangle$ of surface Ni atoms(top) and the incremental binding energy ΔE_{bind} for the addition of subsurface C atoms to *oh* sites (bottom) in EG (blue) and RG(red) at various concentrations. Image taken from [88].

2.4 G/CO/Ni(111)

The adsorption of Carbon Monoxide on bare metal surfaces has been widely studied by means of different experimental techniques [94] [95] [96] [97] [114] [99] and numerical simulations [100]. On Ni(111) four different high symmetry adsorption sites are available, namely top, bridge, hollow hcp and hollow fcc. At low coverages, when the lateral intermolecular interactions are negligible, the adsorption on hollow sites is favored [99] [114]. At a coverage of 0.5 ML the hollow sites are still indicated as the preferred ones by most of the literature [94] [95] [96] [97] , but alternative suggestions for bridge sites only [101] or a mixture of bridge and top sites are also present [102] [101]. At the saturation coverage of 0.57 ML top and bridge sites are suggested [103].

Under near-ambient pressure conditions, CO molecules can intercalate underneath an epitaxial graphene monolayer grown on Ni(111), getting trapped into the confined region at the interface. The scenario is quite complicated and a detailed description of the adsorption pattern and of its effects on the G electronic structure is still lacking. In order to shed a light into this issue, STM (Scanning Tunneling Microscopy), LEED (Low Energy Electron Diffraction) and XPS (X-ray Photoemission Spectroscopy) experiments were performed by C. Africh, G. Comelli and collaborators at CNR-IOM Tasc. LEED (figure 2.27b) shows new additional spots, beside those related to Ni and G, which are compatible with the co-existence of $c(4 \times 2)$ and $\sqrt{7} \times \sqrt{7}R19.1^\circ$ CO domains, with a local coverage of 0.50 ML and 0.57 ML respectively, in line with results present in literature obtained in absence of G capping. On the other hand, STM images (figure 2.27a) taken after CO dosing show the full hexagon characteristic of decoupled flakes of graphene.

Since STM and LEED provide information about the periodicity of the intercalated CO pattern but no indication about the specific ad-

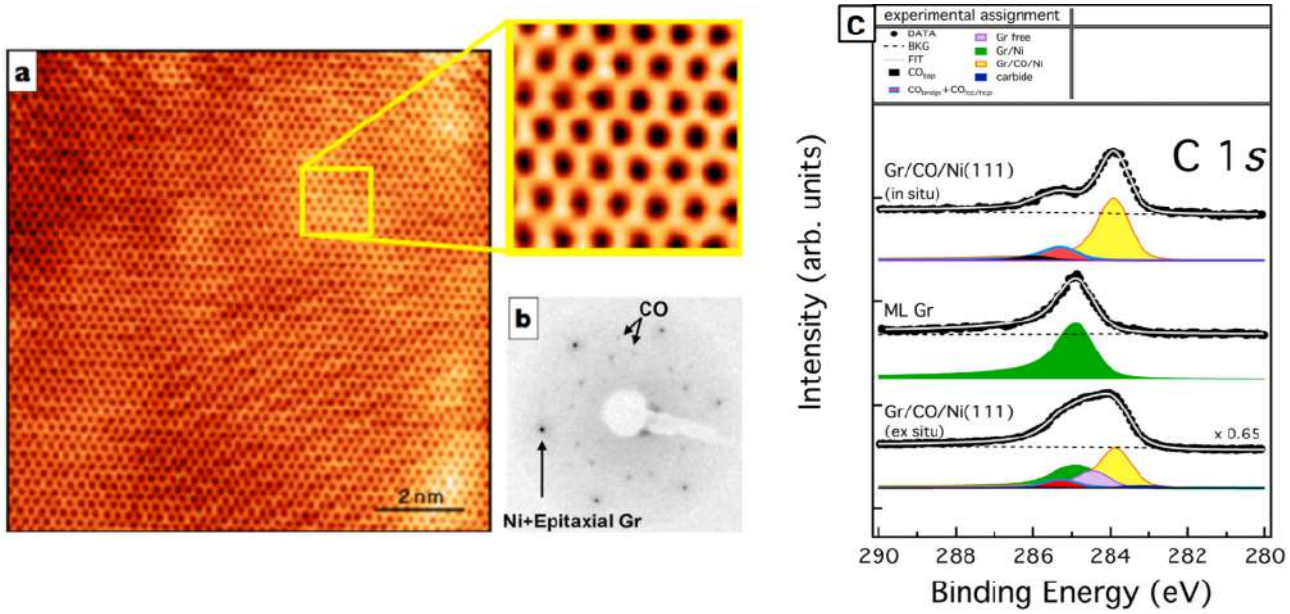

Figure 2.27: Experimental STM image(a), LEED pattern at 100 eV (b) and XPS spectra(c) of graphene/Ni(111) after CO intercalation (10 min @ 10 Torr) [I = 1 nA, V_{bias} = 0.2 V; inset: 1.5 ×1.5 nm^2 , I=1 nA, V_{bias} = 0.4 V]. Image taken from [104]. Legend of experimental peak assignment is reported on the top left.

sorption sites, XPS C1s spectra were taken (figure 2.27c). The signal has been deconvolved with Doniach-Sunjic lineshapes using four components for G on Ni(111), already identified in previous work [**?**], and two further components related to the presence of intercalated CO. The two components, with the hints from DFT calculations, have been attributed to C atoms of CO in top positions and C atoms of CO in bridge and fcc/hpc positions (because of the limited energy resolution, peaks corresponding to CO in bridge and fcc/hcp position, which are expected to lie very close to each other, were merged into a single peak).

In this chapter a full investigation of the intercalated CO pattern for different coverage is provided, highlighting the modifications induced on the graphene electronic structure. The results presented here have already been published [104].

Computational details

DFT calculations were performed with the Quantum ESPRESSO code [27], using the Generalized Gradient Approximation for the exchange-correlation functional in the Perdew-Burke-Ernzerhof parametrization (GGA-PBE) [33]. Ultrasoft, scalar-relativistic pseudopotentials with non-linear core corrections from the QE website have been used [90]. Semi-empirical corrections accounting for the van der Waals interactions were included with the DFT-D2 approach [89]. The periodic cells have different shapes and sizes in the plane to cope with the different CO coverages and accommodate different ordered patterns both for adsorption on clean Ni, in the absence of G capping, and for intercalation at the G/Ni interface. Specifically, we use a rhombic $\sqrt{7} \times \sqrt{7}R19.1°$ cell for 0.14 ML and 0.57 ML, a rectangular $2 \times \sqrt{3}$ and a parallelogrammatic $c(4 \times 2)$ cell for 0.50 ML. In all the supercells 3 Ni layers and G adsorbed on one side with a vacuum spacing of about 24 Å between G and the parallel consecutive Ni(111) surface have been used. Concerning the Brillouin zone sampling, Monkhorst-Pack k-point meshes [38] with similar density for the different cells have been used, namely: $6 \times 6 \times 1$ for the $\sqrt{7} \times \sqrt{7}R19.1°$ cell, $9 \times 9 \times 1$ for the $c(4 \times 2)$ cell and $6 \times 6 \times 1$ for the $2 \times \sqrt{3}$ cell for the structural optimization and self-consistent calculations; $48 \times 48 \times 1$ and $72 \times 72 \times 1$ for the $\sqrt{7} \times \sqrt{7}R19.1°$ cell and for the $c(4 \times 2)$ cell, respectively, for the non-self-consistent calculations for the projected density of states (PDOS). Convergence tests suggested a kinetic energy cutoff of 30 Ry for the plane-wave basis set, 200 Ry for the charge density and an energy broadening of 0.01 Ry for the Methfessel-Paxton smearing technique. For calculation of core-level-shifts the plane-wave energy cutoff was increased to 50 Ry for the wavefunctions and 350 Ry for the charge density. STM simulations were performed using the Tersoff-Hamann approach [46].

DFT simulations

We performed a systematic density functional theory investigation of G/CO/Ni(111) for CO concentrations of 0.14ML, 0.50ML and 0.57ML. For the sake of comparison and validation of our results, it is useful to shortly examine first the CO adsorption patterns on Ni(111) in absence of G capping and for the same coverages, although already studied in literature.

CO/Ni(111)

All the optimized structures are characterized by CO molecules almost perpendicular to the surface, with the C end down (figures 2.28, 2.29, 2.30). For each configuration, adsorption energy has been calculated as:

$$E_{adsCO} = \frac{1}{N_{CO}} \left(E_{CO/Ni} - E_{Ni} - N_{CO} * E_{CO} \right) \tag{2.4}$$

where $E_{CO/Ni}$ is the total energy of the CO/Ni(111), E_{Ni} is the energy of the corresponding clean Ni slab, E_{CO} is the energy of a gas-phase CO molecule and N_{CO} is the number of CO molecules adsorbed on the slab.

At a coverage of $\theta = 0.14ML$(figure 2.28), fcc and hcp sites are favored but also bridge and, to a lesser extent, top sites are stable, with adsorption energies per CO molecule ranging from -2.24 eV (hollow hcp) to -1.86 eV (top)(tab.2.8). At medium coverage of $\theta = 0.50ML$, CO molecules can be arranged in both $2 \times \sqrt{3}$ and $c(4 \times 2)$ patterns (figures 2.29a and 2.29b respectively). The former pattern is the most stable and involves CO molecules alternatively in hollow fcc and hcp sites with an average adsorption energy of -2.26 eV per molecule. The $c(4 \times 2)$ cell involves instead top sites and "hybrid" sites, which are intermediate between fcc and bridge, and between hcp and bridge, with an average adsorption energy of -1.98 eV, lower than in configuration A, as expected since the top site is the least favored.

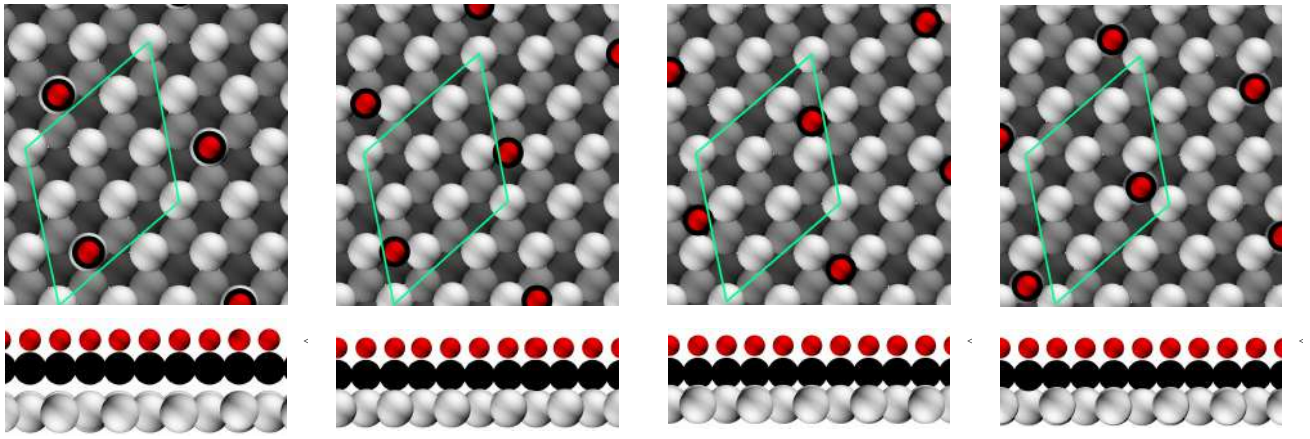

(a) (b) (c) (d)

Figure 2.28: Stable adsorption patterns of CO on Ni(111) (top(a), bridge(b), fcc(c), hcp(d)) in absence of G layer for a CO coverage of 0.14ML. Green lines denote the cell used for simulations. Image taken from [104].

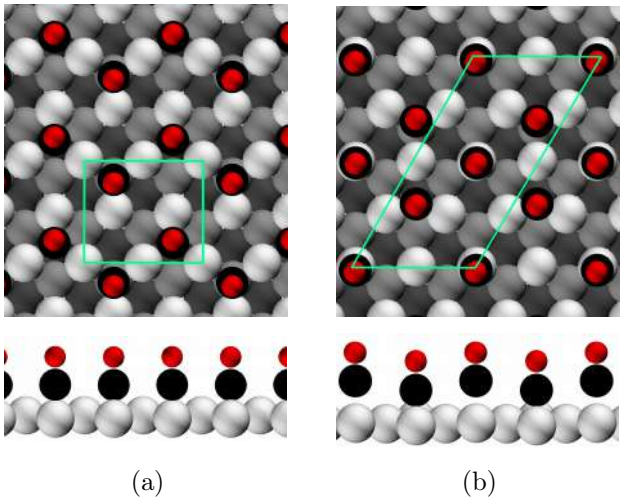

(a) (b)

Figure 2.29: Two different stable adsorption patterns of CO on Ni(111) (1fcc+1hcp(a), 1hcp+1fcc+2top(b)) in absence of G layer for a CO coverage of 0.50ML. Green lines denote the simulations cells used. Image taken from [104].

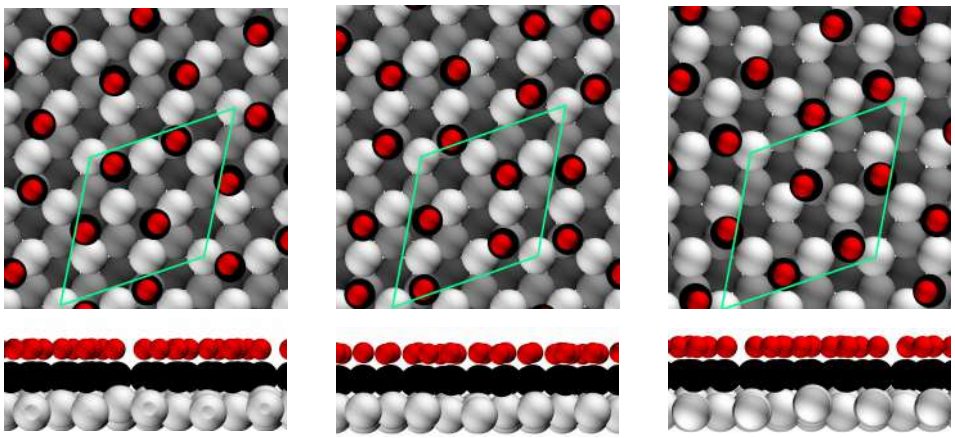

(a) (b) (c)

Figure 2.30: Three different stable adsorption patterns of CO on Ni(111) (1hcp + 3fcc(a), 2hcp+2fcc(b), 3hcp + 1fcc(c)) in absence of G layer for a CO coverage of 0.57ML. Green lines denote the cell used for simulations. Image taken from [104].

For 0.57 ML coverage, three different stable configurations (figure 2.30) have been found, all involving CO molecules mainly in hollow sites (both fcc and hcp), but slightly displaced from high symmetry positions towards top and bridge sites. The average adsorption energy is very similar, between -2.15 eV and -2.16 eV. Two of these configurations are similar to those proposed in Ref. [105]. To summarize, we find a variation of about 0.4 eV, at most, for the average CO adsorption energy within the explored coverage range; larger differences are related to the occupation of less favored adsorption sites rather than to repulsive intermolecular interaction. Our results are in agreement with the literature, taking into account the different details of the calculations.

$\theta(ML)$		$E_{interc\ CO}$ with vdW	E_{adsCO} no G, with vdW	E_{adsCO} no G, no vdW
0.14	top	0.15*	-1.86	-1.56
	bridge	-0.15*	-2.08	-1.80
	fcc	-0.30	-2.22	-1.91
	hcp	-0.34	-2.24	-1.93
0.50	1hcp + 1 fcc	-1.78	-2.26	-1.90
	1hcp + 1fcc + 2top	–	-1.98	-1.62
0.57	1hcp + 3fcc	-1.76	-2.16	-1.78
	2hcp + 2fcc	-1.75	-2.15	-1.77
	3hcp + 1fcc	-1.78	-2.15	-1.77

Table 2.8: Intercalation energies(equation 2.5) for CO at Gr/Ni(111) interface and adsorption energies(equation 2.4) for CO on clean Ni(111) in eV.
*calculated by constraining the in-plane positions of CO since they are not stable adsorption sites.

G/CO/Ni(111)

In the study of CO intercalated at the G/Ni(111) interface, we consider G initially aligned in the top-fcc registry with respect to the underlying Ni(111) surface, and allow the structures to fully relax. In all cases, even for the smallest coverage of $0.14ML$, the G layer is well detached from Ni surface, increasing its original distance (2.12 Å without CO) to 5.52 Å, while maintaining the top-fcc registry. In the optimized structures, the CO molecules are almost perpendicular to the surface, as in the absence of G capping. At low coverage ($\theta = 0.14ML$), only hollow (fcc, hcp) sites are stable for CO adsorption (figure 2.31). For comparison, the intercalation energy for top and bridge sites has been calculated by constraining the in-plane position of CO. G capping clearly puts a constraint for the adsorbed CO pattern also at higher coverage: at $0.50ML$, only one pattern is found, with the CO occupation of fcc and hcp sites(figure 2.32). Conversely, three different adsorption patterns are found at

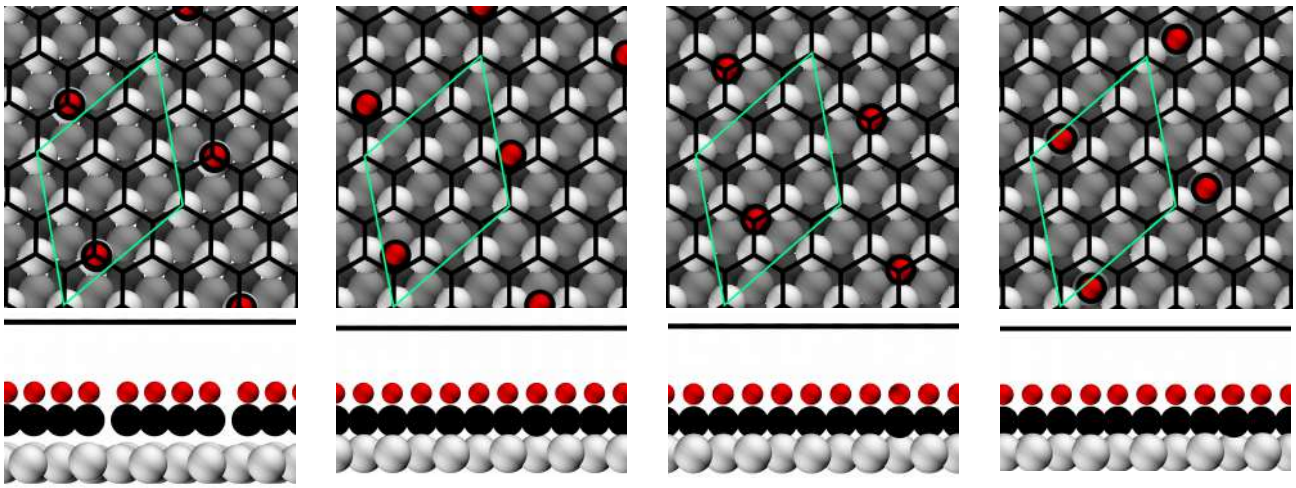

(a) (b) (c) (d)

Figure 2.31: Adsorption configurations of CO on Ni(111) (top(a), bridge(b), fcc(c), hcp(d)) in presence of G layer for a CO coverage of 0.14ML. Fcc and hcp sites are stable while top and bridge have been obtained by constraining the in-plane positions of CO molecules. Green lines denote the cell used for simulations. Image taken from [104].

$0.57ML$, characterized mostly by the occupancy of hollow sites with CO molecules slightly displaced towards top and bridge sites, similarly to the case without G capping (figure 2.33). In summary, for CO intercalated at G/Ni(111), we did not find stable configurations including top sites, at variance with what we found in the absence of G capping for 0.14 ML and 0.50 ML. The CO intercalated mainly occupies hollow sites, even if slightly moved towards bridge or top sites, and G cover inhibits the occupation of pure top sites, as suggested in [106].

Energetics

Insight about mutual interaction between G, CO molecules and Ni substrate can be inferred from the energetics. In particular, we can gain information about the stability of the system from the binding energy of intercalated CO at G/Ni interface per CO molecule, defined as:

$$E_{intercCO} = \frac{1}{N_{CO}} \left(E_{G/CO/Ni} - E_{G/Ni} - N_{CO} * E_{CO} \right) \qquad (2.5)$$

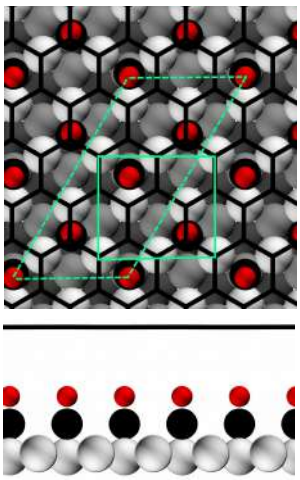

(a)

Figure 2.32: (a) Stable Adsorption configuration of CO on Ni(111) (CO on fcc and hcp sites)in presence of G layer for a CO coverage of 0.50ML. Green lines denote the cell used for simulations. Image taken from [104].

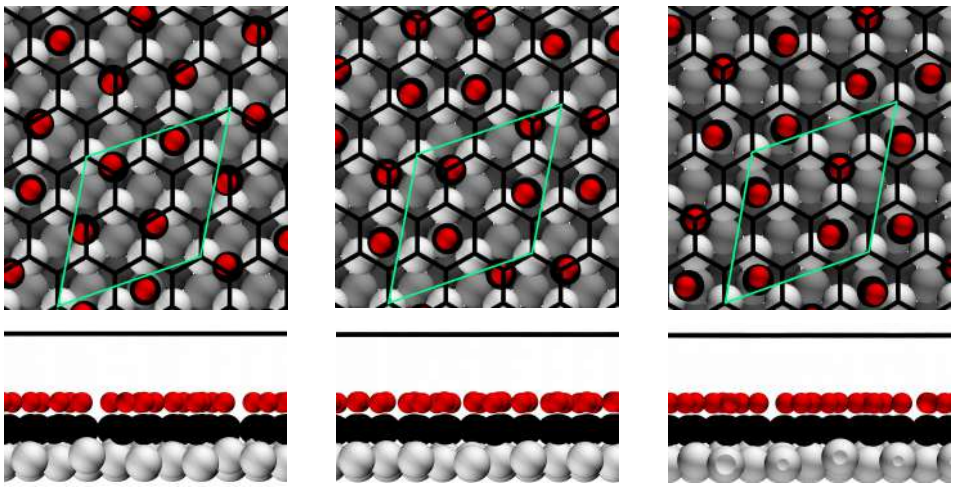

(a) (b) (c)

Figure 2.33: Stable adsorption configurations of CO on Ni(111) ((a)1hcp+3fcc, (b)2hcp+2fcc, (c)3hcp+1fcc) in presence of G layer for a CO coverage of 0.57ML. Green lines denote the cell used for simulations. Image taken from [104].

where $E_{G/CO/Ni}$ is the total energy of the G/CO/Ni(111), $E_{G/Ni}$ is the energy of the corresponding system in absence of CO, E_{CO} is the energy of a gas-phase CO molecule and N_{CO} is the number of intercalated CO molecules. From table 2.8, $E_{intercCO}$ can be compared with the corresponding energy quantity without G capping, E_{adsCO}: as coverage increases, $E_{intercCO}$ decreases, while E_{adsCO} remains more or less constant. The large variation between low and high coverage can be attributed to the different balance between the energy necessary to detach G from Ni, which is always the same per C atom, and the energy gained when CO intercalates and binds to the Ni surface, which depends on the coverage [107] .
The interaction between G and the substrate can be evaluated through adhesion energy defined as:

$$E_{adhG/(CO/Ni)} = \frac{1}{N_G}\left(E_{G/CO/Ni} - E_{CO/Ni} - E_G\right) \tag{2.6}$$

in the case with intercalated CO, and defined as:

$$E_{adhG/Ni} = \frac{1}{N_G}\left(E_{G/Ni} - E_{Ni} - E_G\right) \tag{2.7}$$

without CO, where $E_{CO/Ni}$ is the energy of the corresponding system without G capping, $E_{G/Ni}$ is energy of the system without CO, E_G is the energy of free-standing G layer, E_{Ni} is the energy of the Ni(111) slab alone and N_G is the number of C atoms of G. We found $E_{adhG/(CO/Ni)} = -0.05$ eV and $E_{adhG/Ni} = -0.16$ eV for each configuration studied, indicating that G is less bound to CO/Ni than to the clean Ni surface. In summary, these energy values suggest that the CO intercalation facilitates the detachment of G from Ni.

2.4.1 Electronic properties

Core-level shits

Core-level-shifts(CLSs) of C 1s level have been calculated for all the configurations considered here (both for C atoms in G and in the

intercalated CO molecules), comparing them with the binding energy(BE) of free-standing G. Interestingly, for G directly supported on Ni(111) we obtained an average CLS of about 0.4 eV towards higher BE, with the CLS of C 1s in top and fcc sites differing by about 0.1 eV, well beyond the numerical accuracy.
The effect of the CO intercalation on the C 1s of G is strongly dependent on coverage: small for $\theta = 0.14ML$ but large for $\theta = 0.50ML$ (with a CLS of about 0.55 eV towards lower BE) and $\theta = 0.57ML$ (CLS of 0.35 eV), notwithstanding the extremely weak interaction between G and CO (table 2.9). The non-monotonic behavior of the C1s peak could be due to the different periodic cells used to model different CO coverage.

C1s	Exp(eV) [104]	DFT(eV)	
		GR/CO/Ni(111)	CO/Ni(111)
G decoupled by CO	283.8	284.35[0.14ML] 283.85[0.50ML] 284.05[0.57ML]	-
G non interacting	284.4	284.40	-
Gr/Ni	284.8	284.80 [fcc] 284.90 [top]	-
CO bridge	285.3	285.15 [0.14ML]	285.15
CO hollow		284.95[0.14ML] 284.95[0.50ML] 284.95[0.57ML]	284.95[0.14ML] 284.95[0.50ML] 284.95[0.57ML]
CO top	285.9	285.70 [0.14ML]	285.70
carbide	283.2[283.0-.5]	283.20 283.60	-

Table 2.9: Experimental and DFT calculated C1s XPS peaks. Experimental values are taken from [104]. The calculated values have been aligned with experimental peaks for the non-interacting (free standing) G.

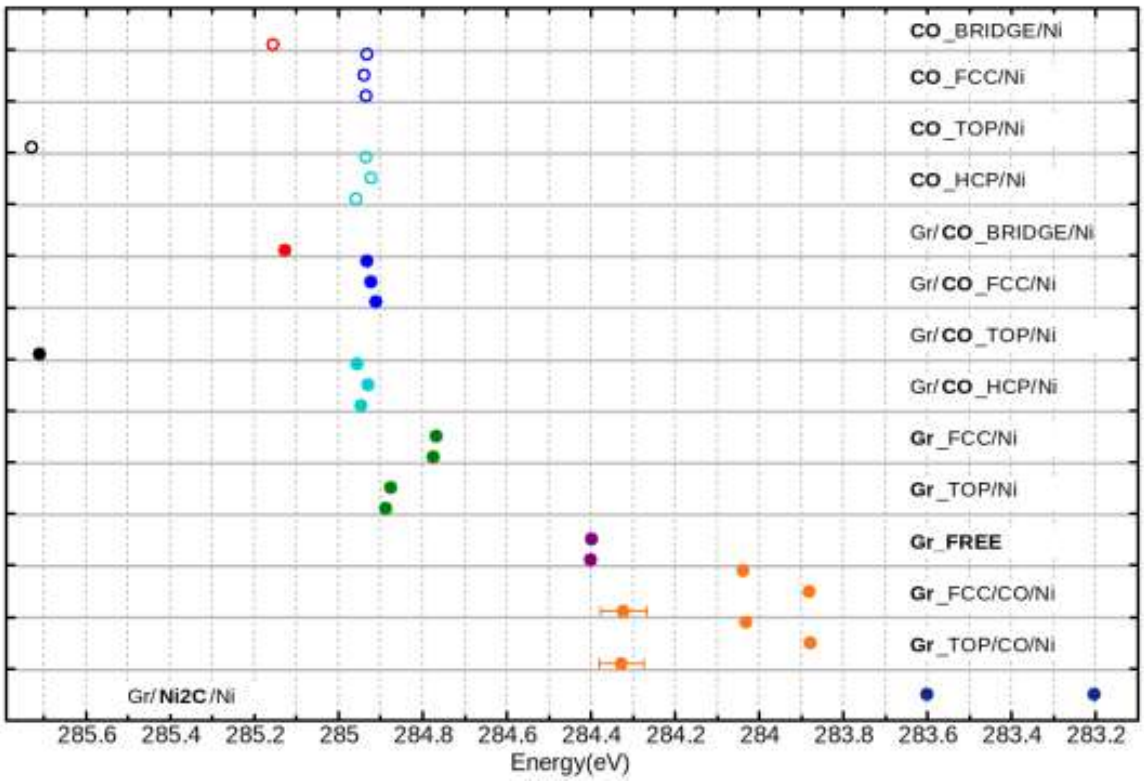

Figure 2.34: Details of DFT calculated C 1s core level binding energies (horizontal axis) for C atoms in CO/Ni, Gr/Ni, Gr/CO/Ni, Gr/Ni 2 C/Ni. The results are separated in different panels: each panel refers to a specific system and a specific C type, indicated in the label (bold fonts are used to unambiguously distinguish which C type we refer to). The same color code of figure 2.35 (XPS spectrum) is used: purple for C atoms of free standing Gr; orange for C atoms of G decoupled by Ni after CO intercalation; green for C atoms of G directly interacting with Ni; light blue for C atoms of CO at (or close to) fcc or hcp sites; red for C atoms of CO at bridge sites; black for C atoms of CO at top sites, dark blue for C atoms of a carbide layer between G and Ni. Filled/open symbols for C atoms of CO indicate configurations with/without G capping, respectively. For the C atoms of G we show separately the results for the two sublattices, having top and fcc registry with respect to the Ni(111) surface. In each panel we distinguish results obtained in different simulation cells, distributing them on the vertical axis for visualization purposes. In particular, from bottom to top within each panel: i) for systems including CO we report the results for coverage of 0.14 ML, 0.50 ML, 0.57 ML, respectively; ii) for free G and Gr/Ni we report the results obtained in the $\sqrt{7} \times \sqrt{7}R19.1^\circ$ cell and in a cell multiple of the $2 \times \sqrt{3}$, respectively (this choice guarantees that a core-excited C atom is well separated from its images in the adjacent periodically repeated cells); The error bar on the C 1s peak position of G in Gr/CO(θ=0.14ML)/Ni (orange) indicates the variation with the particular choice of the C atom of Gr. In all the other cases the variations are negligible. Image taken from [104].

As mentioned above, through DFT calculations, we have also access to the CLSs of the C atoms belonging to the intercalated CO molecules. In all cases, those C 1s levels are shifted toward higher BE with respect to what computed for free standing G, with CLSs comparable or even larger than those obtained for G directly interacting with Ni.
As reported in table 2.9 and figure 2.34, CO molecules forced in high symmetry top and bridge sites at $\theta = 0.14ML$ show the largest C 1s CLSs, namely 1.3 eV in top and 0.75 eV in bridge site with respect to free standing Gr. In all the other cases, and for the entire range of investigated coverages, when the CO molecules are precisely in highly symmetric hollow sites (for 0.14 ML) or slightly displaced towards "hybrid" hollow-bridge positions (for 0.50 and 0.57 ML), the CLSs are almost identical and displaced by about 0.55 eV with respect to free standing G, i.e. only about 0.1 eV larger than G directly interacting with Ni. Moreover, CLS for CO molecules adsorbed on clean Ni surface are the same as with G capping, so in general the presence of G does not affect the CO C 1s binding energies. Figure 2.35 reports the calculated CLSs together with experimental spectra. Since the ex situ spectrum was acquired from a region mainly occupied by the 0.50 ML CO structure, with few coexisting 0.57 ML domains, we used the values calculated for 0.50 ML, although those for 0.57 ML are very similar (tab. 2.9). Since theoretical calculated CLSs were defined up to a constant, all CLSs have been shifted by the same amount in order to align experimental and theoretical CLS of free-standing G (violet peak and bars in figure 2.35 , respectively). We can observe a good agreement between the theoretical values and the attribution of the experimental peaks concerning the C 1s level of G in the different configurations considered (G directly interacting with Ni and detached from Ni by CO intercalation, indicated respectively with green and orange bars). Moving to the high BE region, the XPS broad component at 285.3 eV (red/blue component in figure

2.35) well matches the calculated values for CO in hollow - both fcc and hcp - and bridge sites (light blue and red bars, respectively). At even higher binding energies, the top site CO peak, predicted to be present at 285.7 eV on the clean Ni surface and absent under the G capping at high CO coverage, is almost negligible (black component at 285.9 eV), with a small residual intensity likely due to defect sites. C 1s peaks of carbide are also included in the convolution and their positions are compatible with what we found in the previous chapter.

Electronic structure analysis

Band structures projected on the G layer for G/Ni(111) and for the three G/CO/Ni(111) systems have been calculated and are reported in figure 2.36. The band structure has been evaluated along the $\Gamma \rightarrow M \rightarrow K \rightarrow \Gamma$ high-symmetry path for the $\left(\sqrt{7} \times \sqrt{7}\right) R19.1°$ cell and along the $\Gamma \rightarrow X \rightarrow S \rightarrow Y \rightarrow \Gamma$ high-symmetry path for the $\left(2 \times \sqrt{3}\right)$ cell. In all three cases we can observe a clear shift of the Dirac cone above the Fermi level, suggesting a net p-type doping effect that increases with the increasing coverage. We recall that G/Ni(111) is a n-type system, as clearly visible from figure 2.36a, where, notwithstanding the strong hybridization with the d Ni states, a main feature resembling a linear dispersion crossing can be recognized at about 4 eV below the Fermi level for the spin up C states and at about 3.3 eV for the spin down C states, in reasonable agreement with the feature experimentally detected at 2.66 eV [87]. Therefore, the presence of intercalated CO molecules has a strong and opposite effect on the G doping. The doping effect has been further investigated by analyzing the density of states (DOS) projected on the C atoms of the G layer for the three different coverages (figure 2.37a). The zero of the energy scale is set to the Fermi energy of the free standing case. The plot in figure 2.37a clearly shows that the DOS of G, detached from the substrate by intercalated CO, recovers its free-standing typical shape, but with a rigid shift towards higher

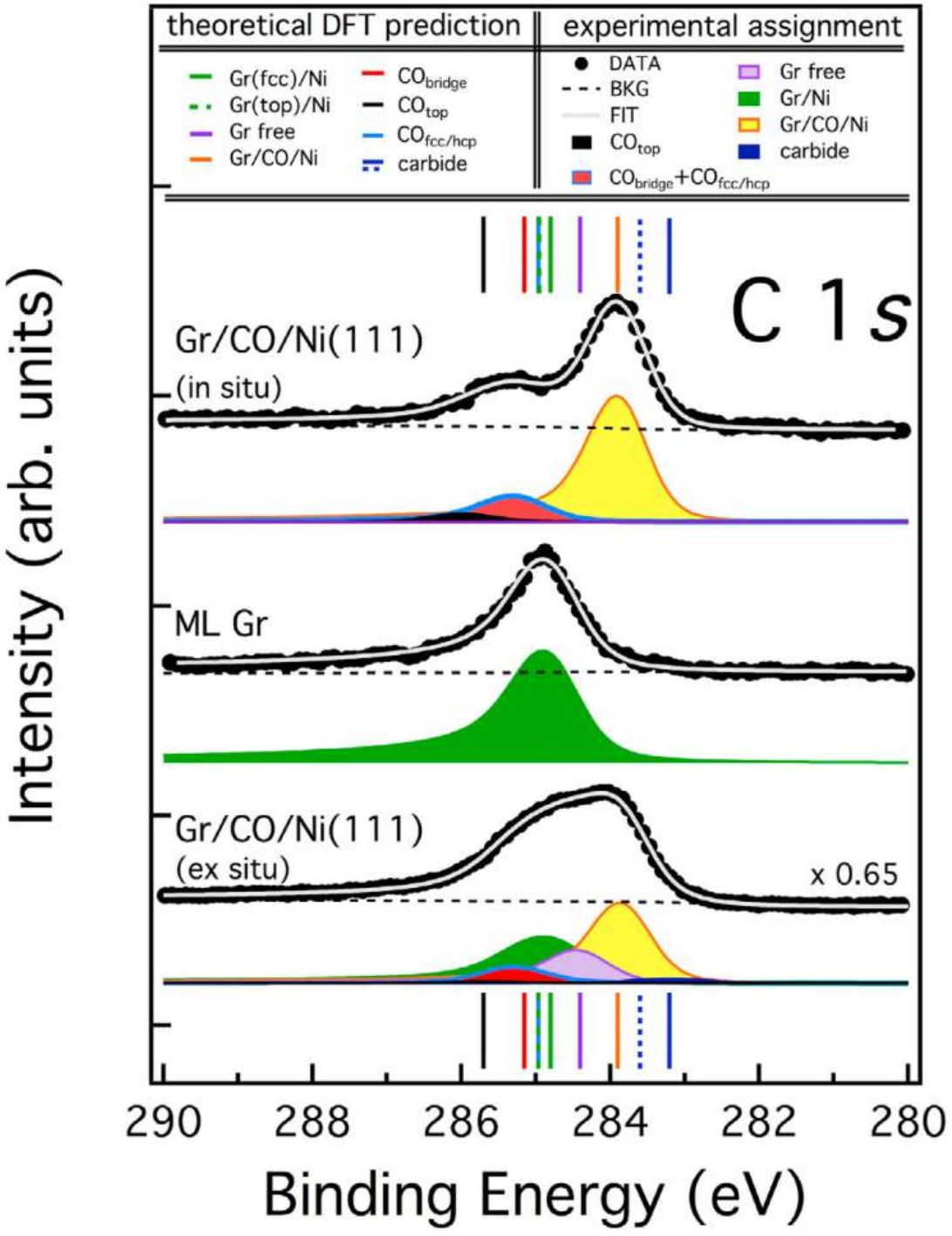

(a)

Figure 2.35: Comparison of the experimental XPS spectrum and the calculated binding energies of C 1s core level for Gr/CO/Ni (bottom panel: ex situ; upper panel: in situ) and for epitaxial Gr/Ni (middle panel). The experimental spectrum of Gr/CO/Ni detected ex situ has been deconvoluted with six components. Only three of them contribute to the intercalated layer prepared in situ. The DFT calculated values correspond to the configuration with 0.50 ML of CO (which is the coverage characterizing the experimental sample), except for the values for CO in bridge and in top positions which are shown as a reference and are calculated in an artificial configuration at 0.14 ML with constraints on the in-plane position of CO. See table 2.9 and figure 2.34 for details. Image taken from [104].

energies, in perfect agreement with the projected band structures shown in figure 2.36. The result, irrespective of the particular CO adsorption sites, is a sizeable p-doping effect, monotonically and linearly increasing with the CO coverage up to 0.86 eV at the saturation value (figure 2.37b).

Electronic charge transfer analysis

Similarly to what done for the energy, we can split the electron density into different contributions and then plot their difference with respect to the electron distribution of the whole system G/CO/Ni. Figure 2.38 shows the contour plots of the differential electron density calculated in two different ways:

$$\Delta n_1(\mathbf{r}) = n_{G/CO/Ni}(\mathbf{r}) - n_G(\mathbf{r}) - n_{CO}(\mathbf{r}) - n_{Ni}(\mathbf{r}) \tag{2.8}$$

and

$$\Delta n_2(\mathbf{r}) = n_{G/CO/Ni}(\mathbf{r}) - n_G(\mathbf{r}) - n_{CO/Ni}(\mathbf{r}) \tag{2.9}$$

The first plot highlights the large polarization of the CO molecules due to the adsorption on Ni. In the second plot, the interaction between G and the intercalated CO is magnified, and a very small electron transfer from G to CO is visible. The latter can be quantified calculating the Löwdin charges [39]: C atoms of G give on average to the intercalated CO 0.004, 0.018 and 0.022 electrons for coverage of 0.14 ML, 0.50 ML and 0.57 ML, respectively, following an almost linear trend. We notice that this electron transfer, although very small, has a direction compatible with the p-doping effect found in the projected DOS analysis.

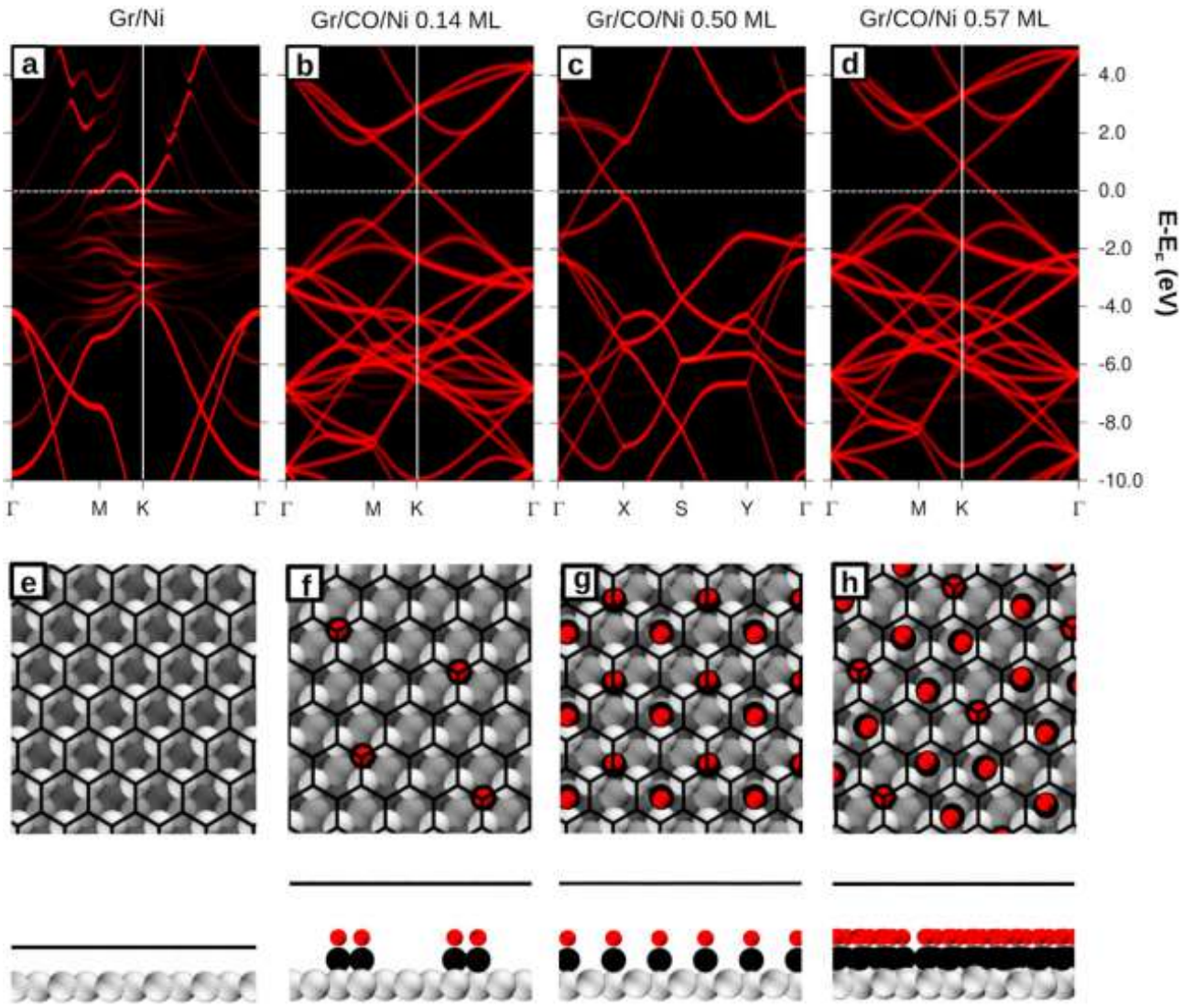

(a)

Figure 2.36: First row(spin-up channel only, for spin-down channel see SI of [104]): Gr-projected band structure along the high symmetry path for (a) Gr/Ni and for Gr/CO/Ni at different CO coverages: (b) 0.14 ML, (c) 0.50 ML, and (d) 0.57 ML. Second row: Top and side views of representative optimized models for (e) Gr/Ni and for Gr/CO/Ni at different CO coverages: (f) 0.14 ML, (g) 0.50 ML, and (h) 0.57 ML; the side views are taken in a bottom-up direction with respect to the top view panels. Oxygen: red; Carbon: black (wireframe for Gr, spheres in CO); Ni: grey, from light to dark according to the depth from the surface. Image taken from [104].

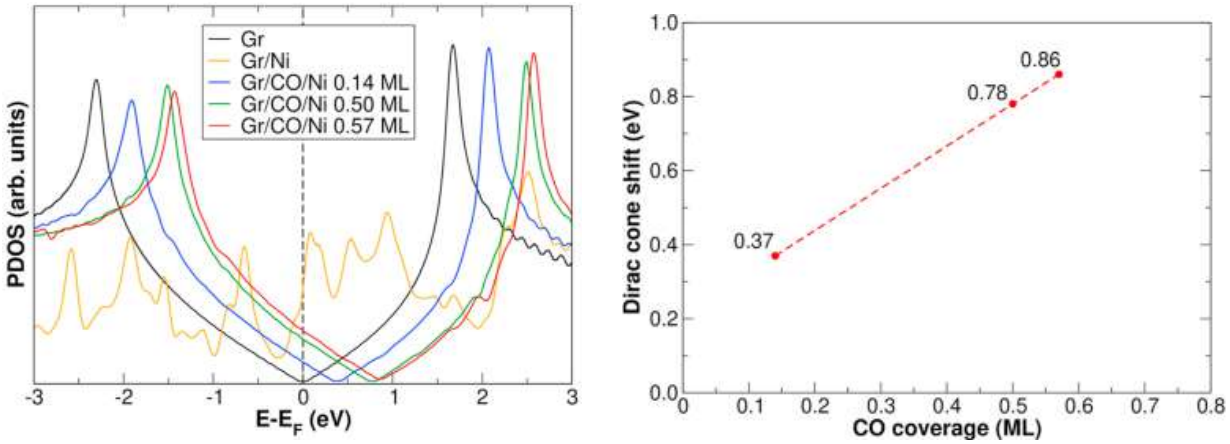

(a) (b)

Figure 2.37: (a)Projected density of states (PDOS) onto the supported-graphene C p_z states for the optimized models of Gr/CO/Ni(111) at different CO coverages (0.14 ML, 0.50 ML, and 0.57 ML). The C p_z PDOS of free-standing graphene and of G on Ni without intercalated CO is shown for comparison. The PDOS value for each system is normalized to one C atom of graphene. All energies are referred to the corresponding Fermi energy of each system, as indicated by a dotted black line. (b) Linear relationship of the shift of the Dirac cone with respect to the Fermi energy for Gr/CO/Ni(111) (in eV) vs the CO coverage. Image taken from [104].

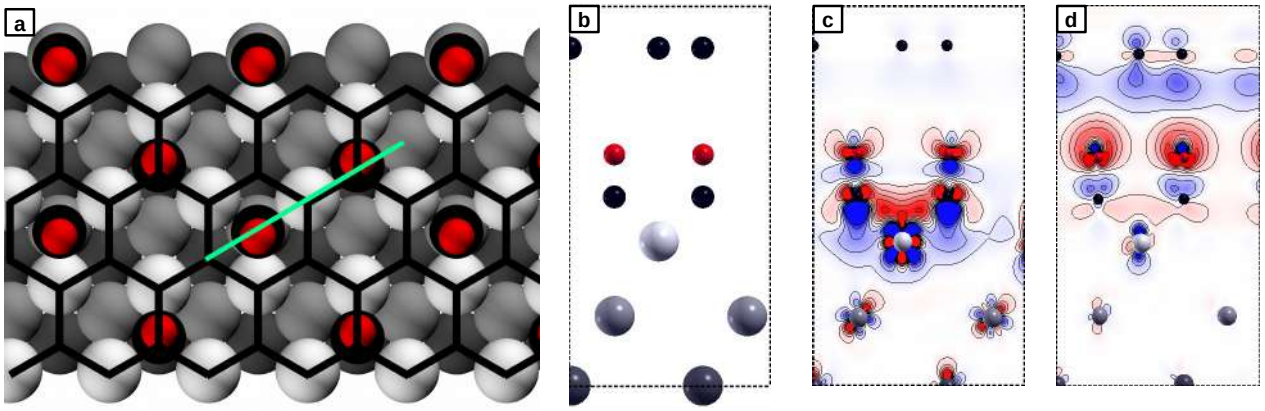

(a)

Figure 2.38: Stick-and-ball model (a,b) and electron density difference plots (c,d) for a stable adsorption configuration for a CO coverage of 0.50 ML. Stick-and-ball model: (a) top view, with the indication of the plane considered for the side view; (b) side view. Plots in the plane (b) for electron density difference calculated as in equation 2.8 (c) and equation 2.9(d). Red/blue indicates abundance/depletion of electrons. The electron density difference isosurfaces are plotted at $+/-0.015\ e/a_0^3$ and at $+/-0.002\ e/a_0^3$ in (c) and (d), respectively. The smallest scale in (d) allows to appreciate the very small electron transfer from G to the intercalated CO. Image taken from [104].

Chapter 3

Graphene on Ni(100)

Graphene(G) can be grown on Nickel facets with different lattice symmetries which leads to different moiré patterns according to the local registry with the substrate: while G on Ni(111) can be grown without substantial tension or corrugation [**?**], on Ni(100) the interfacial symmetry mismatch leads to the formation of stripe or network moiré pattern [108]. Of particular interest for this work is the stripe moiré pattern where regions of chemisorbed G alternates to physisorbed G, resulting in a potential interesting environment for adatom or molecules adsorption. One of the main issues for G growth on Ni(100) is the presence of vacancies in G deposited on a metal substrate, since metal-G interaction reduces the vacancies formation energy and facilitate their formation [109]. Although many efforts have been done so far, a large-scale fabrication of defect-free graphene is still missing [110]. On the other hand, defects in G open new possibilities in surface chemistry as they can be very active and selective in the adsorption of adatoms such as Co or molecules of environmental importance such as Carbon Monoxide [73]. In this chapter we give an overview of different types of C-vacancies in G/Ni(100) and how their presence can affect the reactivity of G towards Co adatoms and CO molecules adsorption.

3.1 Computational detail

Spin-polarized DFT calculations were performed with QUANTUM ESPRESSO (QE) package [27]. Exchange and correlations effects were taken into account by means of Perdew-Burke-Ernzerhof (PBE) parametrization within the Generalized-Gradient-Approximation [33]. Van der Waals interactions were also added by means of semi-empirical corrections DFT-D2 scheme [89]. Cutoffs of $30Ry$ and $200Ry$ were set for plane-wave basis set and electron density expansions, respectively. The convergence threshold for total energy in all calculations was set to $10^{-6}Ry$. Ultrasoft, scalar-relativistic pseudopotentials with non-linear core corrections from the QE website have been used [90]. To model G on Ni(100) stripe moiré pattern we used an orthorhombic supercell with in-plane dimensions set to 12x4 unit cells of Ni(100), where the factor of 12 allows to accommodate six armchair periods (corresponding to 2 valleys and two ridges of the stripe moiré) and the factor of 4 gives the minimum reasonable separation between images of defect along the stripe direction (figure 3.1) [108]. Thickness of vacuum region has been set to 12 Å. A 1×2×1 k-mesh including Γ point has been used for Brillouin zone sampling during structural optimizations. The Methfessell-Paxton smearing with an energy broadening of 0.01 Ry was used [39]. In order to simulate STM images, further *nscf* calculations with a 2×6×2 k-mesh have been done. STM images simulations were performed employing the Tersoff-Hamann scheme [46]. Energy barriers were calculated by means of nudged elastic band method with the quasi-Newton Broyden optimization scheme. In all cases a threshold on the norm of the force orthogonal to the path was set to 0.1 eV/Å.

3.2 Structural model for C-vacancies

Relaxation of atomic positions of pristine G on Ni(100) revealed a periodicity of ripples of 15 Å and a moderate corrugation, with G-Ni distance varying between 1.95 Å (we will refer to this region as *valley*) and 2.8 Å (referred as *ridge*), in agreement with [108](figure 3.1a).

We then considered the possibility to create single (1V) or double

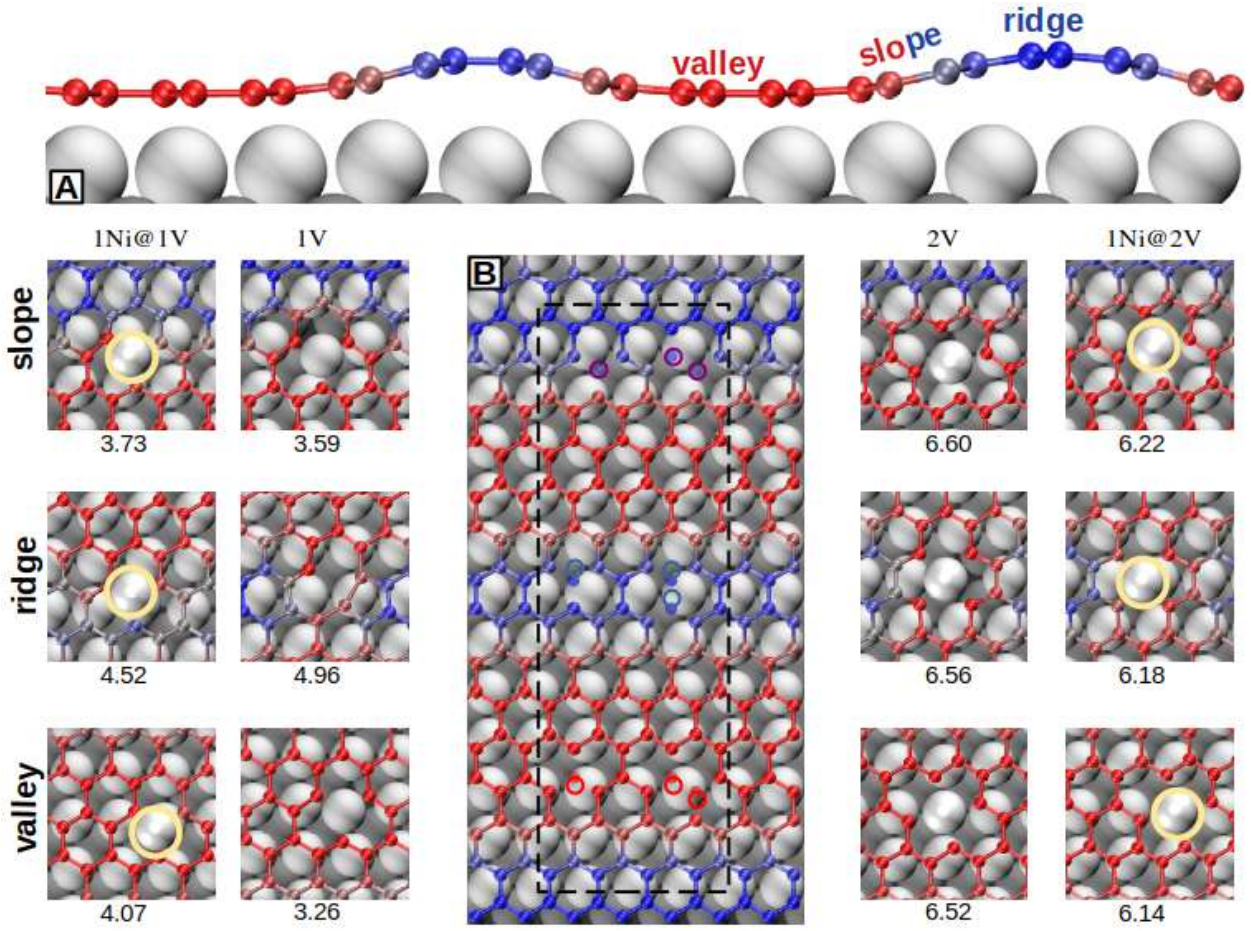

Figure 3.1: (a)Side view of s-moiré pattern for G on Ni(100) where valleys(red) and ridges(blue) alternates. (b) Top view of the s-moiré pattern. Black dashed lines denote the supercell used. Single(1V) and Double(2V) C-vacancy on valley, slope and ridge are depicted as circled transparent spheres. In the insets on the left(right) 1V and 2V passivated by substrate(additional Ni adatom) are reported with their formation energy calculated with equation 3.1(3.2). Additional Ni adatom are circled in yellow.

(2V) C-vacancies in three different regions: on the valley, on the ridge and on the slope between ridge and valley, as shown in figure 3.1. For each configurations the vacancy formation energy has been

calculated as(see table 3.2):

$$E_{form}(nV) = E(G^*/Ni(100)) - E(G/Ni(100)) + nE(G_C) \quad (3.1)$$

where $n = 1(2)$ stands for single(double) vacancy, $E(G^*/Ni(100))$ is the total energy of the structure with one single(double) vacancy, $E(G/Ni(100))$ is the total energy of the vacancy-free structures and $E(G_C)$ is the total energy of pristine G sheet per C atom. A positive E_{form} indicates that a certain amount of energy is needed to create the vacancy(see table 3.2). Defected structures with higher $E_{form}(nV)$ are less probable from a thermodynamic point of view as more energy must be invested for their formation. The surface vacancies are among the most reactive sites in the structure and as such they ought to be passivated either by the substrate or by atoms/molecules that are diffusing on the surface. The formation of 1V on the ridge is very unfavorable since the ridge is very far from the nickel surface and thus the passivation by substrate is hindered. This can be rationalized from a very small displacement of Ni atom below the vacancy of only 0.20 Å and a very high formation energy of 4.96 eV. The other two 1V configurations are slightly more favorable, as $E_{form}(1V)$ is lower for 1V on slope and on valley, but its values of 3.59 eV and 3.26 eV, respectively, are still very high. The lower values of E_{form} with respect to 1V on ridge are due to the partial passivation realized by the Ni atom laying below 1V, which moves upwards by 0.71 and 0.63 Å and binds to the vacancy.
The formation of 2V is still not very favorable even though their E_{form} per missing C-atoms is lower then single vacancies. The gain in formation energy comes from an efficient passivation of 2V, as the Ni atom that is laying below the 2V moves upwards by ~ 1.5 Å and fully passivates the vacancy (figure 3.1). However, such displacement of Ni atom from its site on (100) surface is a process that requires a lot of energy and the net result is a positive formation energy of substrate-passivated 2V.

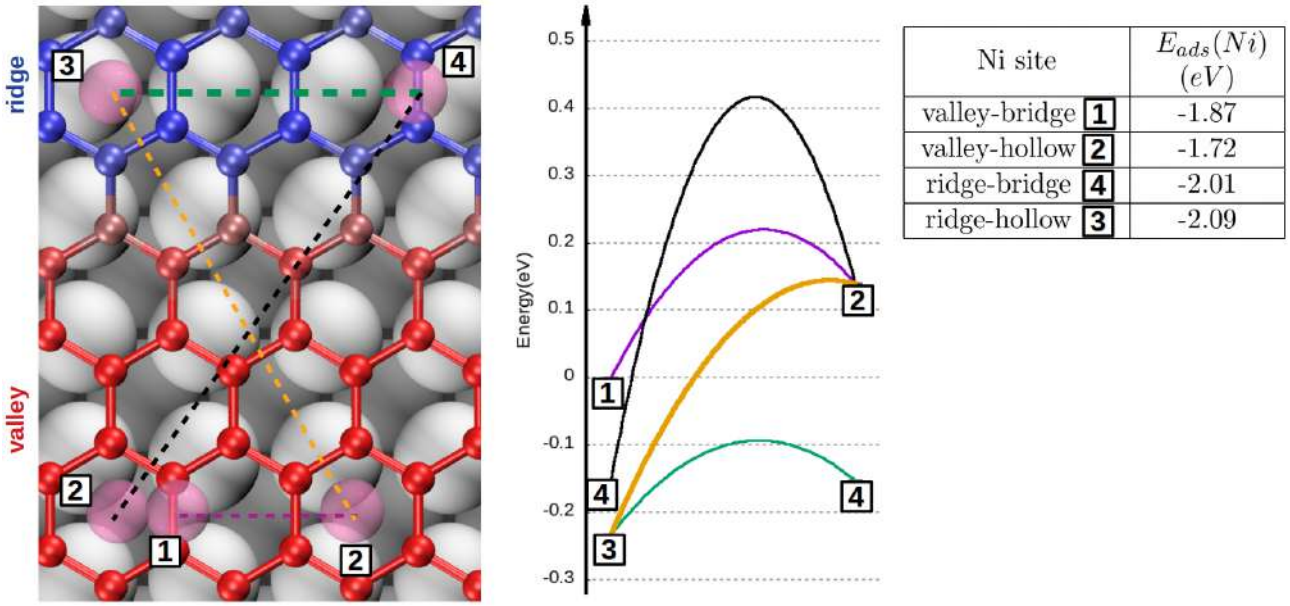

Ni site	$E_{ads}(Ni)$ (eV)
valley-bridge 1	-1.87
valley-hollow 2	-1.72
ridge-bridge 4	-2.01
ridge-hollow 3	-2.09

Figure 3.2: Adsorption energies and diffusion barriers for a Ni adatom on G/Ni(100) without defects. Color scale for s-moiré pattern is the same as in figure 3.1. The values of E_{ads} are reported in the table on top right; in the plot they are rescaled to the value in the site labeled by 1.

Nevertheless, increasing the temperature Ni atoms become more mobile and the concentration of Ni atoms that diffuse along the surface increases. Even though vacancies of free G are very mobile [111] and could easily reconstruct upon the increasing of temperatures, we can disregard it since G on valley is strongly interacting with Nickel underneath and a migration of C atoms would require a huge amount of energy, i.e. a very high temperature. Therefore, if G contains vacancies, they can be passivated not only by substrate but also by diffusing Ni atoms, that could be either at the interface or on G. To inspect this possibility, we performed NEB calculation for Ni diffusion on pristine G on Ni(100) (figure 3.2). Diffusion along the ridge and along the valley has very low energy barriers, easily overcome by thermal excitation. Interestingly, the energy barrier for Ni diffusion from valley to ridge is much lower than viceversa (0.25 eV vs 0.55 eV respectively) so we could expect larger Ni concentration on ridge than on valley as temperature increases.

On the basis of previous investigation of defects in G/Ni(111) [112],

a tentative assignment of the different types of defects has been proposed also for experimental images taken on G/Ni(100).

	ridge	slope	valley	tot.
1V	0.203	0.033	0.004	0.240
2V	0.149	0.005	0.002	0.156
1Ni@2V	0.302	0.196	0.106	0.604
tot	0.654	0.234	0.112	1.000

Table 3.1: Contingency table of relative frequencies distribution for C-vacancies. Frequencies have been obtained by identifying C-vacancies in experimental STM images and classifying them according their position on the moirè pattern (ridge, slope or valley) and their type (1V, 2V, 1Ni@2V). Unpublished courtesy of C.Africh and coworkers.

The experimental analysis of the C-vacancies statistical reported in table 3.1 indicates that the 2Vs passivated by Nickel adatoms are the most abundant vacancies. Therefore, we focus on the three 2V configurations and we passivate them with an additional Ni(figure 3.1). In this case, as suggested in [112] for Ni passivated defected G on Ni(111), we calculated the formation energy of 1Ni@2V as:

$$E_{form}(1Ni@nV) = E(1Ni@G^*/Ni(100)) - E(G/Ni(100)) + n * E(G_C) - E(Ni_{fcc}) \quad (3.2)$$

where $n = 1(2)$ stands for single(double) vacancy, $E(1Ni@G^*/Ni(100))$ is the total energy of the structure with Ni passivated 2V, $E(G/Ni(100))$ is the total energy of the vacancy-free structures, $E(G_C)$ is the total energy of pristine G sheet per C atom and $E(Ni_{fcc})$ is the total energy of a Ni atom in the bulk. From this definition the larger E_{form} is, the higher is the formation cost in the otherwise perfect configuration(table 3.2).

To evaluate the stability of the structures, we calculated the adsorption energy of the Nickel adatom as:

$$E_{ads}(Ni) = E(Ni/G^*/Ni(100)) - E(G^*/Ni(100)) - E(Ni_{fcc}) = E_{form}(1Ni@nV) - E_{form}(nV) \quad (3.3)$$

where $E(Ni/G^*/Ni(100))$ is the total energy of the whole system, $E(G^*/Ni(100))$ is the energy of the system without the additional

Ni atom and $E(Ni_{fcc})$ is the energy of bulk Ni per atom. A negative value means that the adsorption is favored. As we notice from the adsorption energies $E_{ads}(Ni)$ reported in table 3.2, the adsorption of an additional Ni atom is favored, but the energetics is not enough to explain their larger concentration on ridges rather than on valleys or slopes since $E_{ads}(Ni)$ is always the same (i.e. $-0.38\ eV$). Furthermore, formation energies here calculated refer to the energy needed to remove C atoms from a perfect G layer ($E_{form}(nV)$) and, eventually, passivate the defect with an additional Ni atom ($E_{form}(1Ni@nV)$) but their very high values implies that this is very unlikely. Thus, concentration of C defects in G layer is also linked to the kinetics of the growth process which can affect their abundance.

	$E_{form}(nV)$		$E_{form}(1Ni@nV)$	$E_{ads}(Ni)$
1V ridge	4.96	1Ni@1V ridge	4.52	-0.44
1V slope	3.59	1Ni@1V slope	3.73	0.14
1V valley	3.26	1Ni@1V valley	4.07	0.81
2V ridge	6.56	1Ni@2V ridge	6.18	-0.38
2V slope	6.60	1Ni@2V slope	6.22	-0.38
2V valley	6.52	1Ni@2V valley	6.14	-0.38

Table 3.2: Formation energies of substrate passivated(column 2) and Ni passivated(column 4) 1V and 2V. Adsoprtion energies of Ni adatom is also reported for 1Ni@2V. Note that E_{form} in column 2 is calculated with equation 3.1 while E_{form} in column 4 with equation 3.2.

To check whether nickel tends to clusterize on defects, we calculated the adsorption energy of a second additional Ni atom bound to the same defects. The positive adsorption energy of 1.43 eV shows that Ni clusterization is very unlikely.
STM images of the most abundant defects were simulated. Vacancies passivated by Nickel adatom appear as bright spots, similarly to C-vacancy on Ni(111) [112], while those passivated by substrate appear as dark spots (figure 3.3). On the basis of these results, we made a comparison with the experimental images and we identified different

types of defects(figure 3.3).

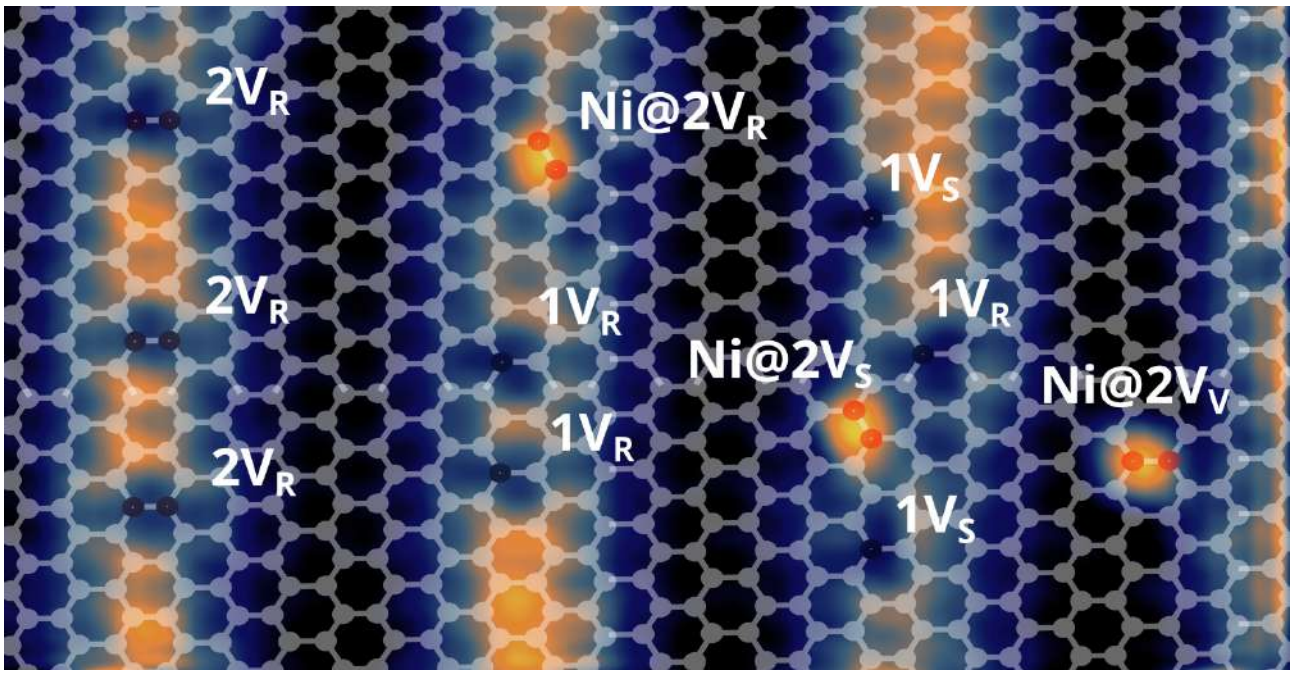

(a)

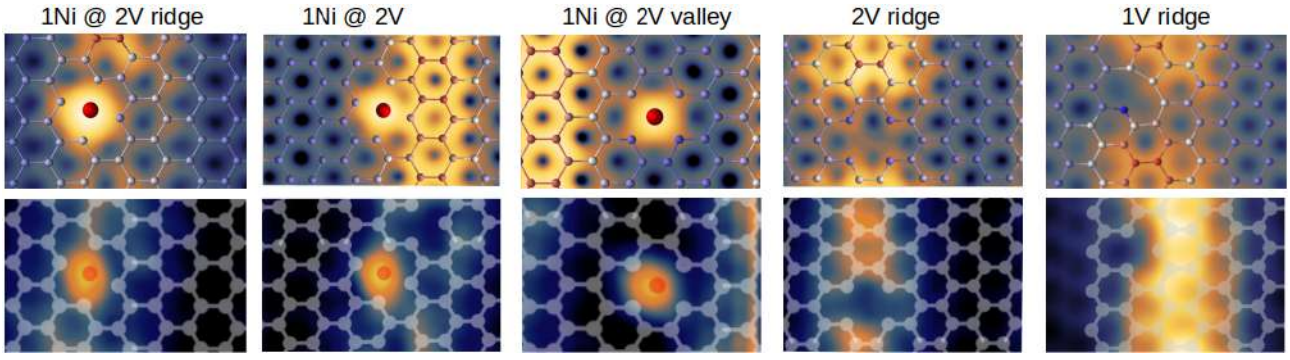

(b)

Figure 3.3: (a) Experimental STM image of different kind of C-vacancies. White stick-and-ball model of G layer has been superimposed and missing C atoms are depicted in black while Ni adatom are in red. Unpublished kind permission of C.Africh and G.Comelli's group. (b) Details of the most probable defects. First row: simulated STM image with stick-and-ball model superimposed. Second row: detail of experimental STM image.

3.3 Carbon Monoxide passivation of C-vacancies

Based on the considerations of the previous section we are confident that of all the inspected defects the most likely to occur are the 1Ni@2Vs followed by the 2Vs passivated by the substrate. To probe their reactivity we simulated the adsorption of a CO molecule. The adsorption energy is calculated as:

$$E_{ads}(CO) = E(CO/Sub) - E(Sub) - E(CO) \tag{3.4}$$

where $E(CO/Sub)$ is the total energy of the whole system,$E(Sub)$ is the energy of the substrate, i.e $E(G^*/Ni(100))$ or $E(Ni/G^*/Ni(100))$ depending on the type of defects and $E(CO)$ is the energy of an isolated CO molecule in a box. From previous studies it is known that CO does not adsorb on pristine G [113]. The adsorption of CO on G/Ni(100) is not energetically favored as well since calculated adsorption energy is positive, although small(0.01 eV). The reactivity of G changes completely with the presence of vacancies. Four representative configurations with adsorbed CO molecule on 2V passivated by Ni adatoms or by the substrate are presented in figure 3.4. All configurations display negative $E_{ads}(CO)$, indicating that the adsorption of CO is energetically favored. However, the most favored configuration is CO adsorbed on 1Ni@2V on valley. In any case, adsorption energies of CO on defected G are lower than adsorption energies of CO on clean Ni(100)[114], meaning that the presence of G weakens the CO strong adsorption.

We simulated STM images of each configuration and compared them with experimental one. Experimentally, after CO exposure, we can distinguish bright spots on ridges and on valleys. Trying to assign a proper structural model to each type of image, as we can see from figure 3.5, 2V on ridge passivated either by Ni or by the substrate with CO show very bright spots which fit very well with the experimental image. Anyway also 1Ni@2V, studied in previous

section, could be a third candidates for these very bright spots. For spots on valley we also have three different candidates: 2V passivated by Ni with and without CO and 2V passivated by substrate with CO.

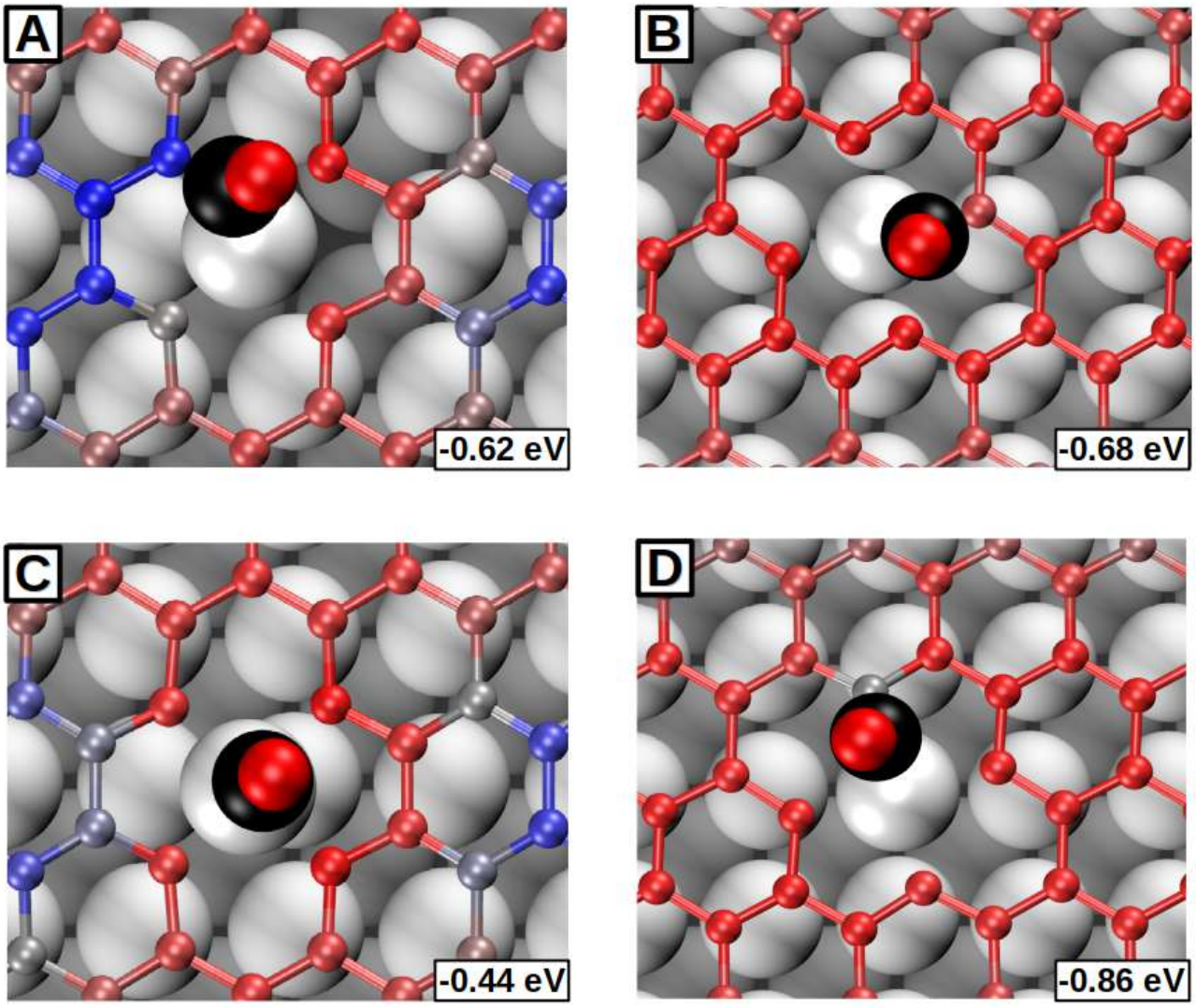

Figure 3.4: Carbon Monoxide molecule adsorbed on 2V vacancy passivated by substrate on ridge(a) and on valley(b) and 2V vacancy passivated by additional Ni adatom on ridge(c) and valley(d). $E_{ads}(CO)$ calculated as in equation 3.4 is reported in the bottom right square of each configuration. E_{ads} calculated as in equation 3.4.

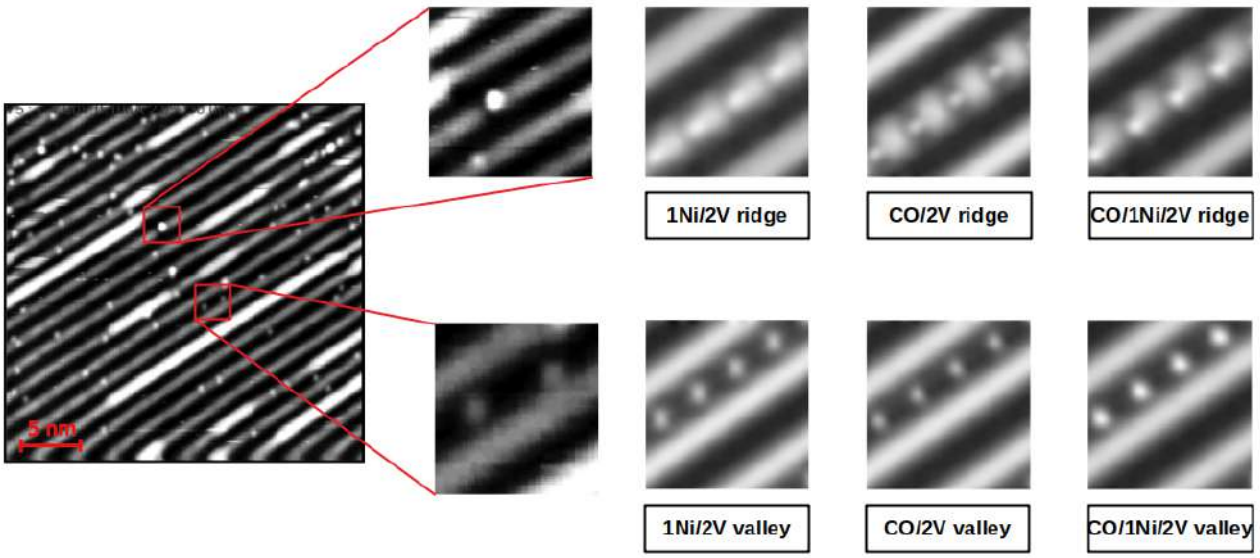

Figure 3.5: Experimental STM image after CO exposure showing many bright spots. Candidates for them are reported on the right. Experimental bright spots are compatible both with the presence o CO and with Ni passivation of Nickel. Unpublished kind permission of C. Africh and G. Comelli's group

3.4 Co passivation of C-vacancies

Graphene's vacancies reactivity has been probed with Co adatom as well. Conversely to CO, Co adatom can bind on pristine G/Ni(100) so we have investigated also this case. Co adatoms on hollow sites on ridges and on valleys have been considered (figure 3.6) and their adsorption energy has been calculated as:

$$E_{ads}(Co) = E(Co/G/Ni(100)) - E(G/Ni(100)) - E(Co) \quad (3.5)$$

where $E(Co/G/Ni(100))$ is the total energy of the system with Co adatom, $E(G/Ni(100))$ is the energy of $G/Ni(100)$ and $E(Co)$ is the total energy of an isolated Co atom.
The adsorption energy for Co on ridge is 1.50 eV, i.e. 0.50 eV higher than on valley. Moreover, from Löwdin charge analysis Co donates $\approx 0.5e$ to G, both on valley and on ridge, while the surface Ni atoms below the ridge remains neutral and those below valleys do-

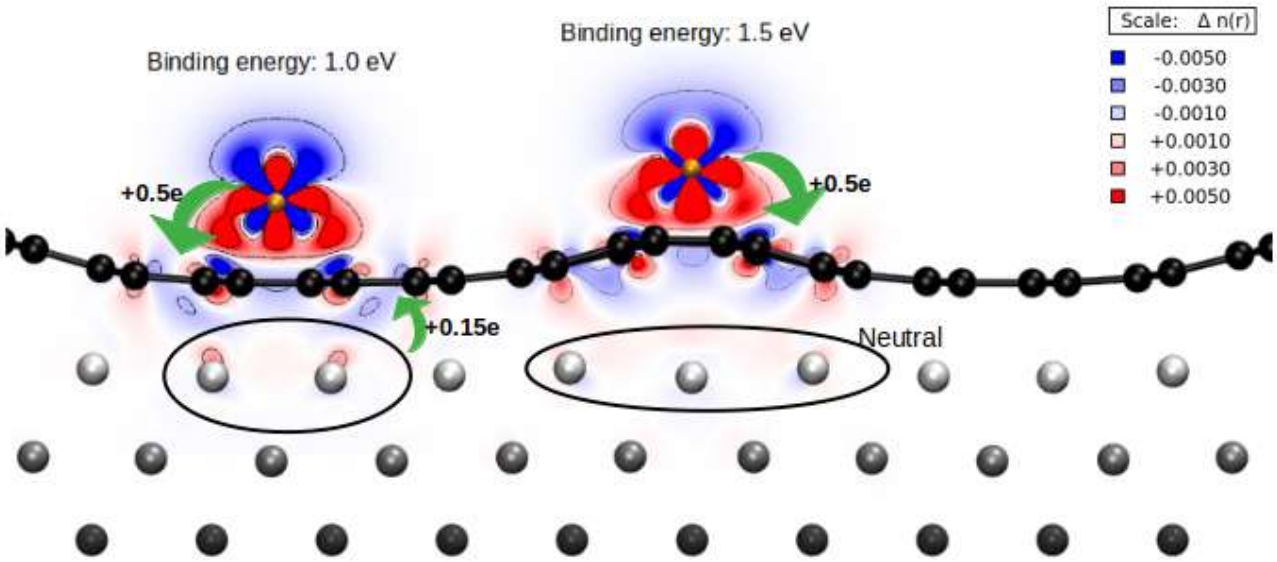

Figure 3.6: Induced charge density upon Cobalt adsorption on ridge and on valley. On valley both Co and Nickel underneath donates electrons to G giving rise to a repulsive interaction between Co and Ni. On the ridge only Co donates electrons to G thus the CO-Ni repulsion is weaker.

nate $\approx 0.15e$ to G, thus becoming slightly positively charged. This is also qualitatively visible from the induced charge density plot upon adsorption of Co on G/Ni(100) in figure 3.6. Therefore, charge analysis reveals a global electrostatic repulsive interaction between Co and Ni substrate. This explains the higher Co binding energy on ridge: the farther is the Co from Ni substrate, the weaker is the repulsion and the higher is the binding energy of Co on graphene.

Due to the repulsive character of this interaction, the presence of the Nickel substrate increases the mobility of Co on G as it reduces the diffusion barrier. Indeed, as we can see from figure 3.7, the diffusion barrier on pristine graphene is $\approx 0.1\ eV$ larger than that for the diffusion along the ridge and $0.3\ eV$ larger than along valley. Furthermore, Co diffusion from valley to ridge is favored rather than vice versa, thus leading to a higher concentration of Co adatoms on ridge.

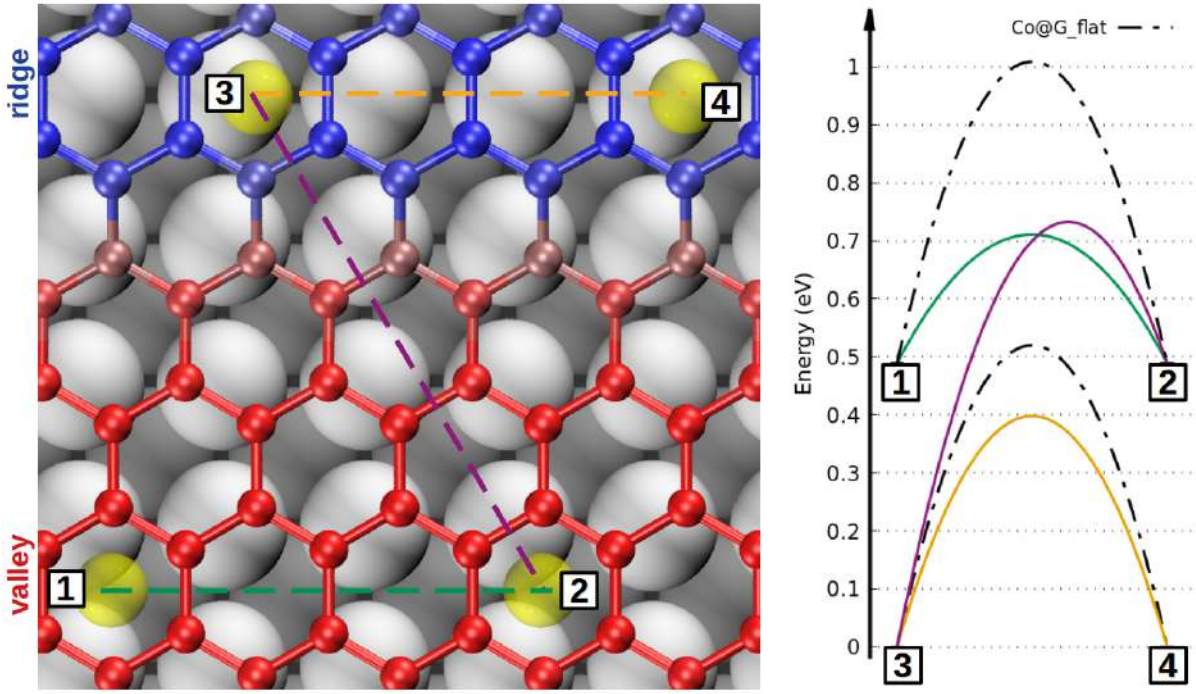

Figure 3.7: Adsorption energies and diffusion barriers diffusion for a Co adatom on G/Ni(100) along the ridge(yellow), along the valley(green) and from ridge to valley(purple). Dashed Black line in the plot on the right indicates energy barrier for diffusion of Co on free and flat G layer without any substrates(the position is shifted for comparison).

C-vacancies as hook for Co

As for Carbon Monoxide, defects in G on Ni(100) affect its reactivity upon Co adsorption. Since 1Ni@2Vs are the most likely kind of defects, we investigated the adsorption of Co adatom only on such defects. The adsorption energy has been calculated as:

$$E_{ads}(Co) = E(Co/G^*/Ni(100)) - E(G^*/Ni(100)) - E(Co) \quad (3.6)$$

where $E(Co/G^*/Ni(100))$ is the total energy of the system with Co adatom, $E(G^*/Ni(100))$ is the energy of defected G on Ni(100) and $E(Co)$ is the total energy of isolated Co.
The adsoprtion energies are 2.43 eV and 2.59 eV for Co on 1Ni@2V on valley and ridge respectively, significantly higher than in absence of defects (figures 3.8a and 3.8b). Furthermore, Co adatoms attaches to the Ni trapped in 2V with very low barriers both on valley and on ridge as shown by NEB calculations in figure 3.9.

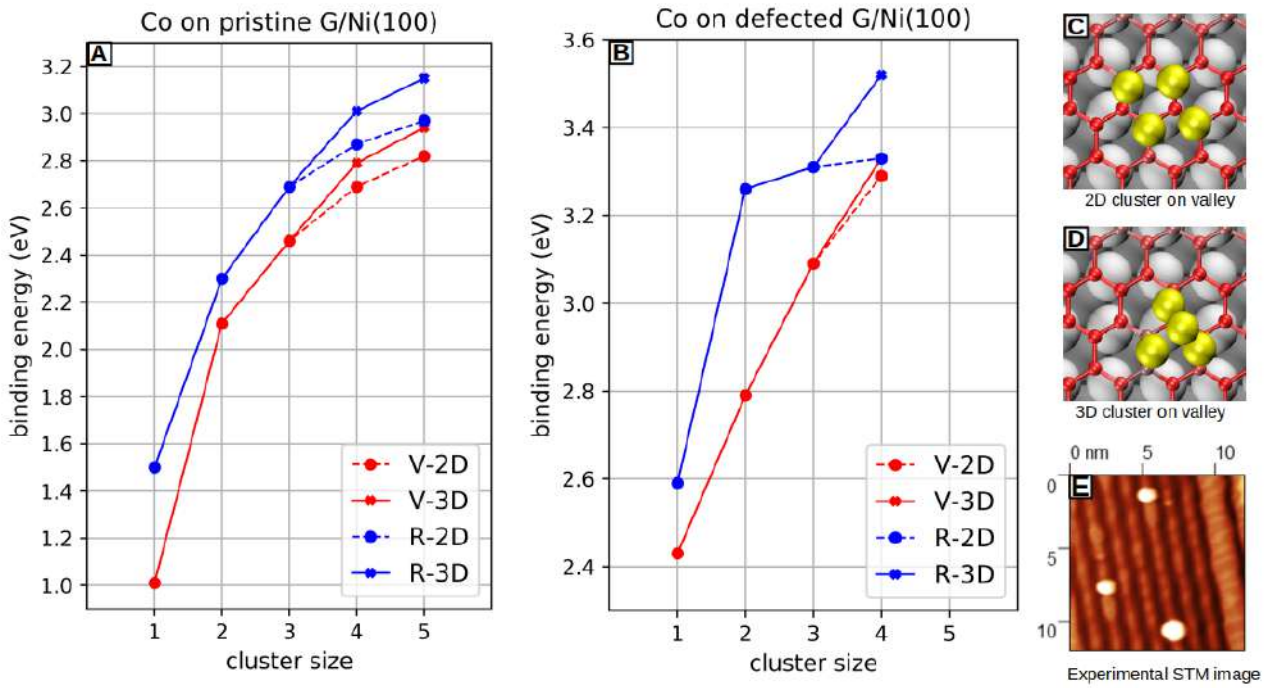

Figure 3.8: Binding Energy of different sizes Co clusters on pristine G/Ni(100)(a) and defected G/Ni(100)(c) on ridges(blue) and valleys(red). For clusters of 4 and 5 atoms the results are different for a 2D/3D shape. Examples of 2D and 3D Co cluster are reported in the insets (c) and (d) respectively.(e) Experimental STM image with Co clusters only on ridges and not on valleys, as predicted by simulations. Unpublished kind permission of C.Africh and G.Comelli's group.

At this point we can compare the tendency of Co to make clusters on the passivated vacancy and on pristine G. We calculated the adsorption energies per Co atom of clusters with 2,3,4 and 5 adatoms, both on valley and on ridge as:

$$E_ads(nCo) = \frac{1}{n}(E(nCo/G^*/Ni(100)) - E(G^*/Ni(100)) - nE(Co)) \tag{3.7}$$

where n is the number of Co in the cluster, $E(nCo/G^*/Ni(100))$ is the total energy of the system with Co cluster, $E(G^*/Ni(100))$ is the defected G and $E(Co)$ is the energy of an isolated Co atom. From figure 3.8 we can clearly see that the adsorption on ridge sites is favored in any case (blue lines are always at higher values than the red ones). Furthermore, the formation of these small clusters is favored on the Ni passivated vacancy rather than on the pristine G, but the difference progressively reduces by increasing the cluster

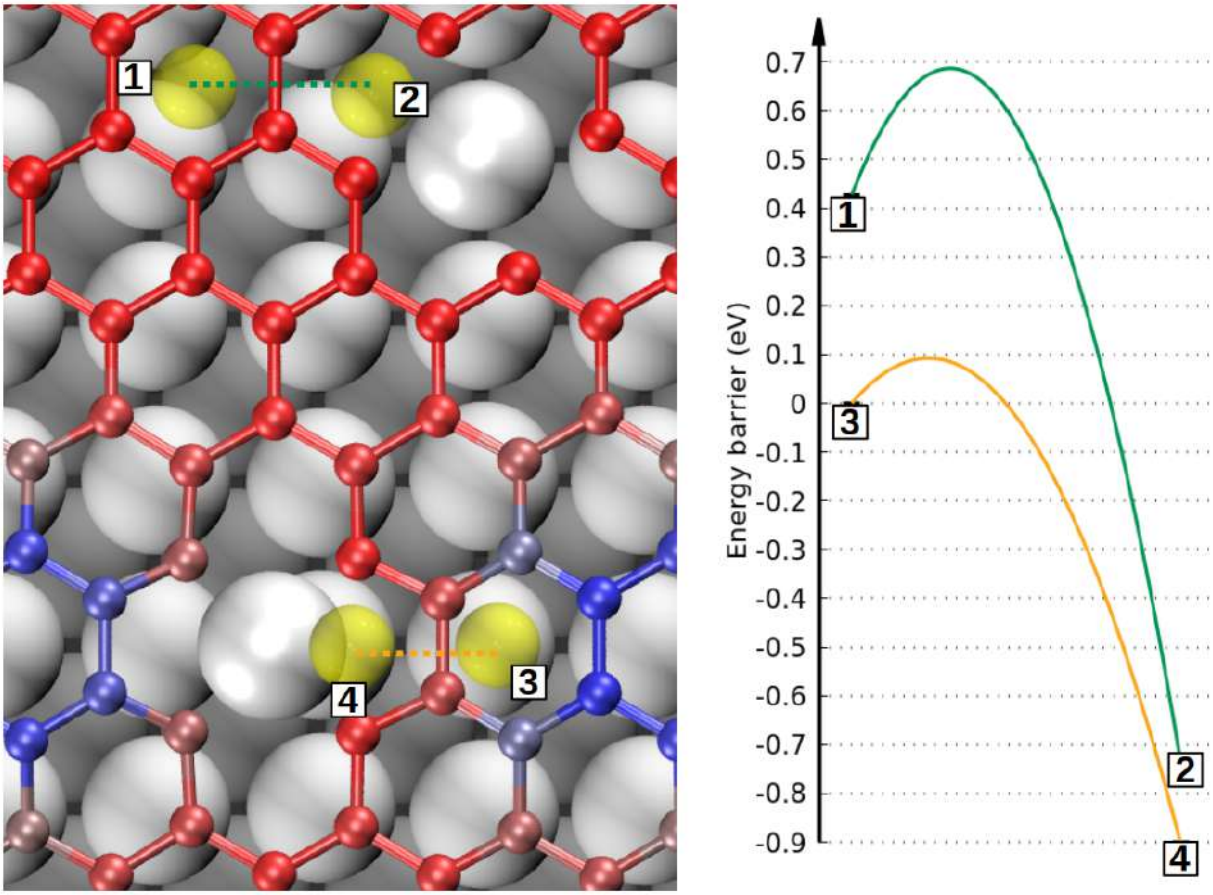

Figure 3.9: Energy barriers for Co to attach on Ni adatom passivated 2V on ridge(yellow) and on valley(green). In both cases barriers are very low and the energy gain is very high.

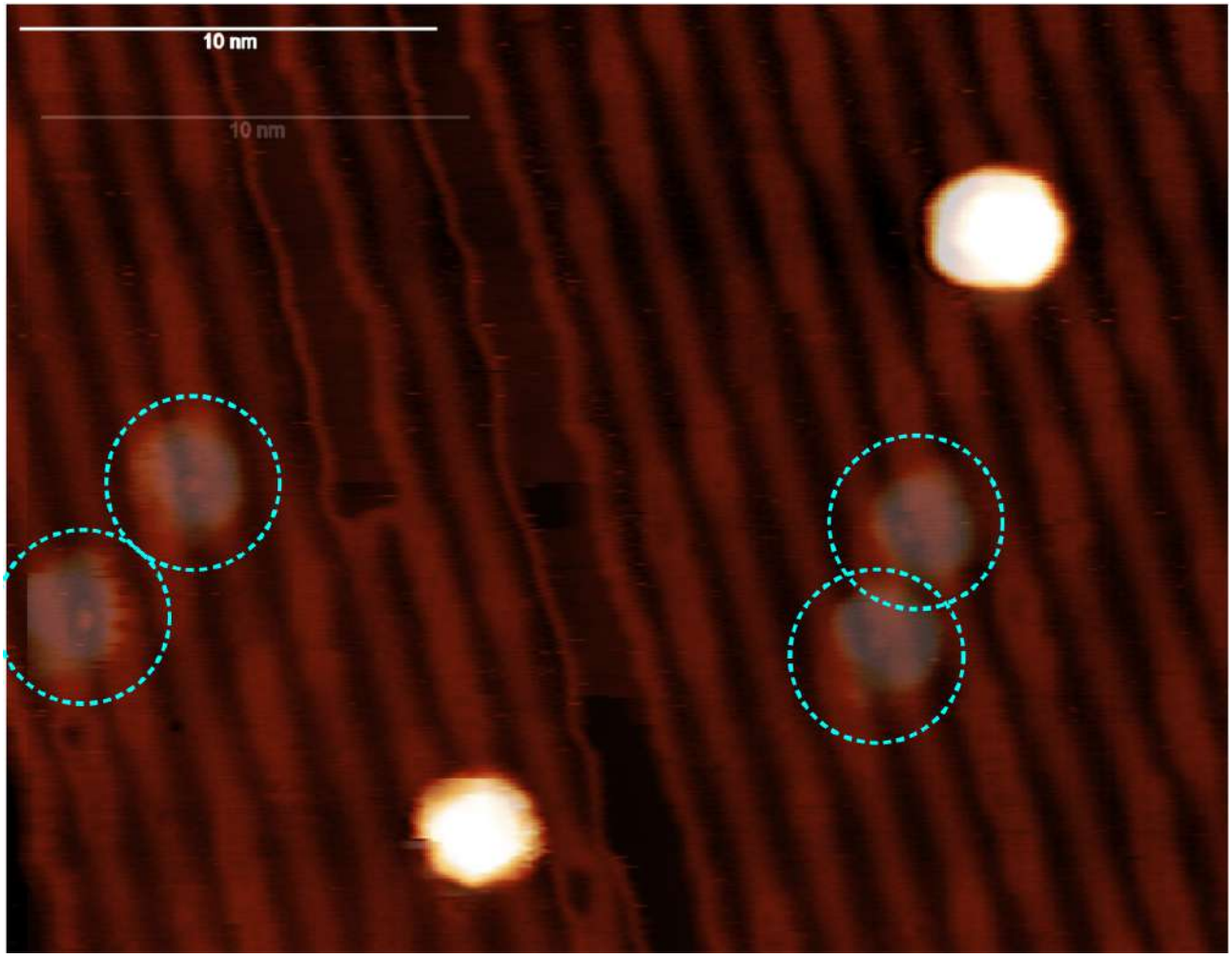

Figure 3.10: Experimental STM image of Co cluster (large bright spot) on ridges of G/Ni(100) interface. Under some of them(circled by light blue lines) can be seen a smaller bright spot which seem to be a trapped Ni adatom, compatibly with results of previous section. Unpublished kind permission of C.Africh and G.Comelli's group.

size. Ni passivated vacancies can therefore act as a hook for Co clusterization and this seem also to be confirmed by experimental STM image in figure 3.10 where we can see that they are right above Ni passivated C-vacancies of G.

Chapter 4

Blue-Phosphorus on Au(111)

In the last few years different 2D allotropes made only by phosphorus atoms raised particular attention owing to their unusual features and various potential applications in electronic and optoelectronic devices [115] [116] [117] [118] [119] [120] [121] [122] [123] [124] [125] [126] [127] [128]. Among them,a single layer of Black-Phosphorene(BLP), obtained through exfoliation from the 3D parent material [127], is one of the most important due to its high stability, high carrier mobility and the intrinsic bang gap of $\approx 2eV$ around Γ point [3] [127] [129] [130] [131] and it has already been widely studied both theoretically and experimentally [127] [132] [133] [134] [135] [136].

On the other hand, a new 2D phosphorus allotrope, called Blue-Phosporus(BP) , has been computationally proposed by [132] which in principle should share many intriguing properties as BLP but with a smaller bang gap of $\approx 1.2eV$ [137] [138] [139] [140] [141] [142]. BP has not the bulk counterpart so it cannot be obtained through mechanical exfoliation as BLP but it should be obtained using bottom-up methods, such as epitaxial growth. As for graphene, a successful growth depends on the choice of the substrate but the great reactivity of P atoms makes it more challenging. Recent papers [143] [144] indicated Au(111) as a good substrate candidate to grow a single BP layer from purified black phosphorous, but also less expensive methods using other phosphorous allotropes are currently under study. It seems to arranges in more flat honeycomb structure than BLP but

its precise structure on Au(111) is still unclear and controversial. STM images of BP grown on Au(111) have been recently taken by experimental colleagues of CNR and of Physics Department of University of Trieste, showing interesting features not fully discussed in [143]. In addition, ARPES spectra have also been taken, suggesting that BP contributes with new features to the band structure mainly between -1 eV and -2 eV.
In this chapter we propose a refined structural model for BP grown on Au(111) through DFT simulations starting from literature. Using a new computational technique, tested during this work, we investigate the contributions of P atoms to the electronic band structure of the proposed model offering relevant information to explain the ARPES spectra and maps.

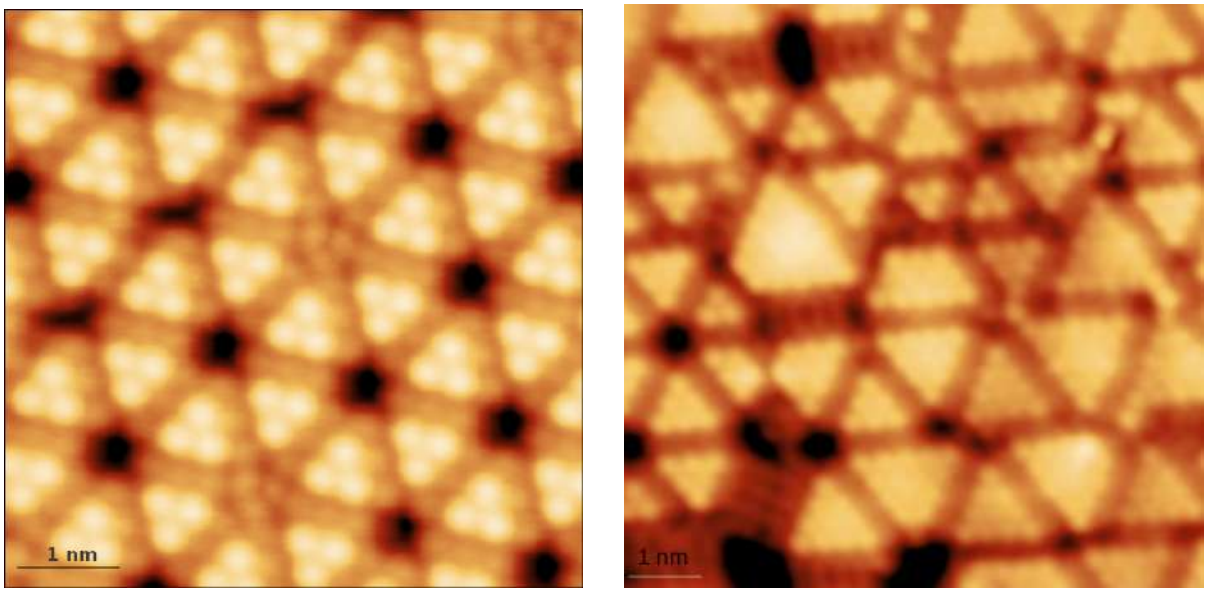

(a) (b)

Figure 4.1: Experimental STM images of Blue-Phosphorus on Au(111). (a) Detailed image which clearly show the bright triangular shaped BP domains [V_{bias} = - 0.8 V, I = 0.2 nA]. (b)Large scale image with BP domains of different size [V_{bias} = - 0.4 V, I = 1.0 nA]. Unpublished kind permission of A. Sala.

4.1 Computational details

Spin-polarized DFT calculations were carried out using the QUANTUM ESPRESSO package. Exchange-correlations terms were taken into account by means of Perdew-Burke-Ernzerhof (PBE) functional within the generalized gradient approximation (GGA). The use of van der Waals correction is essential: Grimme-D3 scheme [145] were used since Grimme-D2 scheme leads to fictitious Au surface reconstruction during structural optimizations.
To model Au(111) surface a slab geometry with 4 layers has been used, with a lattice parameter of 4.15 Å. In particular, to host the BP, we used an hexagonal supercell with in-plane dimensions set to 5×5 times the unit cell of Au(111) and 12 Å of vacuum space along z-direction. During structural optimizations all atoms but those in the bottom Au layer were allowed to relax. A 2×2×1 k-mesh for Brillouin zone sampling has been used for the *scf* cycle, and *nscf* calculations with fixed potential were performed with a 4×4×2 k-mesh before band structure calculations. Cutoffs of 40 Ry and 300 Ry were used for the plane-wave expansion and for the charge density, respectively. The Methfessell-Paxton smearing of the electron gas with an energy broadening of 0.01 Ry was used to improve the convergence of the self-consistent cycle [39] . STM images were simulated employing the Tersoff-Hamann scheme [46].
For a meaningful comparison of the ARPES spectra and maps with the calculated band structure, it would be useful to have the contribution of each atom resolved in k-space. The use of supercells in simulations has the drawback that the band structure plots are complicated by folding, since the Brillouin zone is reduced with respect to the original reference cell. A direct comparison with the experimental data is therefore impossible. A non trivial procedure of unfolding and projecting on the atomic orbitals has to be applied to the standard output of the pseudopotentials plane-wave calculations.

A. Ferretti implemented such a procedure in a code interfaced with the QE [146], that has been carefully tested during this thesis.
Unfolded and atomic-projected electronic band structures along Γ - K and Γ - M paths were performed with a sampling of 200 different k points each. ARPES map were also obtained with the same package using a 2D equally spaced grid of 900 k-points.

4.2 Clean Au(111): testing the band unfolding procedure

In order to test the new QE package for band structure unfolding we compared the bands calculated on the Au(111) unit cell using QE's projwfc.x package with those unfolded from the 5×5 supercell along Γ - K and Γ - M paths. As we can see from image 4.2, unfolded band structures (4.2c and 4.2f) agree very well with those calculated on the Au(111) unit cell. In the former case bands are a bit more widespread due to the reduced energy mesh and the low number of k points chosen for the unfolding algorithm but they couldn't be increased for computational reasons. In any case, the main features of Au 3d states between -2 eV and -6 eV are still clearly visible. The unpleasant feature is the position of the parabolic Shockley surface state at Γ point which is around the Fermi level in calculated band structures but it is well known that it should be around 0.5 eV below [147].
We increased the number of layers to 6,9,12 and 21 in the Au(111) unit cell and we calculated their electronic structure for Γ - K path using the new package for unfolding(figure 4.3). As the number of layers increase the Shockley surface state goes down and stabilizes at around $-0.4eV$, therefore the result found in the 4 layers configurations is due to a too thin Au(111) slab model. Since we cannot computationally afford a 5×5 supercell with more than 4 layers, this is something that we have to keep in mind when we will examine our results for BP on Au(111).

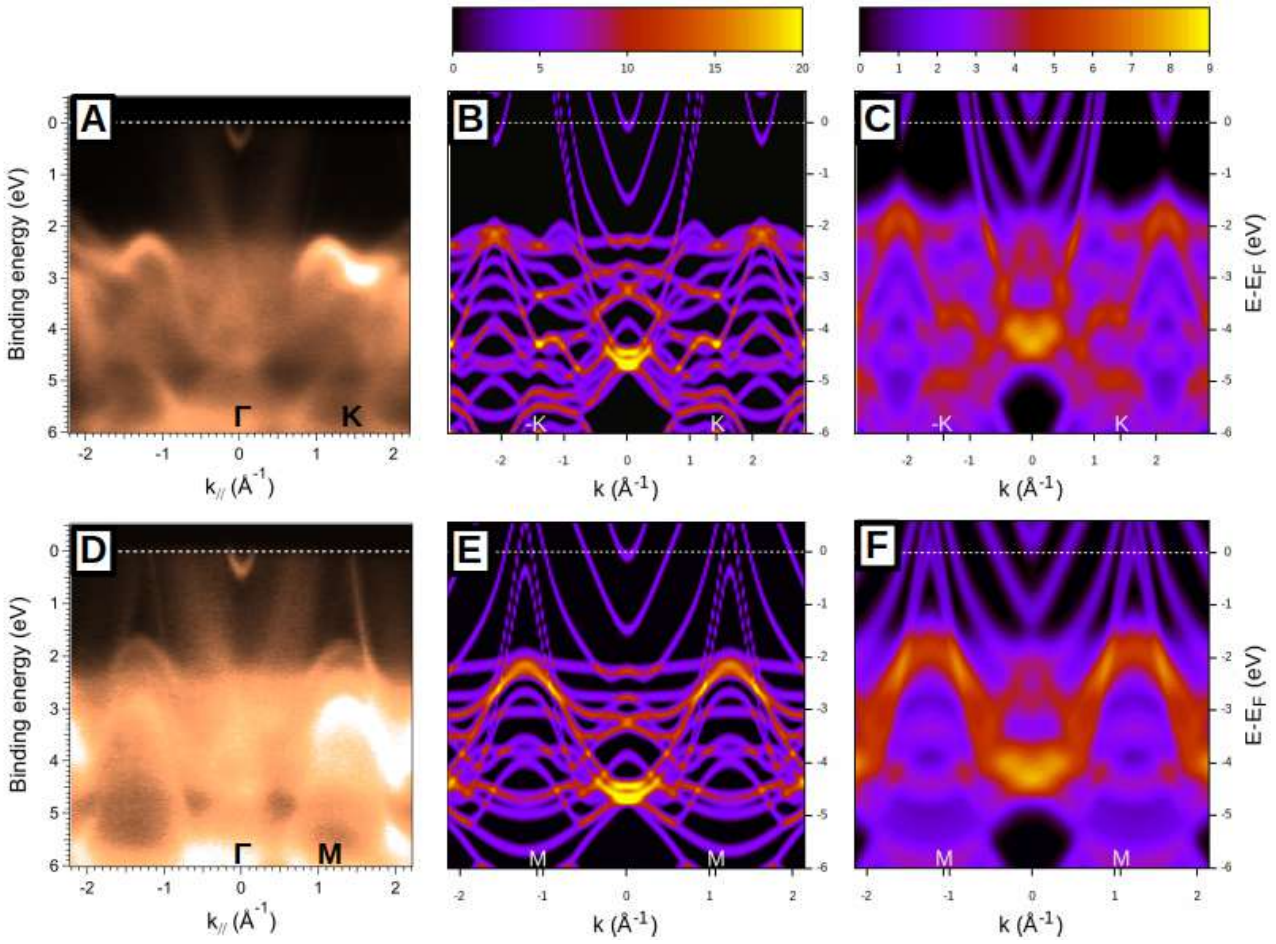

Figure 4.2: (a)((d)) Experimental ARPES spectra for clean Au(111) along $\Gamma - K(\Gamma - M)$ path. Unpublished kind permission of A. Sala. (b)((e)) Band structure of clean Au(111) surface calculated in the unit cell of Au(111) along $\Gamma - K(\Gamma - M)$ path using QE's projwc.x package. (c)((f)) Unfolded band structure of clean Au(111) surface calculated using the 5×5 supercell along $\Gamma - K(\Gamma - M)$ path with the new package for unfolding. The color intensity describes spectral function defined in equation 1.30. All spectra have Fermi level set to 0 eV. Color scale of images is reported above for each column(images in the same column have the same color scale).

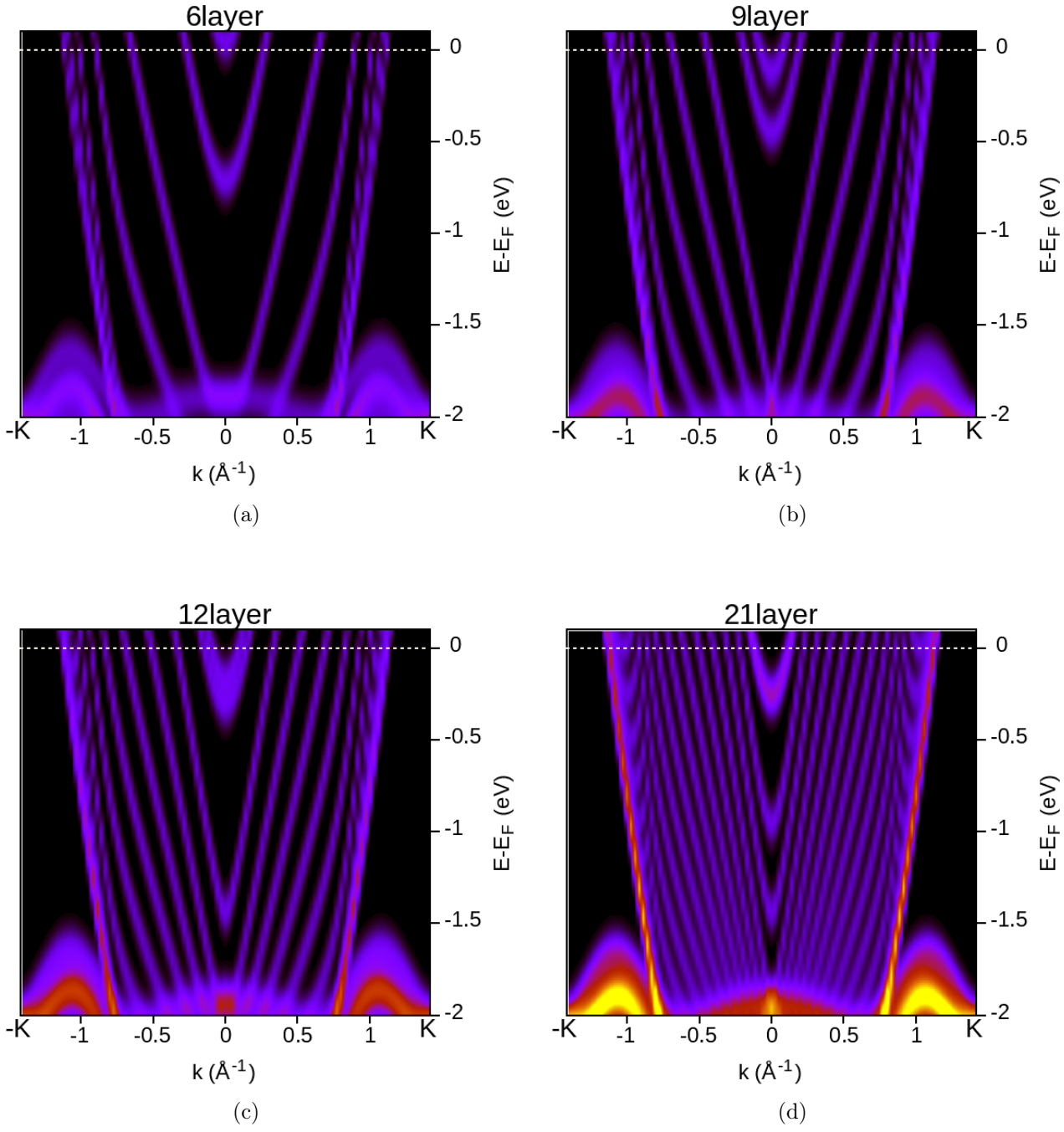

(a) (b) (c) (d)

Figure 4.3: Detail of band structure of clean Au(111) along $\Gamma - K$ path calculated on the unit cell and for slabs with 6(a),9(b),12(c) and 21(d) number of layers. The Shockley surface state goes down as the number of layers increases. Fermi level is set to 0 eV and color scale is the same as in figure 4.2.

4.3 BP models on Au(111)

Structural models

From experimental STM images in figure 4.1 BP on Au(111) seem to form an ordered phase with triangular flakes of similar size arranged in a regular pattern. The periodicity of such a system seems to be 5 times the Au(111) unit cell along the two in-plane directions, compatible with what reported in [148] [143]. In this work we constructed two possible models for BP on Au(111), both in a 5x5 supercell and following what already proposed in literature: one with two pyramidal-shaped islands of BP with 9 P atoms each ($P_9 \times 2$ model, figure 4.4 a) and one with the BP structure but with 9 Au atoms in between the P island($P_9 \times 2 + Au_9$ model, figure 4.4 b). Possible configurations with a monolayer of BP have not been taken into account since we already know from literature that this case can be excluded [149].

E_{ads} for each P atom have been calculated as (tab. 4.1):

$$E_{ads} = \frac{1}{N_P}\left(E_{BP/Au(111)} - E_{Au(111)} - N_P E_P\right) \tag{4.1}$$

where N_P is the number of P atoms in the cell, $E_{BP/Au(111)}$ is the total energy of the structure, $E_{Au(111)}$ is the energy of the Au substrate and E_P is the energy of the isolated P atoms. This definition therefore also contains the cohesion energy of the P layer architecture. $P_9 \times 2 + Au_9$ model is more favorable than $P_9 \times 2$ due to the presence of additional Au edge atoms which stabilize BP flakes. As reported in table 4.2, the structure parameters of BP in the $P_9 \times 2 + Au_9$ model are more similar to the structure parameters of freestanding BP than in the $P_9 \times 2$ model meaning that BP is closer to its equilibrium configuration when Au edge atoms are present.

For both models, the simulated STM images (figure 4.4a-b) show triangular shaped flake of BP but at a closer inspection $P_9 \times 2 + Au_9$

model fits better on the edge of such domains due to the presence of additional Au adatoms (figure 4.4c).

structure	E_{ads} per P atom (eV)
$P_9 \times 2$	-0.81
$P_9 \times 2 + Au_9$	-1.04

Table 4.1: Adsoprtion energies E_{ads} per P atoms of the two models calculated with equation 4.1 .

	$\langle \Delta z_{Au-P} \rangle$ Å	$\langle \Delta z_{P-P} \rangle$ Å	$\langle \Delta r_{Pabove} \rangle$ Å	$\langle \Delta r_{Punder} \rangle$ Å
$P_9 \times 2$	1.69	1.15	3.47	3.39
$P_9 \times 2 + Au_9$	2.45	1.18	3.33	3.22
BP_free	–	1.26	3.29	–

Table 4.2: Geometric distances of the two investigated models. Distance along z-axis between first layer of Au and P layer closest to the surface(Δz_{Au-P}) and between the two out of plane P layers(Δz_{P-P}). Coplanar distance between nearest-neighbor of P in the lower (Δr_{Punder}) and highest (Δr_{Pabove}) P layer are also reported.

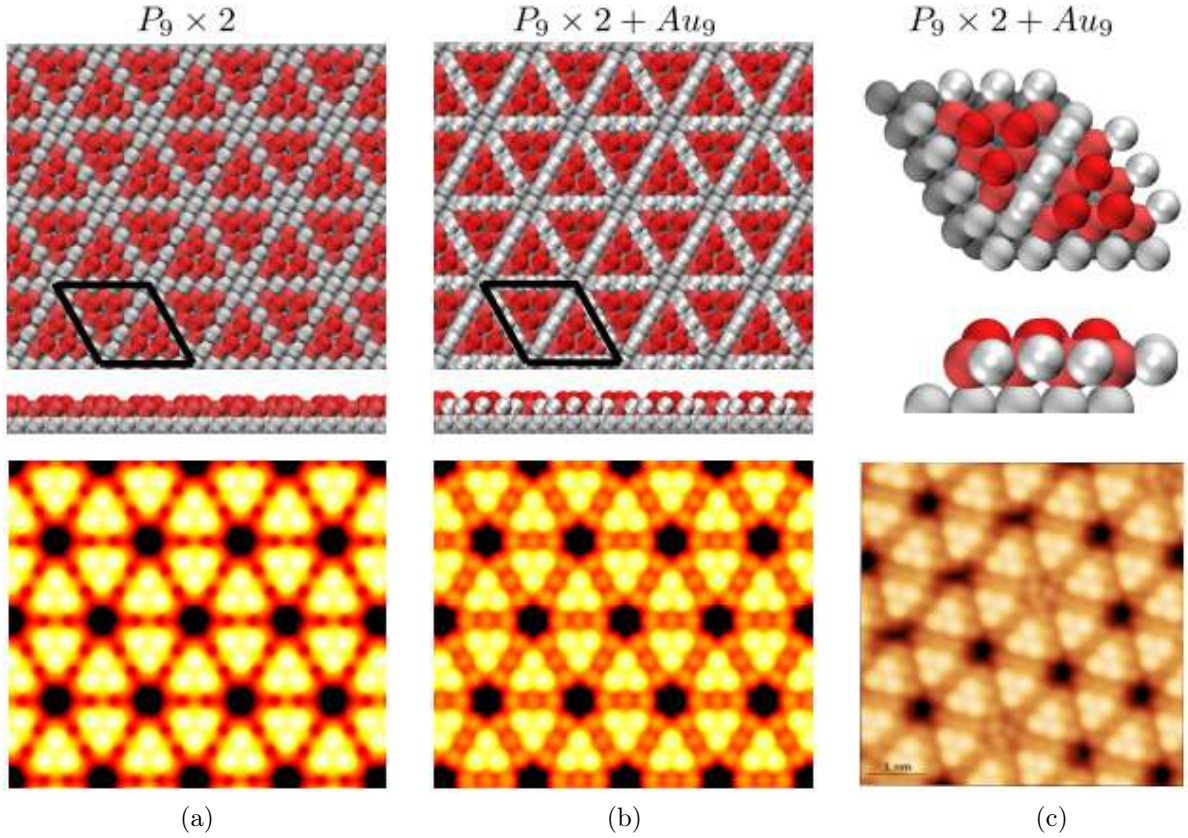

Figure 4.4: (a) $P_9 \times 2$ model. (b) $P_9 \times 2 + Au_9$ model. 5×5 supercell is denoted with black thick lines. Top and side view of structural models are reported in the first and second row respectively and simulated STM images of each model in the bottom image. The $P_9 \times 2 + Au_9$ STM image show both bright triangular shaped BP domains and bright spots at their edges in agreement with experimental STM image in figure 4.1. (c) Experimental STM image [V_{bias} = - 0.4 V, I = 1.0 nA] with top and side view of $P_9 \times 2 + Au_9$ stick-and-ball model in the 5×5 supercell.

4.4 Band structure calculations

To further investigate the BP fingerprint, band structure calculations for both models along Γ - K and Γ - M have been calculated and compared with ARPES Spectra. Unfolding of band structure is fundamental for comparison since our structural models have been obtained in the 5×5 supercell. The band structures calculated for $P_9 \times 2$ model are reported in figure 4.5. The BP layer contributions, both for Γ - K and Γ - M paths, is between Fermi energy and $-1\ eV$ but this is not compatible with experimental ARPES spectra. Conversely, the band structures of $P_9 \times 2 + Au_9$ model in figure 4.6 shows a clear contribution of BP layer between -1 eV and -2 eV, as detected

experimentally.
Even more captivating is the comparison between ARPES map and the simulated ones (figures 4.7, 4.8, 4.9 and 4.10). At Fermi energy experimental ARPES map of clean Au(111) and of BP/Au(111) (figures 4.7a-h) are significantly different: while in clean Au(111) a bright circle is present around Γ point correspondent to the surface state of gold, in BP/Au(111) it is faded away by the presence of BP. From our calculation, this is compatible only with $P_9 \times 2 + Au_9$ model (figures 4.7d-e-f-g-h) since ARPES maps for $P_9 \times 2$ show a clear bright spot at Γ point due to new states supplied by the BP layer (figures 4.8d-e-f). Furthermore, edges of the Brillouin zone seem to be closer one to each other for the configuration with BP than for the clean surface, both the for experimental and calculated maps of $P_9 \times 2 + Au_9$ (figures 4.7b-d). The BP contribution at the Fermi energy seems to be just around the edge of the Brillouin zone and in particular on the vertex of the hexagon as shown from bright spots in image 4.7h.
The trace of BP is much more evident in experimental maps at 1.00 eV where dark triangles on the edge of the hexagon, present in the ARPES map of clean Au(111) (figure 4.9a), completely disappear in the case with BP (figure 4.9c). In simulated maps of $P_9 \times 2$ model (figure 4.10d-e-f) dark triangles are still present so only ARPES maps of $P_9 \times 2 + Au_9$ model are compatible with such effect (figure 4.9d-e-f-g-h) and it is due to the presence of BP with Au edge since maps projected into the P and Au edge atoms shows the contribution right there (figure 4.9g-h).
Moreover, in simulated maps of $P_9 \times 2$ model a bright spot at Γ point is still present while in $P_9 \times 2 + Au_9$'s (figure 4.10d-e-f) is absent, as in the experimental ones (figure 4.10c).
To conclude, also band structure calculations seem to point towards $P_9 \times 2 + Au_9$ model as the most compatible.

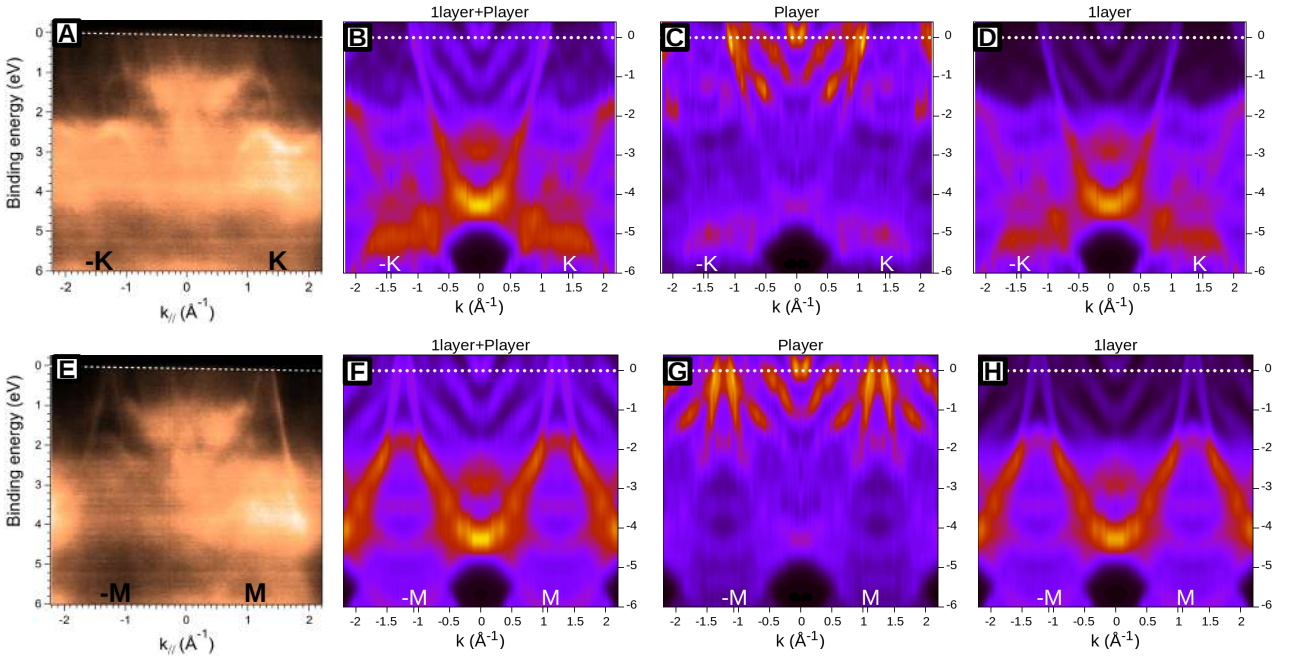

Figure 4.5: (a)(e) Experimental ARPES spectra along the $\Gamma - K$ ($\Gamma - M$) path for $P_9 \times 2$ model. Since only first few layers of the interface contribute to the experimental spectra, calculated band structures in (b) and (f) reports the sum of BP layer and first layer of Au contributions. Calculated single component contributions are also shown in (c) and (d) for $\Gamma - K$ path and in (g) and (h) for $\Gamma - M$. BP fingerprint is around Fermi level for both paths indicating that this may not be the right model.

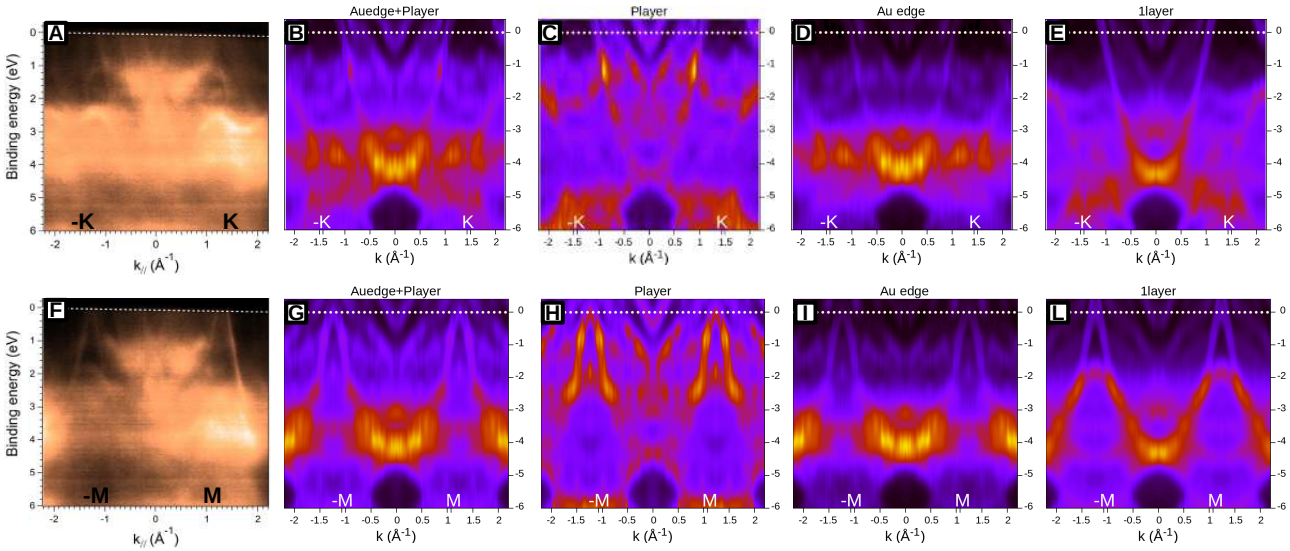

Figure 4.6: (a)(f) Experimental ARPES spectra along the $\Gamma - K$ ($\Gamma - M$) path for $P_9 \times 2 + Au_9$ model. Since only first few layers of the interface contribute to the experimental spectra, calculated band structures in (b) and (g) reports the sum of BP layer and Au edge (Au_9)contributions. Calculated single component contributions are also shown in (c),(d) and (e) for $\Gamma - K$ path and in (h),(i) and (l) for $\Gamma - M$. In this case, BP contribution is between -1 eV and -2 eV for both paths in agreement with experimental ARPES spectra in (a) and (f).

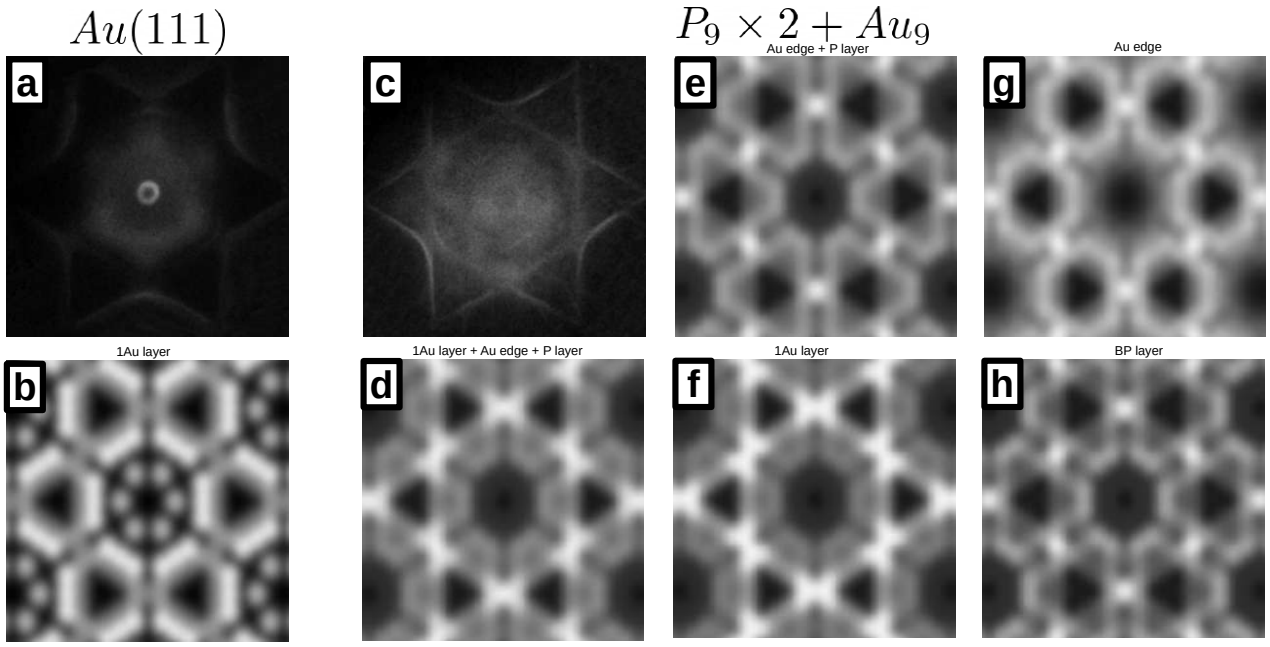

Figure 4.7: (a) Experimental ARPES map of clean Au(111) surface. (b) Calculated ARPES map projected into first layer of clean Au(111) surface. (c) Experimental ARPES map of BP on Au(111) surface. Calculated ARPES maps for $P_9 \times 2 + Au_9$ projected into BP atoms(h), Au edge atoms(g) and first Au layer atoms(f) are also reported. Since only first few layers of the interface contribute to the experimental spectra, sum of the three single component(d) and of BP and Au edge(e) contributions are plotted for comparison with experimental ARPES map. Experimental and calculated maps were taken at Fermi energy.

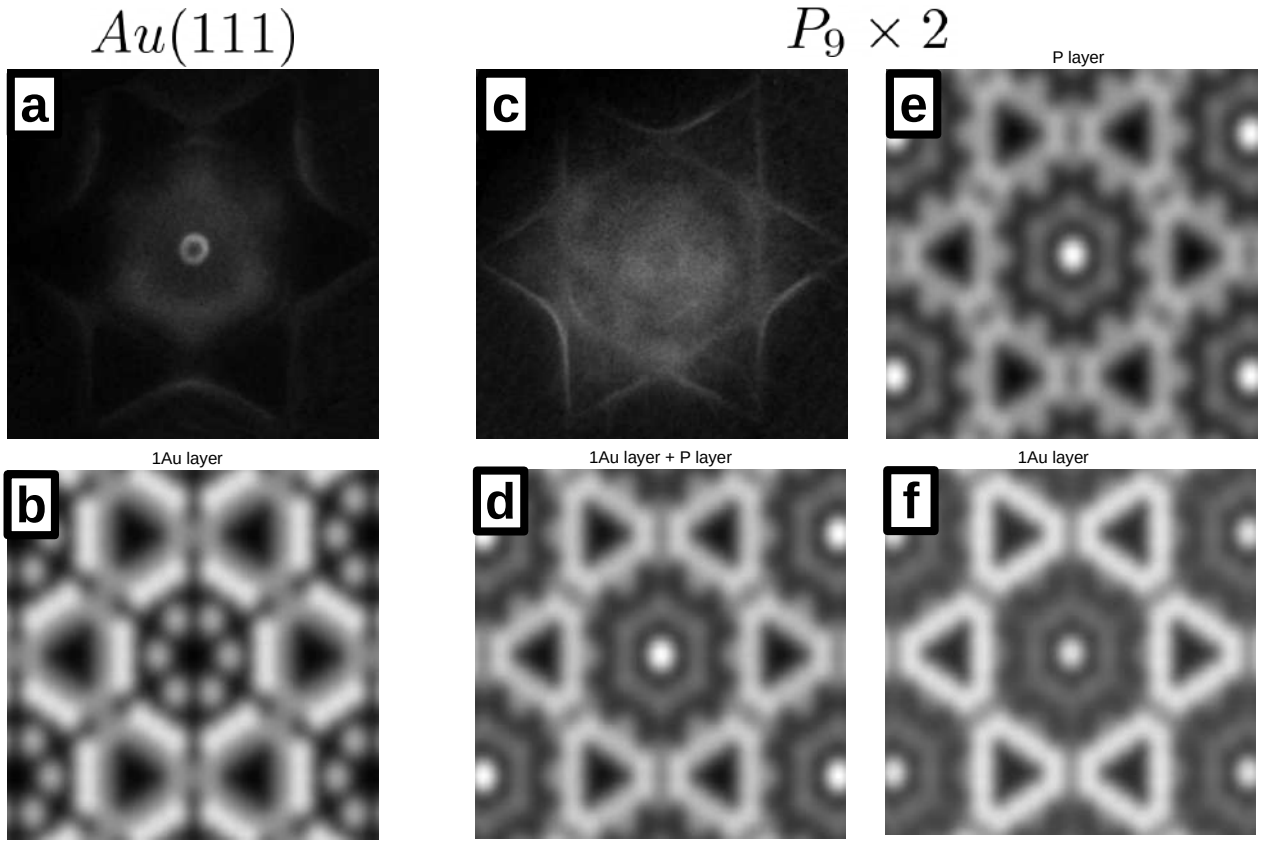

Figure 4.8: (a) Experimental ARPES map of clean Au(111) surface. (b) Calculated ARPES map projected into first layer of clean Au(111) surface. (c) Experimental ARPES map of BP on Au(111) surface. Calculated ARPES maps for $P_9 \times 2$ projected into BP atoms(e) and first Au layer atoms(f) are also reported. Since only first few layers of the interface contribute to the experimental spectra, sum of BP and first Au layer(d) contributions are plotted for comparison with experimental ARPES map. Experimental and calculated maps were taken at Fermi energy.

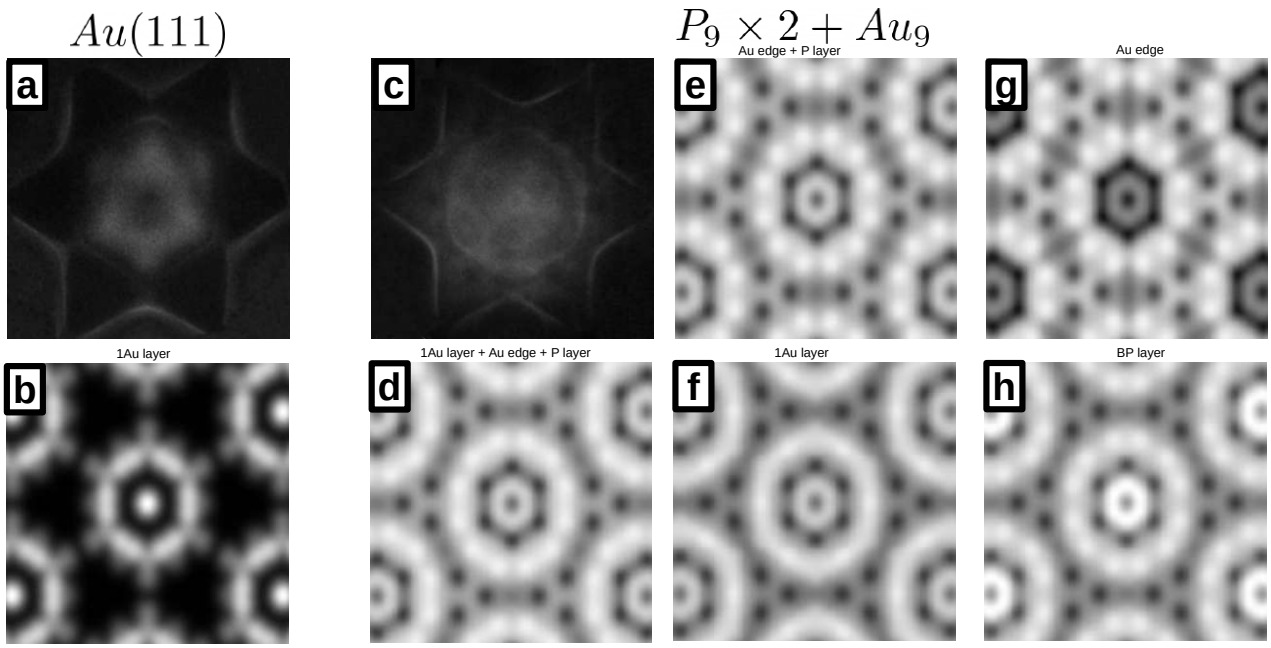

Figure 4.9: (a) Experimental ARPES map of clean Au(111) surface. (b) Calculated ARPES map projected into first layer of clean Au(111) surface. (c) Experimental ARPES map of BP on Au(111) surface. Calculated ARPES maps for $P_9 \times 2$ projected into BP atoms(e) and first Au layer atoms(f) are also reported. Since only first few layers of the interface contribute to the experimental spectra, sum of BP and first Au layer(d) contributions are plotted for comparison with experimental ARPES map. Experimental and calculated maps were taken at -1.0 eV.

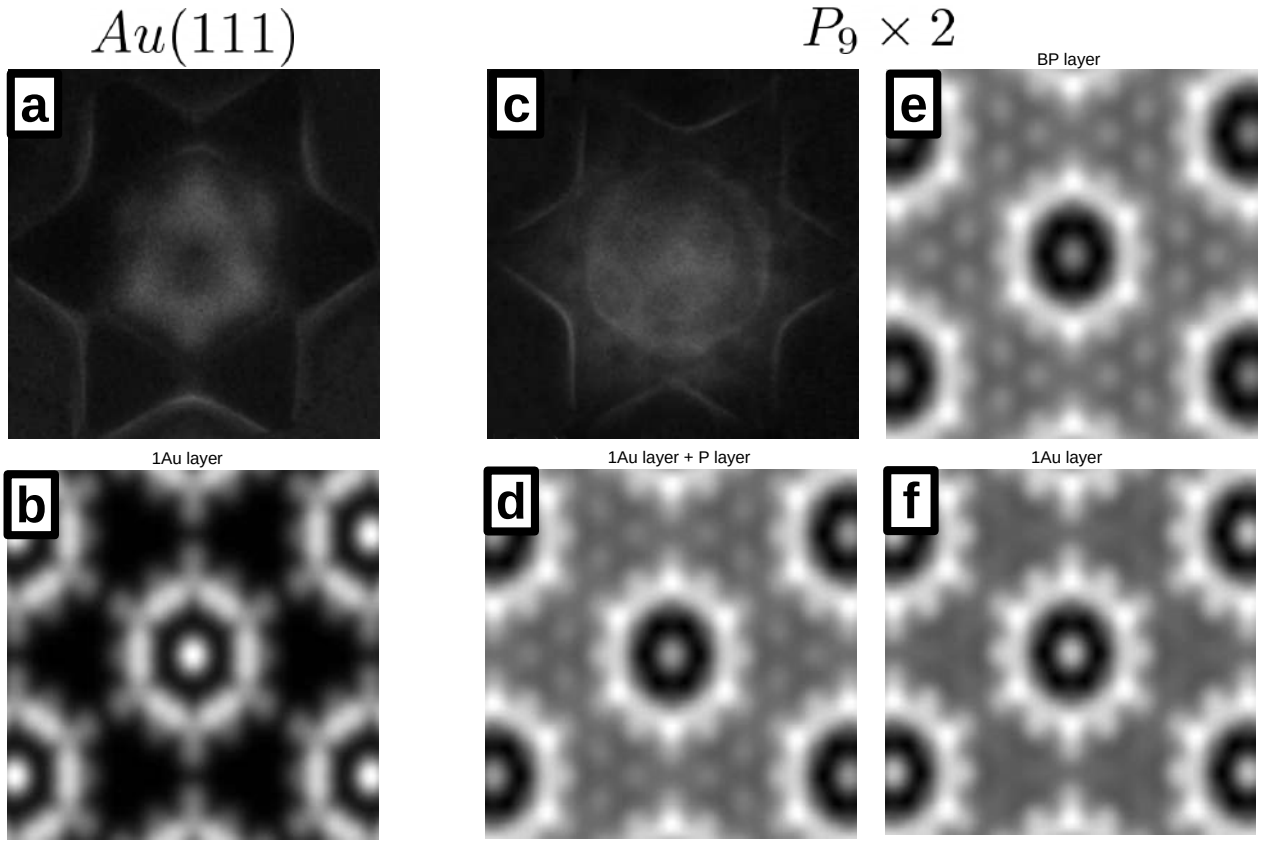

Figure 4.10: (a) Experimental ARPES map of clean Au(111) surface. (b) Calculated ARPES map projected into first layer of clean Au(111) surface. (c) Experimental ARPES map of BP on Au(111) surface. Calculated ARPES maps for $P_9 \times 2$projected into BP atoms(h), Au edge atoms(g) and first Au layer atoms(f) are also reported. Since only first few layers of the interface contribute to the experimental spectra, sum of the three single component(d) and of BP and Au edge contributions are plotted for comparison with experimental ARPES map. Experimental and calculated maps were taken at -1.0 eV.

Chapter 5

Conclusion and perspective

In this thesis, some selected systems based on 2D materials on metallic substrates (G on Ni and BP on Au) have been examined in terms of structural, electronic and reactivity properties, using different and complementary numerical approaches. Most of the work has been performed using quantum mechanical ab-initio simulations based on density functional theory (DFT). Part of the work concerned the construction via neural network techniques and the validation of new interatomic potentials to extend the investigation of G/Ni systems to more realistic configurations or to dynamical processes not directly affordable by ab-initio calculations.

Despite the extensive studies already existing on G, its interaction with a metallic substrate, the role of intercalants and of defects on its properties were not yet fully understood at the beginning of this thesis work. The knowledge of the structural and electronic properties of BP on Au(111) was even more limited. Still some open issues remain, but some important results have been achieved. We summarize them as follows:

- *The thesis work allowed to understand the effects of the intercalation of the carbon monoxide (CO) at G/Ni interface, i.e. decoupling with peculiar consequences on the electronic structure, opening the way to the design of CO sensors* [104].
  The electronic properties of G can be modified at will for potential technological applications. To this end, the intercalation of

Carbon Monoxide at G/Ni(111) interface has been investigated with DFT, identifying the most favorable adsorption sites. Even at a coverage as low as 0.14 ML, G detaches from the substrate and recovers the peculiar features of the free-standing layer. Although G is weakly interacting with CO/Ni support, a sizeable p-doping effect with a shift of the Fermi level roughly proportional to the coverage is clearly visible in the Density of States projected into C atoms. This sensitivity of the G doped state to the presence of intercalated CO could be used to design atomic-scale sized sensors.

- *The decoupling of G from the Ni substrate can be also due to the formation of a carbide layer at the interface between G and Ni(111)* [88].
  Using DFT calculations, the role of G cover on the mechanisms for the Ni_2C formation has been investigated. Structural model for both Epitaxial and Rotated domains of G (EG and RG) on Ni_2C/Ni(111) interface have been constructed. G cover induces a destabilization of C adsorption sites at Ni(111) surface: while EG, due to its strong interaction with Ni(111), completely locks the nickel surface preventing the carbide formation, rotated G allows higher concentration of subsurface C atoms, enabling the transition from C-enriched Ni(111) to a Ni_2C reconstructed layer. Thus, this work explains why carbide is experimentally detected only under rotated G domains, suggesting the possibility of employing 2D covers to tune the metal surface reactivity.

- *Another important result obtained concerns the characterization and control of defects in G/Ni systems, in particular on Ni(100), extending previous works on Ni(111). Such defects make G, otherwise inert, reactive to atoms (such as cobalt) and molecules (such as CO)* [150].
  Several different kind of defects in G layer have been identified:

some of them have been attributed to C-vacancies passivated by substrate, others to Ni adatoms trapped in the vacancy. The reactivity of G in presence of such defects have been investigated: Cobalt cluster and carbon monoxide molecules can be easily adsorbed on these sites. The control of defects is therefore extremely important.

- *In G/Ni(111), the coexistence of domains with different registries with the substrate is experimentally observed: in this work it has been predicted by large-scale simulations based on effective interatomic potentials.*
  The desire of extending the investigation to more realistic G/Ni configurations (e.g., large domains) has driven the investigation to an approach alternative to "brute force" DFT, i.e., to the construction and validation of interatomic potentials through a Neural Network approach (DeePMD) where learning starts from selected configurations studied by DFT. The new interatomic potential, which has been then used for classical molecular dynamics simulations with the LAMMPS package, allows the investigation of very large systems with thousands of atoms which have been impossible to study by DFT. A successful application has been done on large G ribbons/flakes on Ni(111), with the result of predicting the coexistence of domains with different registry with the substrate on a scale of 10 nm, in agreement with experiments.

- *The investigation of BP/Au(111) allowed to clarify the configuration at the atomic scale, through an unprecedent accurate comparison of measured and calculated angle-resolved photoelectron spectroscopy (ARPES) spectra and maps.* [151]
  BP on Au(111) was recently synthesized at CNR. A close comparison between different experimental results and simulations allowed to identify the best structural model formed by P_9 pyra-

midal shaped domains connected by Au adatoms. The nice correspondence with many different new experimental results, including STM images and ARPES spectra, allows to discriminate among different possible models.

Several non trivial technicalities have been afforded in this work, including: different tools for calculations on complex systems (e.g., correct treatment of slab geometries and non-trivial periodicities, Van der Waals interactions; energy barrier calculations), several data analysis and post-processing procedures (e.g., projected electronic bands and density of states, simulations of ARPES spectra and maps), issues related to the use of High Performance Computing resources, and technicalities related to the generation of the effective interatomic potentials.

In conclusion, this thesis has provided some significant contribution to the comprehension of many experimental results, indicating once again the necessity of a synergetic effort between simulations and experiments to shed light on the structure and properties of real systems. The field of 2D materials, however, remains still largely unexplored. In particular, an open challenge is to simulate some kinetics and dynamical processes, like those occurring during the growth that so greatly affect the structure and the quality of 2D materials. We are still far from that, but the initial work of this thesis on the generation of effective interatomic potentials could open the way towards reliable investigation in this direction.

Acknowledgments go to:

- CINECA for computational resources obtained through ISCRA C initiative and agreement with University of Trieste.
- PRIN2017 project FERMAT; MAECI ITALY-SERBIA project

Appendix

5.1 Ni lattice parameter calculation

Nickel has a face-centered cubic (figure 5.1a) crystalline structure. In order to compute its equilibrium lattice parameter a series of scf calculations for different values of lattice parameter and different values of energy cutoffs (figure 5.1b). A part from the overall shift, the four curves seem to converge to the same behavior as the energy cutoff increases and the minimum at about 3.52 Å. This value is compatible with the known one from [152].

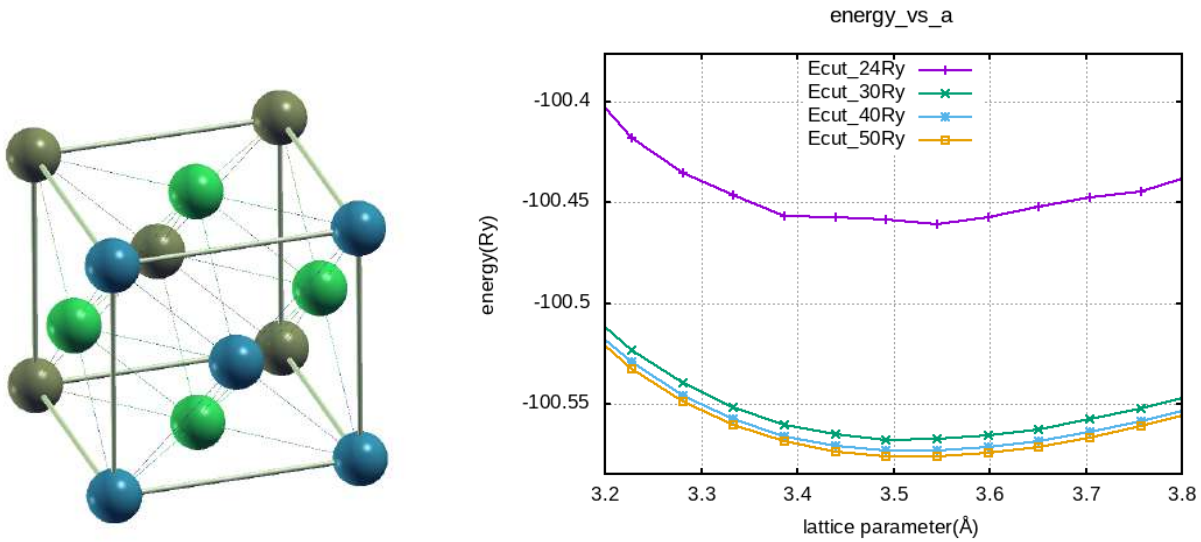

(a) (b)

Figure 5.1: Stick-and-ball model of nickel bulk (a) and plot of the energy versus lattice parameter in (b).

5.2 C1s pseudopotential generation

In this appendix we describe the details behind the construction of Ultrasoft PseudoPotential of Carbon with a missing 1s core electron, which we needed to evaluate the Core Level Shifts of C $1s$ core states in different chemical environments. PseudoPotential has been generated using `ld1.x` code of Quantum ESPRESSO package within the scalar-relativistic approximation and non-linear core correction. The pseudization of atomic orbitals inside the core regions was performed with Troullier-Martins pseudization algorithm [153].
We generated PP with $1s^1 2s^2 2p^2$ electronic configuration of C atom: $1s$ electron was treated as core and $2s$ and $2p$ electrons as valence. We used the inner and outer cutoff radii 1.0 and 1.2 a.u. for $2s$ states and 0.9 and 1.4 a.u. for $2p$ states. Pseudo wavefunctions (PS) outside the pseudization region of $\approx$ 1 a.u. reproduce well the All-electron wavefunctions(AE), as depicted in figure 5.2. Logarithmic derivatives $D^l(\epsilon, r)$ of AE and PS wavefunctions(figure 5.3), defined as:

$$D^l(\epsilon, r) = \frac{d}{dr} ln\psi_l(\epsilon, r) \tag{5.1}$$

evaluated at $r = 2.0 a.u.$ agree very well in the relevant energy range from $-2Ry$ to $2Ry$.

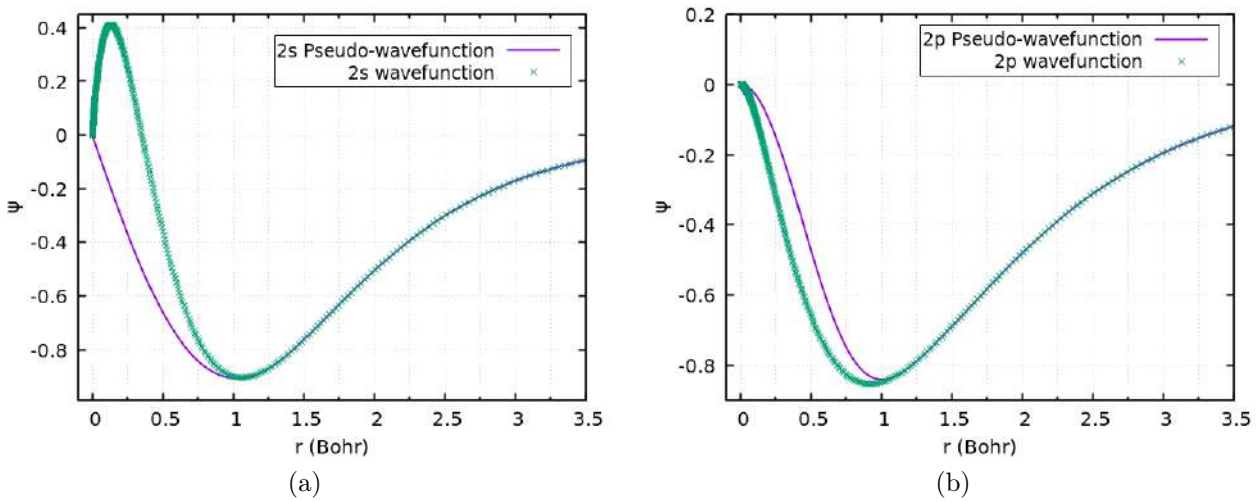

(a) (b)

Figure 5.2: Radial-Wavefunctions of 2S-states (a) and of 2P-states. Image taken from [88].

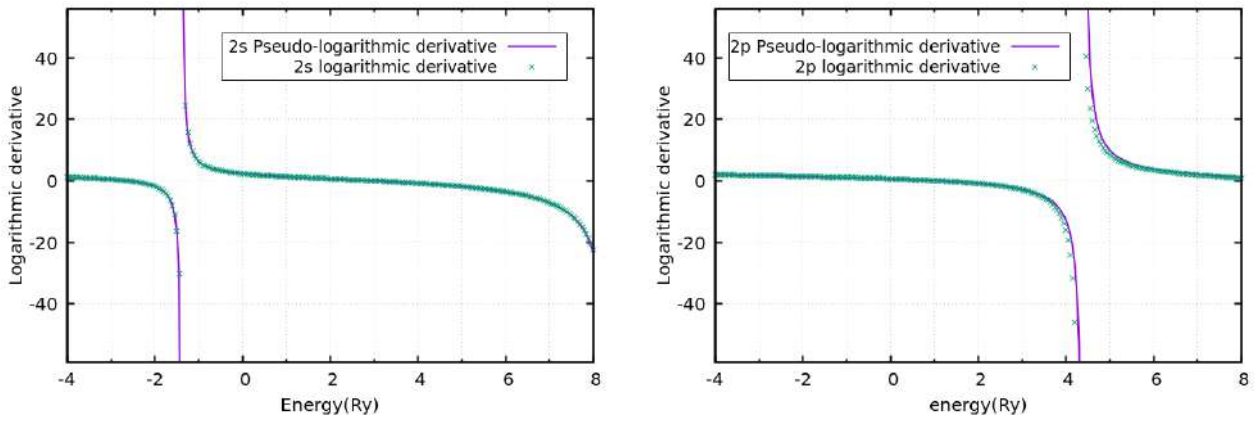

(a) (b)

Figure 5.3: Logarithmic derivative of 2-S(a) and 2-P(b) radial wavefunctions. Image taken from [88].

To test the accuracy of the generated PP, we evaluated the eigenvalues of valence states by solving the Kohn-Sham equations at different plane wave cutoff energies in wavefunction's expansion as presented in table 5.1. As we can see, we have a good agreement for both eigenvalues only for cutoffs larger than $50Ry$ thus in all calculations involving our PP we have been using plane wave cutoff of $50Ry$. Transferability of PP was tested comparing the differences between the AE and PS energy spectra that correspond to different valence configurations of C atom(table 5.2). Errors on eigenvalues do not exceed 0.005 Ry ensuring resonably good transferability of the PP.

cutoff (Ry)	$\epsilon_2 s(Ry)$	$\epsilon_2 p(Ry)$
20	-2.1968	-1.4862
30	-2.1969	-1.5585
40	-2.1970	-1.5668
50	-2.1970	-1.5670
60	-2.1971	-1.5671
80	-2.1971	-1.5672
100	-2.1971	-1.5672
AE	-2.1981	-1.5680

Table 5.1: Energies of C valence states obtained at different energy cutoff in the plane wave expansion of wavefunctions. AE corresponds to eigenvalues obtained from all-electron calculations.

electronic configuration	$\Delta(AE-PS)_{2s}(Ry)$	$\Delta(AE-PS)_{2p}(Ry)$
$1s^1 2s^2 2p^2$	0.00151	0.00024
$1s^1 2s^1 2p^3$	0.00264	0.00062
$1s^1 2s^0 2p^4$	0.00450	0.00029

Table 5.2: Energy difference between AE and PS eigenvalues for different electronic configurations.

Appendix B: Poster

JULY 07, 2020
CONFERENCE ONLINE

Graphene Online &2DM
Fundamental Research Insights

GO 2020

Ni_2C formation at the graphene/Ni(111) interface: a first-principles investigation

Simone Del Puppo[1],Srdjan Stavrić [1,2],Željko Šljivančanin [2], Maria Peressi [1]

[1]Department of Physics, University of Trieste, via Valerio 2, I-34127 Trieste, Italy
[2]Vinča Institute of Nuclear Sciences, University of Belgrade, P. O. Box 522, RS-11001, Republic of Serbia

ABSTRACT

The peculiar graphene(G) properties are very sensitive to its coupling with the substrate. In case of G grown on Ni(111) surface, this is strongly affected by the formation of an intercalated carbide (Ni_2C) layer, which, remarkably, occurs only under rotated graphene (RG) and not under epitaxial graphene (EG) domains [1,2]. We performed first principles simulations based on density functional theory to explain the preferential surface segregation of the Ni-dissolved C atoms under RG domains [3]. Furthermore, a complete description of the electronic properties of G with and without carbide, in RG and EG domains is obtained. Finally, we obtained the specific C1s core level shifts that are the fingerprints of different G/Ni_2C/Ni(111) configurations in good agreement with the experimental results.

STRUCTURE

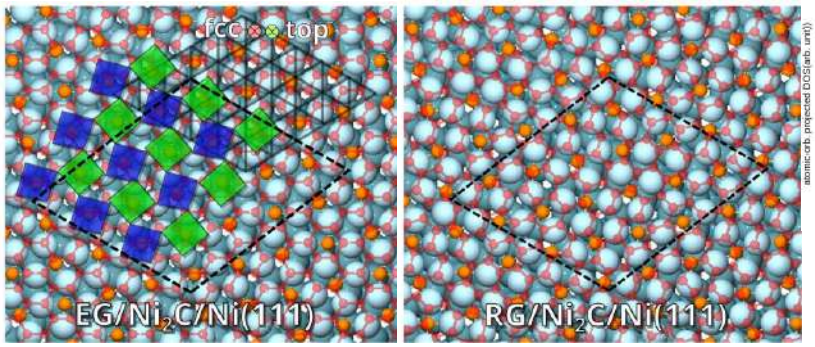

- simulation cell: 6 x(√43 R 7°.6)
- matching three different lattices (and G with two different orientations)
- Ni_2C is stable under both EG and RG
- Ni_2C detaches both EG and RG from Ni

ELECTRONIC PROPERTIES

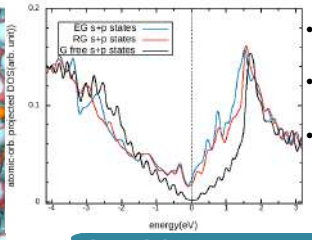

- Dirac Cones preserved
- G nearly free-standing
- E_F shift: 0.1 eV

C1s CORE LEVEL SHIFTS

- fingerprint of different chemical environment
- two different CLS for carbide are found
- agreement th./exp.

TOWARDS CARBIDE FORMATION

SURFACE SEGREGATION OF Ni-DISSOLVED C

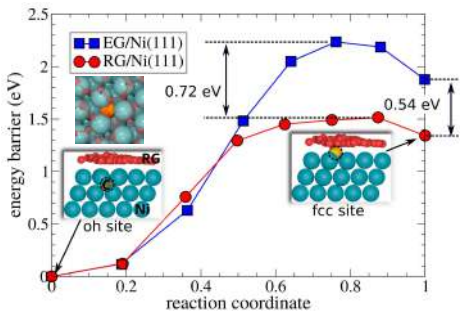

INCREASING THE CONCENTRATION OF SUBSURFACE C

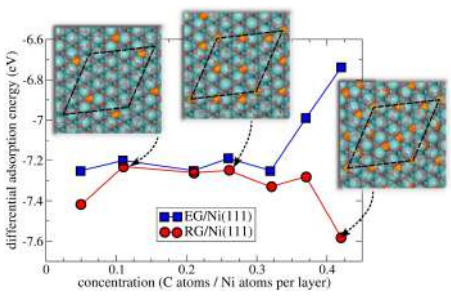

- C added one-by-one on *oh* sites
- concentration < 0.35: similar chemical potential in EG and RG
- concentration > 0.35: opposite behaviour, under EG further segregation is more difficult

CONCLUSIONS

- subsurface *oh* sites are the most stable both in RG and EG for dissolved C
- Surface segregation is an activated process (higher energy barrier under EG)
- EG and RG detached by Ni_2C from the surface (~ free-standing features)
- Ni-dissolved C atoms prefer subsurface octahedral sites
- Carbide formation favored only under RG for thermodynamics and kinetics arguments

CONTACT PERSON

Simone Del Puppo
SIMONE.DELPUPPO@phd.units.it

REFERENCES

[1] C. Africh et al., Scientific Reports 6 (2016) 19734.
[2] L. L. Patera et al., ACS Nano 7 (2013) 7901.
[3] S. Stavrić et al., to be submitted

Farnesina
Ministero degli Affari Esteri e della Cooperazione Internazionale

Project funded by a grant from the Italian Ministry of Foreign Affairs and International Cooperation.

Graphene Online &2DM Fundamental Research Insights GO 2020

Figure 5.4: Poster presented at online conference GO2020 on July the 7^th 2020.

Moiré-regulated anisotropic distribution of Co adatoms and nanoclusters on graphene/Ni(100)

S. Del Puppo[1], S.Stavric[1,2], V. Chesnyak[1,3], M. Panighel[3], G. Comelli[1,3], C. Africh[3], M.Peressi[1]

[1] Physics Department, University of Trieste, Italy.
[2] Vinča Institute of Nuclear Sciences - National Institute of the Republic of Serbia and University of Belgrade, Serbia
[3] CNR-IOM, Laboratorio TASC, Italy.

Graphene(G) grown on Ni(100) is periodically corrugated due to the lattice mismatch with the substrate, forming different moiré patterns. In striped moiré, strongly (chemisorbed) and weakly (physisorbed) interacting G regions alternate, inducing anisotropy modulated electronic structure and reactivity properties. Density functional theory calculations predict that Co adatoms and nanoclusters, for instance, prefer to bind to ridge much stronger than on valley. The analysis of charge redistribution upon Co adsorption on G/Ni(100) shows that an electron rearrangement takes place, originating a repulsive Co-Ni interaction mediated by G and modulated by its corrugation, which allows Co atoms to drift more easily from the valley to the ridge than in any other direction, as suggested by the calculated diffusion barriers. These findings are confirmed by scanning-tunneling-microscopy images of real samples that show a larger concentration of Co adatoms and nanoclusters on G's ridges as compared to valleys.

G/Ni(100)

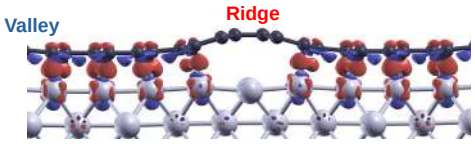

G/Ni(100) alternates regions with C closer to the substrate (valley) to regions with C further away(ridge)[1]. Induced charge density plot show a different chemical environment in the two regions: C on valley have a strong interaction with the substrate, with an overlap of C-2p and Ni-3d orbitals, while C on ridge is detached from Ni substrate. Thus, valley and ridge have different reactivity with respect to metal adatoms adsorption.

Valley:
- G chemisorbed
- Ni donates electrons to G

Ridge:
- G physisorbed
- No charge redistribution

Co ADSORPTION

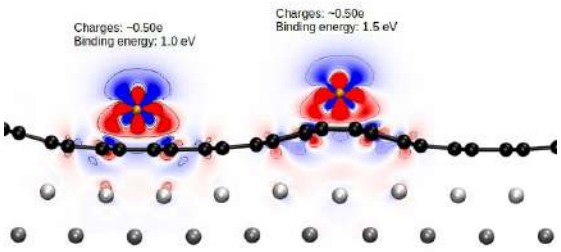

Upon adsorption on G/Ni(100), Co donates ~0.5e to G both on valley and on ridge while Nickels below ridges are neutral and those below valleys are positively charged. Thus, the interaction of Ni with Co@valleys is repulsive; this explains the higher Co binding energy on ridge due to weaker repulsion.

Co adsorption on G/Ni(100):
- Co donates ~ 0.5e to G
- Co-Ni interaction is repulsive
- Co Binding Energy higher on R
- Co is highly mobile: higher concentration and clusterization on ridges

Co DISTRIBUTION

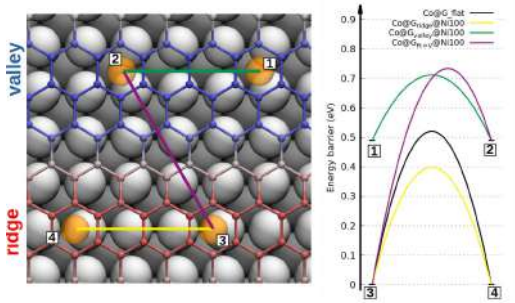

The Co mobility on G/Ni(100) is higher than on freestanding G (lower diffusion barriers both on valleys and on ridges due to Co-Ni repulsive interaction). Furthermore, Co diffusion from valley to ridge is favored rather than vice versa leading to a higher concentration of Co adatoms on ridge rather than on valley, as showed in the experimental STM image.

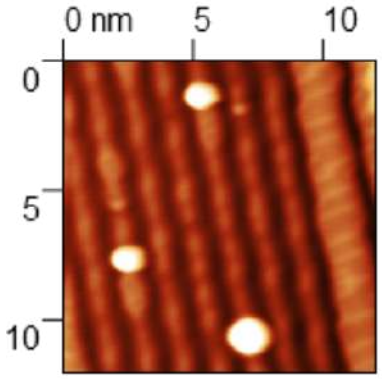

STM image with Co clusters on ridges.

CONTACT PERSON

Simone Del Puppo
SIMONE.DELPUPPO@phd.units.it
University of Trieste

REFERENCES

[1] Z. Zou et al., Graphene on nickel (100) micrograins: Modulating the interface interaction by extended moiré superstructures, Carbon, Volume 130, April 2018, 441-447

ACKNOWLEDGEMENT

We acknowledge funds from MIUR (PRIN 2017: Projects no. 2017NYPHN8 and no. 2017KFY7XF); MAECI (PGR Italy-Serbia 2019-2021); computational resources from CINECA through ISCRA and University of Trieste.

Psi-k Conference
22-25 August 2022
Lausanne, Switzerland
www.psik2022.net

Figure 5.5: Poster presented at Psi-k conference on August the 24^{th} 2022.

Bibliography

[1] K. S. Novoselov, A. K. Geim, S. Morozov, D. Jiang, M. I. Katsnelson, I. Grigorieva, S. Dubonos, A. A. Firsov, *Two-dimensional gas of massless Dirac fermions in graphene*, Nature 438 (2005) 197-200.

[2] A. K. Geim, *Graphene: Status and Prospects*, Science 324 (2009) 1530-1534.

[3] H. Liu, A. T. Neal, Z. Zhu, Z. Luo, X. Xu, D. Tománek, P. D. Ye, *Phosphorene: An Unexplored 2D Semiconductor with a High Hole Mobility*, ACS Nano 8, 5, (2014) 4033-4041.

[4] M. Batmunkh, M. Bat-Erdene, J. G. Shapter, *Phosphorene and Phosphorene-Based Materials – Prospects for Future Applications*, Adv. Mater. 28 (2016) 8586-8617.

[5] R. Ganatra, Q. Zhang, *Few-Layer MoS2: A Promising Layered Semiconductor*, ACS Nano 8, 5, (2014) 4074-4099.

[6] R. Lv, J. A. Robinson, R. E. Schaak, D. Sun, Y. Sun, T. E. Mallouk, M. Terrones, *Transition Metal Dichalcogenides and Beyond: Synthesis, Properties, and Applications of Single- and Few-Layer Nanosheets*, Acc. Chem. Res. 48 (2015) 56-64.

[7] T. Cao, G. Wang, W. Han, H. Ye, C. Zhu, J. Shi, Q. Niu, P. Tan, E. Wang, B. Liu, *Valley-selective circular dichroism of monolayer molybdenum disulphide*, Nat. Commun. 3 (2012) 887-892.

[8] M. Xu, T. Liang, M. Shi, H. Chen, *Graphene-Like Two-Dimensional Materials*, Chem. Rev. 113 (2013) 3766-3798.

[9] A. J. Mannix, X. F. Zhou, B. Kiraly, J. D. Wood, D. Alducin, B. D. Myers, X. Liu, B. L. Fisher, U. Santiago, J. R. Guest, *Synthesis of borophenes: Anisotropic, two-dimensional boron polymorphs* Science 350 (2015) 1513-1516.

[10] B. Feng, J. Zhang, Q. Zhong, W. Li, S. Li, H. Li, P. Cheng, S. Meng, L. Chen, K. Wu, *Experimental realization of two-dimensional boron sheets*, Nat. Chem. 8 (2016) 563-568.

[11] L. Tao, E. Cinquanta, D. Chiappe, C. Grazianetti, M. Fanciulli, M. Dubey, A. Molle, D. Akinwande, *Silicene field-effect transistors operating at room temperature*, Nat. Nanotechnol. 10 (2015) 227-231.

[12] B. Lalmi, H. Oughaddou, H. Enriquez, A. Kara, S. Vizzini, B. Ealet, B. Aufray, *Epitaxial growth of a silicene sheet* , Appl. Phys. Lett. 97 (2010) 223109-223114.

[13] H. Oughaddou, H. Enriquez, M. R. Tchalala, H. Yildirim, A. J. Mayne, A. Bendounan, G. Dujardin, M. A. Ali, A. Kara, *Silicene, a promising new 2D material*, Prog. Surf. Sci. 90 (2015) 46-83.

[14] Z. Y. Zeng, Z. Y. Yin, X. Huang, H. Li, Q. Y. He, G. Lu, F. Boey, H. Zhang, *Single-Layer Semiconducting Nanosheets: High-Yield Preparation and Device Fabrication*, Angew. Chem. Int. Ed. 50 (2011) 11093-11098.

[15] K. S. Novoselov, D. Jiang, F. Schedin, T. J. Booth, V. V. Khotkevich, S. V. Morozov, A. K. Geim, *Two-dimensional atomic crystals* , Proc. Natl. Acad. Sci. USA 102 (2005) 10451-10455.

[16] J. N. Coleman, M. Lotya, A. O'Neill, S. D. Bergin, P. J. King, U. Khan, K. Young, A. Gaucher, S. De, R. J. Smith, I. V. Shvets, S. K. Arora, G. Stanton, H. Y. Kim, K. Lee, G. T. Kim, G. S. Duesberg, T. Hallam, J. J. Boland, J. J. Wang, J. F. Donegan,

J. C. Grunlan, G. Moriarty, A. Shmeliov, R. J. Nicholls, J. M. Perkins, E. M. Grieveson, K. Theuwissen, D. W. McComb, P. D. Nellist, V. Nicolosi, *Two-Dimensional Nanosheets Produced by Liquid Exfoliation of Layered Materials* , Science 331 (2011) 568-571.

[17] K. F. Mak, C. Lee, J. Hone, J. Shan, T. F. Heinz, *Atomically Thin MoS_2: A New Direct-Gap Semiconductor* , Phys. Rev. Lett. 105 (2010) 136805.

[18] A. A. Balandin, S. Ghosh, W. Bao, I. Calizo, D. Teweldebrhan, F. Miao, C. N. Lau, *Superior Thermal Conductivity of Single-Layer Graphene* , Nano Lett. 8 (2008) 902.

[19] J. Cheng, C. Wang, X. Zou, L. Liao, *Recent Advances in Optoelectronic Devices Based on 2D Materials and Their Heterostructures*, Adv. Optical Mater. 7 (2018) 1800441.

[20] K. F. Mak, L. Ju, F. Wang, T. F. Heinz, *Optical spectroscopy of graphene: From the far infrared to the ultraviolet* , Solid State Commun. 152 (2012) 1341.

[21] C. M. Corbet, C. McClellan, A. Rai, S. S. Sonde, E. Tutuc, S. K. Banerjee,*Field effect transistors with current saturation and voltage gain in ultrathin ReS_2*, ACS Nano 9 (2015) 363-70.

[22] Y. Lin, H. Komsa, C. Yeh, T. Björkman, Z. Liang, C. Ho, Y. Huang, P. Chiu, A. V. Krasheninnikov, K. Suenaga , *Single-Layer ReS_2: Two-Dimensional Semiconductor with Tunable In-Plane Anisotropy*, ACS Nano 9 (2015) 11249-11257.

[23] J. Miao, B. Song, Z. Xu, L. Cai, S. Zhang, L. Dong, C. Wang, *Single Pixel Black Phosphorus Photodetector for Near-Infrared Imaging*, Small 14 (2018) 1702082.

[24] F. Xia, H. Wang, Y. Jia, *Rediscovering black phosphorus as an anisotropic layered material for optoelectronics and electronics*, Nat. Commun. 5 (2014) 4458.

[25] Y. Cai, G. Zhang, Y. W. Zhang, *Layer-dependent Band Alignment and Work Function of Few-Layer Phosphorene*, Sci. Rep. 4 (2014) 6677.

[26] L. Sun, G. Yuan, L. Gao, J. Yang, M. Chhowalla, M. H. Gharahcheshmeh, K. K. Gleason, Y. S. Choi, B. H. Hong, Z. Liu, *Chemical vapour deposition*, Nat. Rev. Met. 1 (2021) 5.

[27] P. Giannozzi, S. Baroni, N. Bonini, M. Calandra, R. Car, C. Cavazzoni, D. Ceresoli, G. L. Chiarotti, M. Cococcioni, I. Dabo, A. Dal Corso, S. Fabris, G. Fratesi, S. de Gironcoli, R. Gebauer, U. Gerstmann, C. Gougoussis, A. Kokalj, M. Lazzeri, L. Martin-Samos, N. Marzari, F. Mauri, R. Mazzarello, S. Paolini, A. Pasquarello, L. Paulatto, C. Sbraccia, S. Scandolo, G. Sclauzero, A. P. Seitsonen, A. Smogunov, P. Umari and R. M. Wentzcovitch, *QUANTUM ESPRESSO: a Modular and Open-Source Software Project for Quantum Simulations of Materials*, J. Phys. Condens. Matter 21(2009) 395502.

[28] R. P. Feynman, *Forces in Molecules*, Phys. Rev. 56 (1939) 840-843.

[29] P.Hohenberg and W.Kohn, *Inohomogeneous Electron Gas*, Phys. Rev. 136(3B) (1964) B864-B871.

[30] W. Kohn, L. J. Sham, *Self-Consistent Equations Including Exchange and correlation Effects*, Phys. Rev. 140(4A)(1965) A1133-A1138.

[31] D. Raczkowski, A. Canning,L. W. Wang, *Thomas-Fermi charge mixing for obtaining self-consistency in density functional calculations*, Phys. Rev. B 64 (2001) 121101.

[32] D. D. Johnson, *Modified broyden's method for accelerating convergence in self consistent calculations*, Phys. Rev. B 38 (1988) 12807.

[33] J. P. Perdew, K. Burke, M. Ernzerhof, *Generalized Gradient Approximation Made Simple*, Phys. Rev. Lett. 77 (1996) 3865-3868.

[34] N. W. Ashcroft, N. D. Mermin, *Solid State Physics*, Holt Saunders (1976).

[35] M. T. Cohen, T. K. Bergstresser,*Band Structures and Pseudopotential Form Factors for Fourteen Semiconductors of the Diamond and Zinc-blende Structures*, Phys. Rev. 141 (1966)789.

[36] D. R. Hamann, M. Schlüter, C. Chiang, *Norm-Conserving Pseudopotentials*, Phys. Rev. Lett. 43 (1979) 1494.

[37] D. Vanderbilt, *Soft self-consistent pseudopotentials in a generalized eigenvalue formalism*, Phys. Rev. B 41 (1990) 7892.

[38] H.J.Monkhorst and J.D.Pack, *Special Points for the Brillouin-Zone Integrations*, Phys. Rev. B 13 (1976) 5188-5192.

[39] M.Methfessel,A.T.Paxton, *High-Precisio Sampling for Brillouin Zone Integration in Metals*, Phys. Rev. B 40 (1989) 3616-3621.

[40] C. G. Broyden, *The convergence of a class of double-rank minimization algorithms 1 general considerations*, IMA Jour. of App. Mat. 6 (1970) 76.

[41] R. Fletcher, *A new approach to variable metric algorithms*, The Computer Journal 13 (1970) 317.

[42] D. Goldfarb, *A family of variable-metric methods derived by variational means*, Math. Comp. 24 (1970)23.

[43] D. F. Shanno, *Conditioning of quasi-newton methods for function minimization*, Math. Comp. 24 (1970) 647.

[44] D. Sheppard, R. Terrell, G. Henkelman, *Optimization methods for finding minimum energy paths*, J. Chem. Phys. 128 (2008) 134106.

[45] G. Henkelman, B. P. Uberuaga,H. Jónsson, *A climbing image nudged elastic band method for finding saddle points and minimum energy paths*, J. Chem. Phys. 113 (2000)9901.

[46] J. Tersoff, D. R. Hamann, *Theory of the scanning tunneling microscope*, Phys. Rev. B 31 (1985) 805.

[47] V. Popescu, A. Zunger, *Extracting Eversus* $\overrightarrow{\boldsymbol{k}}$ *effective band structure from supercell calculations on alloys and impurities*, Phys. Rev. B 85 (2012) 085201.

[48] A. P. Thompson, H. M. Aktulga, R. Berger, D. S. Bolintineanu, W. M. Brown, P. S. Crozier, P. J. Veld, A. Kohlmeyer, S. G. Moore, T. D. Nguyen, R. Shan, M. J. Stevens, J. Tranchida,C. Trott, S. J. Plimpton, *LAMMPS - a flexible simulation tool for particle-based materials modeling at the atomic, meso, and continuum scales* , Comp. Phys. Comm. 271 (2022) 108171.

[49] D. Kingma, J. B. Adam, *A method for stochastic optimization*, In International Conference on Learning Representations (ICLR), (2015).

[50] H. Wang, L. Zhang, J. Han, W. E. *Deepm-kit: A deep learning package for many-body potential energy rapresentation and molecular dynamics*, Comp. Phys. Comm. 228 (2018) 178-184.

[51] M. Abadi, P. Barham, J. Chen, Z. Chen, A. Davis, J. Dean, M. Devin, S. Ghemawat, G. Irving, M. Isard, M. Kudlur, J. Levenberg, R. Monga, S. Moore, D. G. Murray, B. Steiner, P. Tucker, V. Vasudevan, P. Warden, M. Wicke, Y. Yu, X. Zheng, *TensorFlow: A system for large-scale machine learning*, 2th USENIX

Symposium on Operating Systems Design and Implementation (2016) 265-283.

[52] A. P. Bartok,R. Kondor,G. Csanyi, *On representing chemical environments*, Phys. Rev. B 87 (2013)184115.

[53] K. S. Novoselov, A. K. Geim, S. V. Morozov, D. Jiang, M. I. Katsnelson, I. V. Grigorieva, S. V. Dubonos, A. A. Firsov, *Two-dimensional gas of massless Dirac fermions in graphene* , Nature 438 (2005) 197.

[54] A. Si, G. Z. Kyzas, K. Pal, F. G. de Souza, *Graphene functionalized hybrid nanomaterials for industrial-scale applications: A systematic review* ,J. Mol. Struct. 1239 (2021) 130518.

[55] X. Li, W. Cai, J. An, S. Kim, J. Nah, D. Yang, R. Piner, A. Velamakanni, I. Jung, E. Tutuc et al., *Large-Area Synthesis of High-Quality and Uniform Graphene Films on Copper Foils* , Science 324 (2009)1312.

[56] S. Bae, H. Kim, Y. Lee, X. Xu, J. Park, Y. Zheng, J. Balakrishnan, T. Lei, H. R. Kim, Y. I. Song et al., *Roll-to-roll production of 30-inch graphene films for transparent electrodes* , Nat. Nanotechnol. 5 (2010) 574.

[57] J. Wintterlin, M. L. Bouquet, *Graphene on metal surfaces*, Surf. Sci. 603 (2009) 1841-1852

[58] Q. Yu, J. Lian, S. Siriponglert, H. Li, Y. P. Chen, S. Pei, *Graphene segregated on Ni surfaces and transferred to insulators* , App. Phys. Lett. 93 (2008) 113103.

[59] C. Busse, P. Lazic, R. Djemour, J. Coraux, T. Gerber, N. Atodiresei, V. Caciuc, R. Brako, A. N'Diaye,S. Blügel, J. Zegenhagen, T. Michely, *Graphene on Ir(111): Physisorption with Chemical Modulation* , Phys. Rev. Let. 107 (2011) 036101.

[60] D. E. Gardin, J. D. Batteas, M. A. Van Hove, G. A. Somorjai, *Carbon, nitrogen, and sulfur on Ni(111): formation of complex structures and consequences for molecular decomposition* , Surf. Sci. 296 (1993) 25.

[61] C. Klink, I. Stensgaard, F. Besenbacher, E. Lægsgaard, *An STM study of carbon-induced structures on Ni(111): evidence for a carbidic-phase clock reconstruction* , Surf. Sci. 342 (1995) 250.

[62] H. Nakano, J. Ogawa, J. Nakamura, *Growth mode of carbide from C_2H_4 or CO on Ni(111)* , Surf. Sci. 514 (2002) 256.

[63] P. Jacobson, B. Stöger, A. Garhofer, G. S. Parkinson, M. Schmid, R. Caudillo, F. Mittendorfer, J. Redinger, U. Diebold, *Nickel Carbide as a Source of Grain Rotation in Epitaxial Graphene* , ACS Nano 6 (2012) 3564.

[64] L. L. Patera, C. Africh, R. S. Weatherup, R. Blume, S. Bhardwaj, C. Castellarin-Cudia, A. Knop-Gericke, R. Schloegl, G. Comelli, S. Hofmann et al., *In Situ Observations of the Atomistic Mechanisms of Ni Catalyzed Low Temperature Graphene Growth* , ACS Nano 7 (2013) 7901.

[65] G. Bertoni, L. Calmels, A. Altibelli, V. Serin, *First-principles calculation of the electronic structure and EELS spectra at the graphene/Ni(111) interface*, Phys. Rev. B 71 (2005) 075402.

[66] L. Bignardi, P. Lacovig, M. M. Dalmiglio, F. Orlando, A. Ghafari, L. Petaccia, A. Baraldi, R. Larciprete, S. Lizzit, *Key role of rotated domains in oxygen intercalation at graphene on Ni(111)*, 2D Mater. 4 (2017) 025106.

[67] A. Varykhalov, J. Sanchez-Barriga, A. M. Shikin, C. Biswas, E. Vescovo, A. Rybkin, D. Marchenko, O. Rader, *Electronic and*

magnetic properties of quasi-freestanding graphene on Ni , Phys. Rev. Lett. 101 (2008) 157601.

[68] S. L. Wong, H. Huang, Y. Wang, L. Cao, D. Qi, I. Santoso, W. Chen, A. T. S. Wee, *Quasi-free-standing epitaxial graphene on SiC (0001) by fluorine intercalation from a molecular source*, ACS Nano 5 (2011)7662-7668.

[69] P. Sutter, J. T. Sadowski, E. A. Sutter, *Chemistry under cover: tuning metal-graphene interaction by reactive intercalation*, J. Am. Chem. Soc. 132 (2010) 8175-8179.

[70] R. Larciprete, S. Ulstrup, P. Lacovig, M. Dalmiglio, M. Bianchi, F. Mazzola, L. Hornekær, F. Orlando, A. Baraldi, P. Hofmann, S. Lizzit, *Oxygen switching of the epitaxial grapheneemetal interaction* , ACS Nano 6 (2012) 9551-9558.

[71] R. Mu, Q. Fu, L. Jin, L. Yu, G. Fang, D. Tan, X. Bao, *Visualizing chemical reactions confined under graphene* , Angew. Chem. Int. 51 (2012) 4856-4859.

[72] E. Granas, M. Andersen, M. A. Arman, T. Gerber, B. Hammer, J. Schnadt, J. N. Andersen, T. Michely, J. Knudsen, *CO intercalation of graphene on Ir (111) in the millibar regime* , J. Phys. Chem. C 117 (2013) 16438-16447.

[73] A. Ambrosetti, P. Silvestrelli, *Toward Tunable CO Adsorption on Defected Graphene: The Chemical Role of Ni(111) and Cu(111) Substrates* , J. Phys. Chem. C 121 36 (2017) 19828-19835.

[74] L. Verlet, *Computer "experiments" on classical fluids. I. Thermodynamical properties of Lennard-Jones molecules*, Phys. Rev. 159 (1967) 98-103.

[75] M. W. Finnis, J. E. Sinclair, *A simple empirical N-body potential for transition metals*, Philos. Mag. A 50 (2006) 45-55.

[76] M. S. Daw, M. I. Baskes, *Embedded-atom method: derivation and application to impurities, surfaces, and other defects in metals*, Phys. Rev. B 29 (1984) 6443-6453.

[77] H. Wang, L. Zhang, J. Han, E. Weinan, *DeePMD-kit: a deep learning package for many-body potential energy representation and molecular dynamics*, Comput. Phys. Commun. 228 (2018) 178-184.

[78] L. Bonati, M. Parrinello, *Silicon liquid structure and crystal nucleation from ab-initio deep metadynamics*, Phys. Rev. Lett. 121 (2018) 265701.

[79] T. Wen, C.-Z. Wang, M. J. Kramer, Y. Sun, B. Ye, H. Wang, X. Liu, C. Zhang, F. Zhang, K.-M. Ho, N. Wang, *Development of a deep machine learning inter-atomic potential for metalloid-containing Pd-Si compounds*, Phys. Rev. B 100 (2019) 174101.

[80] M. F. Calegari Andrade, H.-Y. Ko, L. Zhang, R. Car, A. Selloni, *Free energy of proton transfer at the water-TiO_2 interface from ab initio deep potential molecular dynamics*, Chem. Sci. 11 (2020) 2335-2341.

[81] H. Niu, L. Bonati, P. M. Piaggi, M. Parrinello, *Ab-initio phase diagram and nucleation of gallium*, Nat. Commun. 11 (2020) 2654.

[82] L. Tang, Z. J. Yang, T. Q. Wen, K. M. Ho, M. J. Kramer, C. Z. Wang, *Development of interatomic potential for Al-Tb alloys using a deep neural network learning method*, Phys. Chem. Chem. Phys. 22 (2020) 18467-18479.

[83] N. Mounet, N. Marzari, *First-principles determination of the structural, vibrational and thermodynamic properties of diamond, graphite, and derivatives*, Phys. Rev. B 71 (2005) 205-214.

[84] É. I. Isaev, A. I. Likhtenshtein, Yu. Kh. Vekilov, E. A. Smirnova, *Phonon Spectra of Li_2Ni3Al and B_2NiAl: Ab-initio Calculations*, Solid State Comm. 129 (2004) 809-814.

[85] F. Bianchini, L. L. Patera, M. Peressi, C. Africh, G. Comelli, *Atomic Scale Identification of Coexisting Graphene Structures on Ni(111)* , J. Phys. Chem. Lett. 5 467 (2014).

[86] L. L. Patera, F. Bianchini, G. Troiano, C. Dri, C. Cepek, M. Peressi, C. Africh, G. Comelli, *Temperature-Driven Changes of the Graphene Edge Structure on Ni(111): Substrate vs Hydrogen Passivation*, Nano Lett. 15 (1) (2015) 56-62;

[87] C. Africh, C. Cepek, L. L. Patera, G. Zamborlini, P. Genoni, T. O. Menteş, A. Sala, A. Locatelli, G. Comelli, *Switchable graphene-substrate coupling through formation/dissolution of an intercalated Ni-carbide layer* , Sci. Rep. 6 19734 (2016).

[88] S. Stavrić, S. Del Puppo, Ž. Šljivančanin, M. Peressi, *First-principles study of nickel reactivity under two-dimensional cover: Ni_2C formation at rotated graphene/Ni(111) interface* , Phys. Rev. Mater. 5 (2021) 014003.

[89] S. Grimme, *Density functional theory with London dispersion corrections* , Wiley Interdisciplinary Reviews: Computational Molecular Science 1 (2011) 211-228.

[90] Pseudopotentials available on: https://www.quantum-espresso.org/pseudopotentials.

[91] R. Martinez-Gordillo, C. Varvenne, H. Amara, and C. Bichara, *Ni_2C surface carbide to catalyze low-temperature graphene growth*, Phys. Rev. B 97 (2018)205431.

[92] J. J. McCarroll, T. Edmonds, R. C. Pitkethly, *Interpretation of a Complex Low Energy Electron Diffraction Pattern: Carbona-*

ceous and Sulphur-containing Structures on Ni(111), Nature 223 (1969)1260.

[93] F. Mittendorfer, A. Garhofer, J. Redinger, J. Klimes, J. Harl, G. Kresse, *Graphene on Ni(111): Strong interaction and weak adsorption*, Phys. Rev. B 84 (2011)201401.

[94] P. T. Sprunger, F. Besenbacher, I. Stensgaard, *STM investigation of the Ni(111)-c(4x2)-2CO structure*, Chem. Phys. Lett. 243(1995) 439-444.

[95] L. D. Mapledoram, M. P. Bessent, A. Wander, D. A. King, *An automated tensor LEED analysis of the Ni(111) c(4x2)-2CO structure*, Chem. Phys. Lett. 228 (1994) 527-532.

[96] L. Becker, S. Aminipirooz, B. Hillert, M. Pedio, J. Haase, *Threefold-coordinated hollow adsorption site for Ni(111)-c(4x2)-CO: a surface-extended x-ray absorption fine structure study*, Phys. Rev. B 47 (1993) 9710-9714.

[97] J. C. Campuzano, R. Dus, G. Greenler, *The sticking probability, dipole moment and absolute coverage of CO on Ni(111)*, Surf. Sci. 102 (1981) 172-184.

[98] X. Hao, B. Wang, Q. Wang, R. Zhang, D. Lib, *Insight into both coverage and surface structure dependent CO adsorption and activation on different Ni surfaces from DFT and atomistic thermodynamics*, Phys. Chem. Chem. Phys. 18 (2016) 17606-17618.

[99] V. Shah, T. Li, K. L. Baumert, H. Cheng, D. S. Sholl, *A comparative study of CO chemisorption on flat and stepped Ni surfaces using density functional theory*, Surf. Sci. 537 (2003) 217-227.

[100] A. Eichler, *CO adsorption on Ni(111): a density functional theory study*, Surf. Sci. 526 (2003) 332-340.

[101] A. Bandara, S. Katano, J. Kubota, K. Onda, A. Wada, K. Domen, C. Hirose, *The effect of co-adsorption of on-top CO on the sum-frequency generation signal of bridge CO on the Ni(111) surface*, Chem. Phys. Lett. 290 (1998) 261-267.

[102] N. Ikemiya, T. Suzuki, M. Ito, *Adlayer structures of CO adsorbed on Ni(111) electrode surfaces studied by in situ STM combined with IRAS*, Surf. Sci. 466 (2000) 119-126.

[103] G. Held, J. Schuler, W. Sklarek, H. P. Steinruck, *Determination of adsorption sites of pure and coadsorbed CO on Ni(111) by high resolution X-ray photo-electron spectroscopy*, Surf. Sci. 398 (1998) 154-171.

[104] S. Del Puppo et all., *Tuning graphene doping by carbon monoxide intercalation at the Ni(111) interface*, Carbon 176 (2021) 253.

[105] A.Eichler, *CO adsorption on Ni(111)-a density functional theory study*, Surf. Sci. 526 (2003) 332-340.

[106] M. Wei, Q. Fu, Y. Yang, W. Wei, E. Crumlin, H. Bluhm, X. Bao, *Modulation of surface chemistry of CO on Ni(111) by surface graphene and carbidic carbon* , J. Phys. Chem. C 119 (2015) 13590-13597.

[107] D. Perilli, S. Fiori, M. Panighel, H. Liu, C. Cepek, M. Peressi, G. Comelli, C. Africh, C. Di Valentin, *Mechanism of CO intercalation through the graphene/Ni(111) interface and effect of doping* , J. Phys. Chem. Lett. 11 (2020) 8887-8892.

[108] Z. Zou, V. Carnevali, M. Jugovac, L. L. Patera, A. Sala, M. Panighel, C. Cepek, G. Soldano, M. M. Mariscal, M. Peressi, G. Comelli, C. Africh, *Graphene on nickel (100) micrograins: Modulating the interface interaction by extended moiré superstructures* ,Carbon 130 (2018) 441.

[109] L. Wang, X. Zhang, H. L. W. Chan,F. Yan, F. Ding, *Formation and Healing of Vacancies in Graphene Chemical Vapor Deposition (CVD) Growth* ,J. Am. Chem. Soc. 135 (2013) 4476.

[110] M. K. Bayazit, L. Xiong, C. Jiang, S. J. A. Moniz, E. White, M. S. P. Shaffer , J. Tang, *Defect-Free Single-Layer Graphene by 10 s Microwave Solid Exfoliation and Its Application for Catalytic Water Splitting* , ACS Appl. Mater. Interfaces 13 (2021) 28600-28609.

[111] A. W. Robertson, B. Montanari, K. He, C. S. Allen, Y. A. Wu, N. M. Harrison, A. I. Kirkland, J. H. Warner, *Structural reconstruction of the graphene monovacancy*, ACS Nano 2013, 7, 5, 4495-4502

[112] V. Carnevali, L. L. Patera, G. Prandini, M. Jugovac, S. Modesti, G. Comelli, M. Peressi, C. Africh, *Doping of epitaxial graphene by direct incorporation of nickel adatoms*, Nanoscale 11 (2019) 10358.

[113] L. Leenaerts, B. Partoens, F. M. Peeters, *Adsorption of* H_2O, NH_3, CO, NO_2, NO *on graphene: A first-priciples study*, Phys. Rev. B 77 (2008) 125416.

[114] X. Hao, B. Wang, Q. Wang, R. Zhang, D. Li, Insight into both Coverage and Surface Structure Dependent CO Adsorption and Activation on Different Ni Surfaces from DFT and Atomistic Thermodynamics,PCCP, 26 (2016).

[115] R. Mas-Balleste, C. Gomez-Navarro, J. Gomez-Herrero, F. Zamora, *2D Materials: to Graphene and Beyond*, Nanoscale 3 (2011) 20-30.

[116] A. N. Abbas, B. Liu, L. Chen, Y. Ma, S. Cong, N. Aroonyadet, M. Kö pf, T. Nilges, C. Zhou, *Black Phosphorus Gas Sensors*, ACS Nano 9 (2015) 5618-5624.

[117] J. Sun, G. Zheng, H. Lee, N. Liu, H. Wang, H. Yao, W. Yang, Y. Cui, *Formation of Stable Phosphorus-Carbon Bond for Enhanced Performance in Black Phosphorus Nanoparticle-Graphite Composite Battery Anodes*, Nano Lett. 14 (2014) 4573-4580.

[118] F. Liu, C. Zhu, L. You, S. J. Liang, S. Zheng, J. Zhou, Q. Fu, Y. He, Q. Zeng, H. Fan et all., *2D Black Phosphorus/SrTiO3-Based Programmable Photoconductive Switch*, Adv. Mater. 28 (2016) 7768-7773.

[119] Y. Takao, A. Morita, *Electronic Structure of Black Phosphorus: Tight Binding Approach*, Physica B+C 105 (1981) 93-98.

[120] R. W. Keyes, *The Electrical Properties of Black Phosphorus*, Phys. Rev. 92 (1953) 580-584.

[121] Y. Du, C. Ouyang, S. Shi, M. Lei, *Ab Initio Studies on Atomic and Electronic Structures of Black Phosphorus*, J. Appl. Phys. 107 (2010)093718.

[122] A. N. Rudenko, M. I. Katsnelson, *Quasiparticle Band Structure and Tight-Binding Model for Single- and Bilayer Black Phosphorus*, Phys. Rev. B: Condens. Matter Mater. Phys. 89 (2014)201408.

[123] V. Tran, R. Soklaski, Y. Liang, L. Yang, *Layer-Controlled Band Gap and Anisotropic Excitons in Few-Layer Black Phosphorus*, Phys. Rev. B: Condens. Matter Mater. Phys. 89 (2014) 235319.

[124] J. Kim, S. S. Baik, S. H. Ryu, Y. Sohn, S. Park, B. Park, J. Denlinger, Y. Yi, H. J. Choi, K. S. Kim, *Observation of Tunable Band Gap and Anisotropic Dirac Semimetal State in Black Phosphorus*, Science 349 (2015) 723-726.

[125] A. S. Rodin, A. Carvalho, A. H. Castro Neto, *Strain-Induced Gap Modification in Black Phosphorus*, Phys. Rev. Lett. 112 (2014) 176801.

[126] L. Liang, J. Wang, W. Lin, B. Sumpter, V. Meunier, M. Pan, *Electronic Bandgap and Edge Reconstruction in Phosphorene Materials*, Nano Lett. 14 (2014) 6400-6406.

[127] L. Li, Y. Yu, G. J. Ye, Q. Ge, X. Ou, H. Wu, D. Feng, X. H. Chen, Y. Zhang, *Black phosphorus field-effect transistors*, Nat. Nanotechnol. 9 (2014) 372.

[128] L. Li, J. Kim, C. Jin, G. J. Ye, D. Y. Qiu, F. H. da Jornada, Z. Shi, L. Chen, Z. Zhang, F. Yang, K. Watanabe, T. Taniguchi, W. Ren, S. G. Louie, X. H. Chen, Y. Zhang, F. Wang, *Direct Observation of The Layer−Dependent Electronic Structure in Phosphorene*, Nat. Nanotechnol. 12 (2017) 21-25.

[129] S. P. Koenig, R. A. Doganov, H. Schmidt, A. H. Castro Neto, B. Zyilmaz, *Electric Field eect in ultrathin black phosphorus*, Appl. Phys. Lett. 104 (2014) 103106.

[130] Z. Chen, J. Appenzeller, J. Knoch, Y. Lin, P. Avouris, *Electron-Phonon Scattering in Metallic Single− Walled Carbon Nanotubes*, Nano Lett. 5 (2005)1497-1502.

[131] J. Li, X. Sun, C. Xu, X. Zhang, Y. Pan, M. Ye, Z. Song, R. Quhe, Y. Wang, H. Zhang, *Electrical contacts in monolayer blue phosphorene devices*, Nano Res. 11 (2018) 1834-1849.

[132] Z. Zhu, D. Tomanek, *Semiconducting Layered Blue Phosphorus: A Computational Study*, Phys. Rev. Lett. 112 (2014) 176802.

[133] S. Zhu, Y. Ni, J. Liu, K. Yao, *The study of interaction and charge transfer at black phosphorus–metal interfaces*, J. Phys. D: Appl. Phys. 48 (2015) 445101.

[134] J. Qiao, X. Kong, Z. Hu, F. Yang, W. Ji, *High-mobility transport anisotropy and linear dichroism in few-layer black phosphorus*, Nat. Commun. 5 (2014) 4475.

[135] K. Gong, L. Zhang, W. Ji, H. Guo, *Electrical contacts to monolayer black phosphorus: a first-principles investigation*, Phys. Rev. B 90 (2014) 125441.

[136] A. K. Tareen, K. Khan, S. Rehman , M. Iqbal , J. Yu , N. Mahmood, Z. Zhou, J. Yin , C. li , H. Zhang, *Recent development in emerging phosphorene based novel materials: Progress, challenges, prospects and their fascinating sensing applications*, Progress in Solid State Chemistry 65 (2022) 100336.

[137] E. Montes, U. Schwingenschlögl, *Nanotubes Based on Monolayer Blue Phosphorus*, Phys. Rev. B: Condens. Matter Mater. Phys. 94 (2016) 035412.

[138] Y. Aierken, D. Çakır, C. Sevik, F. M. Peeters, *Thermal Properties of Black and Blue Phosphorenes from a First-Principles Quasiharmonic Approach*, Phys. Rev. B: Condens. Matter Mater. Phys. 92 (2015) 081408.

[139] B. Ghosh, S. Nahas, S. Bhowmick, A. Agarwal, *Electric Field Induced Gap Modification in Ultrathin Blue Phosphorus*, Phys. Rev. B 91 (2015) 115433.

[140] J. Xie,M. S. Si, D. Z. Yang, Z. Y. Zhang, D. S. Xue, *A Theoretical Study of Blue Phosphorene Nanoribbons Based on First-Principles Calculations*, J. Appl. Phys. 116 (2014)073704.

[141] Q. F. Li, C. G. Duan, X. G. Wan, J. L. Kuo, *Theoretical Prediction of Anode Materials in Li−Ion Batteries on Layered Black and Blue Phosphorus*, J. Phys. Chem. C 119 (2015) 8662-8670.

[142] J. Zeng, P. Cui, Z. Zhang, *Half Layer by Half Layer Growth of a Blue Phosphorene Monolayer on a GaN(001) Substrate*, Phys. Rev. Lett. 118 (2017)046101.

[143] J. L. Zhang et al., *Epitaxial Growth of Single Layer Blue Phosphorus: A New Phase of Two-Dimensional Phosphorus* , Nano Lett. 16 (2016)4903-4908.

[144] S. Zhao, J. L. Zhang, W. Chen, Z. Li, *Structure of Blue Phosphorus Grown on Au(111) Surface Revisited*, J. Phys. Chem. C 124 (2020) 2024-202.

[145] S.Grimme, J. Antony, S. Ehrlich, H. Krieg, *A consistent and accurate ab initio parametrization of density functional dispersion correction (DFT-D) for the 94 elements H-Pu*, J. Chem. Phys. 132 (2010)154104.

[146] https://bitbucket.org/bonfus/unfold-x/src/master/ .

[147] A. P. Seitsonen, *Electronic structure of reconstructed Au(111) studied with density functional theory*, Surf. Sci. 643 (2016) 150-155.

[148] W. Zhang, H. Enriquez, A. J. Mayne, A. Bendounan, A. P. Seitsonen, A. Kara, G. Dujardin, H. Oughaddou, *First steps of blue phosphorene growth on Au(111)*, Mat. Today: Proceed. 39 (2021) 1153-1156.

[149] J. L. Zhang,S. Zhao, S. Sun, H. Ding, J. Hu, Y. Li, Q. Xu, X. Yu, M. Telychko, J. Su, C. Gu, Y. Zheng, X. Lian, Z. Ma, R. Guo, J. Lu, Z. Sun, J. Zhu, Z. Li, w. Chen, *Synthesis of Monolayer Blue Phosphorus Enabled by Silicon Intercalation*, ACS Nano 14 (2020) 3687-3695.

[150] in preparation, with M. Peressi, S. Srdjan, C. Africh, G. Comelli, V. Chesnyak, M. Panighel

[151] in preparation, with M. Peressi, A. Sala, A. Verdini, E. Vesselli

[152] C. Kittel, Introduction to Solid State Physics , John Wiley and Sons

[153] N. Troullier, J. L. Martins, *Efficient pseudopotentials for plane-wave calculations*, Phys. Rev. B 43 (1991) 1993.